












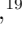






A 13-Billion-Year View of Galaxy Growth: Metallicity Gradient Evolution from the Local Universe to $z = 9$ with JWST and Archival Surveys

ZIHAO LI ^{1,2,3} ZHENG CAI ¹ XIN WANG ^{4,5,6} ZHAOZHOU LI ⁷ AVISHAI DEKEL ^{7,8} KARTICK C. SARKAR ^{7,9}
EDUARDO BAÑADOS ¹⁰ FUYAN BIAN ¹¹ AKLANT K. BHOWMICK ¹² LAURA BLECHA ¹² SARAH E. I. BOSMAN ^{10,13}
JACLYN B. CHAMPAGNE ¹⁴ XIAOHUI FAN ¹⁴ EMMET GOLDEN-MARX ¹⁵ HYUNSUNG D. JUN ¹⁶ MINGYU LI ¹
XIAOJING LIN ^{1,14} WEIZHE LIU ¹⁴ FENGWU SUN ¹⁷ MAXIME TREBITSCH ¹⁸ FABIAN WALTER ¹⁰
FEIGE WANG ¹⁹ YUNJING WU ¹ JINYI YANG ¹⁹ HUANIAN ZHANG ²⁰ SHIWU ZHANG ²¹ MINGYANG ZHUANG ²²
AND SIWEI ZOU ^{23,24}

¹Department of Astronomy, Tsinghua University, Beijing 100084, China

²Cosmic Dawn Center (DAWN), Denmark

³Niels Bohr Institute, University of Copenhagen, Jagtvej 128, DK-2200, Copenhagen N, Denmark

⁴School of Astronomy and Space Science, University of Chinese Academy of Sciences, Beijing 100049, China

⁵National Astronomical Observatories, Chinese Academy of Sciences, Beijing 100101, China

⁶Institute for Frontiers in Astronomy and Astrophysics, Beijing Normal University, Beijing 102206, China

⁷Center for Astrophysics and Planetary Science, Racah Institute of Physics, The Hebrew University, Jerusalem, 91904, Israel

⁸Santa Cruz Institute for Particle Physics, University of California, Santa Cruz, CA 95064, USA

⁹Raman Research Institute, Sadashivanagar, C. V. Raman Avenue, 560 080, Bangalore, India

¹⁰Max-Planck-Institut für Astronomie, Königstuhl 17, D-69117 Heidelberg, Germany

¹¹European Southern Observatory, Alonso de Cordova 3107, Casilla 19001, Vitacura, Santiago 19, Chile

¹²Department of Physics, University of Florida, Gainesville, Florida 32601, USA

¹³Institute for Theoretical Physics, Heidelberg University, Philosophenweg 12, D-69120, Heidelberg, Germany

¹⁴Steward Observatory, University of Arizona, 933 N Cherry Avenue, Tucson, AZ 85721, USA

¹⁵INAF-Astronomical Observatory of Padova vicolo dell'Osservatorio 5 35122 Padova, Italy

¹⁶Department of Physics, Northwestern College, 101 7th Street SW, Orange City, Iowa 51041, USA

¹⁷Center for Astrophysics — Harvard & Smithsonian, 60 Garden St., Cambridge, MA 02138, USA

¹⁸LUX, Observatoire de Paris, Université PSL, Sorbonne Université, CNRS, 75014 Paris, France

¹⁹Department of Astronomy, University of Michigan, 500 S State St, Ann Arbor, MI 48109, USA

²⁰Department of Astronomy, Huazhong University of Science and Technology, Wuhan 430074, China

²¹Zhejiang Lab, Hangzhou, Zhejiang 311121, China

²²Department of Astronomy, University of Illinois at Urbana-Champaign, Urbana, IL 61801, USA

²³Chinese Academy of Sciences South America Center for Astronomy, National Astronomical Observatories, CAS, Beijing 100101, China

²⁴Departamento de Astronomía, Universidad de Chile, Casilla 36-D, Santiago, Chile

ABSTRACT

The gas-phase metallicity gradients of galaxies have been extensively studied over the past four decades both in the local and high-redshift universe, as they trace the baryon cycle and growth of galaxies. With the unprecedented spatial resolution and sensitivity of the James Webb Space Telescope (JWST), it is now possible to measure metallicity and its radial gradients out to redshifts as high as $z = 9$. Here, we present a sample of 456 spectroscopically confirmed galaxies from redshifts $1.5 \lesssim z \lesssim 9$ that are spatially resolved on sub-kiloparsec (kpc) scales by deep JWST NIRCам or NIRISS Wide Field Slitless Spectroscopy (WFSS). Synthesizing these new JWST observations with legacy observations from the literature, we observe that at redshift $z > 5$, galaxy centers are more metal-rich, exhibiting negative metallicity gradients of ~ -0.4 dex kpc⁻¹. These gradients flatten over time, reaching near-zero around $z \approx 2$, coinciding with the peak of the cosmic star formation rate. Beyond this point, the gradients become negative again at lower redshifts approaching $z = 0$. This evolution likely reflects transitions in galaxy formation modes: an inside-out growth phase dominated by intense central star formation with inefficient feedback and limited gas mixing during “cosmic dawn”, enhanced gas mixing

due to feedback-driven wind and gas accretion at “cosmic noon”, and a later phase of slow evolution and reduced feedback toward the present day. These physical processes including gas accretion and feedback not only regulate star and galaxy formation on cosmic scale, but also shape the evolutionary pathways of individual galaxies over cosmic time.

Keywords: Galaxies (573) — High-redshift galaxies (734) — Chemical enrichment (225) — Galaxy evolution (594) — Galaxy formation (595) — Metallicity (1031)

1. INTRODUCTION

The process of star formation and the rate at which stars form across the universe (referred to as star formation rate density (SFRD) (P. Madau & M. Dickinson 2014)) depend on a complex interplay of gas inflows, gas outflows, and other mechanisms operating at different epochs in cosmic history. These processes also influence the metal content of galaxies, referred to as metallicity, and how metals are distributed within galaxies over time. They provide insight into the overall growth and evolution of galaxies throughout cosmic history.

However, key physical processes that dominate galaxy formation and evolution at each epoch are still subject to debate. Traditionally, galaxy evolution has been understood as a gradual process, shaped by both internal dynamics and external interactions over long timescales. These include processes such as the gradual accretion of gas, the formation of stellar structures like bars, gravitational interactions with neighboring galaxies (galaxy harassment), and mergers of galaxies (J. Kormendy & J. Kennicutt 2004; D. Kereš et al. 2005; P. F. Hopkins et al. 2009; M. Lang et al. 2014). Additionally, more dynamic and rapid events with shorter time scale, such as feedback from stellar winds and explosive supernovae (SNe) that last only a few million years (Myr), play a critical role in regulating star formation and the growth of galaxies (D. K. Erb 2015; K. El-Badry et al. 2016). Over the decades, various theoretical models and simulations have been developed to explain galaxy evolution (R. B. Larson 1974; S. J. Lilly et al. 2013; L. Magrini et al. 2016; P. F. Hopkins et al. 2023). Comprehensive models are required to account for the intricate processes driving the formation and distribution of chemical elements in galaxies, which is key to understanding their overall evolution (B. M. Tinsley 1980; B. Tapia-Contreras et al. 2025; C. Lyu et al. 2025; R. L. Graf et al. 2024).

Observing the cosmological evolution of metallicity gradients offers insights into the dominant processes at different epochs, as metal distribution is sensitive to gas transport and turbulence driven by these activities (P. Sharda et al. 2024). Over the past four decades, significant advancements have been made in observing galaxies metal contents and their distribution via multiple

techniques such as long slit or multi-object fiber spectrograph (B. E. J. Pagel & M. G. Edmunds 1981; M. G. Edmunds & B. E. J. Pagel 1984; I. N. Evans 1986; J. M. Vilchez et al. 1988; G. A. Shields 1990; M. B. Vila-Costas & M. G. Edmunds 1992; L. van Zee et al. 1998; S. Considère et al. 2000; L. Magrini et al. 2007; D. S. N. Rupke et al. 2010a; K. Grasha et al. 2022), integral field unit (IFU) observations (G. Cresci et al. 2010; A. M. Swinbank et al. 2012; J. Queyrel et al. 2012; T. Jones et al. 2013; P. Troncoso et al. 2014; D. Carton et al. 2015; I. T. Ho et al. 2015; E. Wuyts et al. 2016; N. Leethochawalit et al. 2016; F. Belfiore et al. 2017; J. Lian et al. 2018; H. Poetrodjojo et al. 2018; L. Sánchez-Menguiano et al. 2018; N. M. Förster Schreiber et al. 2018; D. Carton et al. 2018; M. D. Thorp et al. 2019; F. Bresolin 2019; Y. Zhuang et al. 2019; M. Curti et al. 2020b; A. Franchetto et al. 2021; S. Gillman et al. 2021; P. Lagos et al. 2022; G. Venturi et al. 2024; A. H. Khoram & F. Belfiore 2025; M. Ju et al. 2025; T. Li et al. 2025), slitless spectroscopy (T. Jones et al. 2015; X. Wang et al. 2017, 2020; R. C. Simons et al. 2021; Z. Li et al. 2022; X. Wang et al. 2022a; Y. Cheng et al. 2024), and radio telescopes (L. Vallini et al. 2024). Those works found a diversity of metallicity gradients across stellar masses and redshifts. They have reported negative metallicity gradients in local galaxies (e.g., I. T. Ho et al. 2015) as well as at higher redshifts (e.g., N. M. Förster Schreiber et al. 2018). Positive (inverted) gradients have also been observed, both in the local Universe (e.g., T. Li et al. 2025) and high-redshifts up to $z \sim 3$ (e.g., P. Troncoso et al. 2014; X. Wang et al. 2022a).

Various theoretical models have been proposed to explain certain behaviors of metallicity gradients. Negative gradients can arise in scenarios such as inside-out growth (S. Boissier & N. Prantzos 2000) and accretion disk with coplanar gas inflow (E. Wang & S. J. Lilly 2022; C. Lyu et al. 2025). P. Sharda et al. (2021b,c) suggest that negative gradients originate under equilibrium conditions, modeled through a more complex framework that accounts for the competition of radial advection, metal production, and gas accretion. The inside-out scenario is supported by analyzing radial distribution of stellar populations in low-redshift star forming galaxies

(E. Pérez et al. 2013; D. Goddard et al. 2017; N. Frankel et al. 2019), as well as by simulations (P. B. Tissera et al. 2016; F. Renaud et al. 2025).

On the other side, a flat or positive gradients can arise in the case of pristine gas accretion (G. Cresci et al. 2010; J. Molina et al. 2017; Z. Li et al. 2022), metal loss due to feedback-driven outflows (X. Wang et al. 2019; X. Sun et al. 2024), and mergers (D. S. N. Rupke et al. 2010a,b; P. Torrey et al. 2012; P. B. Tissera et al. 2022). Analytical model by P. Sharda et al. (2021b) suggests galaxies with positive gradients are out of equilibrium with extreme outflow metal loss, pristine gas accretion or the re-accretion of metal-enriched gas (J. Fu et al. 2013). Observations with the much-enriched circumgalactic medium (CGM) on large-scale at cosmic noon (Z. Cai et al. 2017; S. Zhang et al. 2023) also reflect metal-enrichment could happen on larger scale than previously expected.

However, a comprehensive understanding of how metallicity evolves over cosmic time remains elusive. This is largely because earlier observations often lacked the spatial resolution and sensitivity needed to map metal distributions within galaxies at scales smaller than a few hundred parsecs (sub-kiloparsec scales), which is crucial to resolve internal structures and small scale physical processes, and at greater distances corresponding to redshifts $z \gtrsim 3$. With several years of JWST observations, a large spectroscopic sample of high-redshift galaxies has now been assembled, enabling a comprehensive investigation of metallicity gradients across cosmic time (X. Wang et al. 2022a; J. E. Birkin et al. 2023; G. Venturi et al. 2024; S. Arribas et al. 2024; M. Ju et al. 2025).

In this paper, we present a sample of 456 galaxies spanning redshifts from $z = 1.7 - 9$ from JWST Wide Field Slitless Spectroscopic (WFSS) surveys, and measure the spatially resolved metallicities. Leveraging literature observations from archival surveys, we analyze the redshift evolution of metallicity gradients from $z = 0$ to $z = 9$.

This paper is organized as follows. In Section 2, we describe the observations and data reduction. The methods are described in Section 3. We present the results in Section 4 and discuss the physical implication of the observations. We summarize the main findings in Section 5. Throughout this article, we assume a standard flat Λ CDM cosmology with $\Omega_m = 0.3$, $\Omega_\Lambda = 0.7$, and $H_0 = 70 \text{ km s}^{-1} \text{ Mpc}^{-1}$. Emission lines are indicated as follows: $[\text{O III}]\lambda 5008 := [\text{O III}]$, $[\text{O II}]\lambda\lambda 3727, 3730 := [\text{O II}]$, $[\text{N II}]\lambda 6585 := [\text{N II}]$, if presented without wavelength values.

2. DESCRIPTION OF DATA

2.1. Observations and data reduction

In this work, we analyzed JWST observations from “ASPIRE F. Wang et al. 2023; J. Yang et al. 2023), “First Reionization Epoch Spectroscopically Complete Observations” (FRESCO P. A. Oesch et al. 2023)), and “The Next Generation Deep Extragalactic Exploratory Public Survey” (NGDEEP M. B. Bagley et al. 2024). By combining these surveys, we built a large statistical sample of galaxies that have spatially-resolved grism spectroscopy at $z \sim 2-8$ that can be used for metallicity gradient studies with sub-kpc resolution. The angular resolution reaches $0''.04 - 0''.14$ depending on the wavelength, corresponding to the physical size of $\sim 0.5 \text{ kpc}$ in the redshift range $1.7 < z < 3.5$ and $\sim 0.7 \text{ kpc}$ in the redshift range $5 < z < 9$.

The ASPIRE survey contains NIRCcam F356W R-grism observations of 25 Quasar fields, with direct imaging in the F356W, F200W, and F115W filters. FRESCO includes NIRCcam F444W R-grism WFSS observations, with direct imaging in the F444W, F210M, and F182M filters. The NGDEEP observations include NIRISS WFSS R-grism and C-grism in the F200W, F150W, and F115W, with direct imaging in the F200W, F150W and F115W NIRISS filters. The combined data products cover a spectral wavelength range $\lambda_{\text{obs}} \in [1.0 - 2.2] \cup [3.1, 5.0] \mu\text{m}$, enabling redshift coverage $z \in [1.3, 3.5] \cup [5.3, 9]$ for $[\text{O III}]$ emitters.

The ASPIRE imaging is processed in the same way as described in F. Wang et al. (2023); J. Yang et al. (2023). Briefly, the reduction was performed using version 1.8.3 of the JWST Calibration Pipeline with the reference files from version 11.16.15 of the standard Calibration Reference Data System. After Stages 2 and 3, the images are aligned to Gaia DR3 and drizzled to a common pixel scale of $0''.031/\text{pixel}$. For the FRESCO and NGDEEP samples, we use the public image products including NIRCcam and NIRISS retrieved from the Dawn JWST Archive (DJA)²⁵. We use JWST Calibration pipeline CALWEBB Stage 1 to calibrate individual NIRCcam WFSS exposures, with reference files `jwst_1090.pmap`. The $1/f$ noise is then subtracted using the routine described in F. Wang et al. (2023). The world coordinate system (WCS) information is assigned to each exposure with `assign_wcs` step. The flat field is done with CALWEBB stage-2. We build the median backgrounds for the F356W and F444W filters based on all ASPIRE and FRESCO WFSS exposures, which are

²⁵ <https://dawn-cph.github.io/dja/>

then scaled and subtracted from each individual exposure. We then measure the astrometric offsets between each of the short wavelength (SW) images and the fully calibrated direct mosaic to align each grism exposure with the direct image.

The preprocessed NIRC*am* WFSS exposures are then processed with the Grism Redshift & Line Analysis tool (GRIZLI, G. Brammer et al. 2022). We use the spectral tracing, grism dispersion, and sensitivity models described in F. Sun et al. (2023). The detection catalog for spectral extraction is built from the F356W (F444W) direct image for ASPIRE (FRESCO), and the continuum cross-contamination is subtracted by GRIZLI forward modeling using the reference image as the reference image for each grism exposure. The emission line maps are drizzled from the 2D grism to the image plane, matching the wcs of direct imaging, with `pixfrac` = 1 and pixel size = 0''.06, to properly sample the NIRC*am* PSFs (FWHM=0''.115~0''.145).

The NIRISS WFSS reduction is done similarly, with reference files `jwst_1090.pmap` by GRIZLI full end-to-end processing, including CALWEBB Stage 1 calibration from raw exposures, flat fielding, $1/f$ noise subtraction, sky subtraction, astrometry alignment. The contamination modeling and extraction of the spectra are performed with the latest GRIZLI NIRISS configuration file (J. Matharu & G. Brammer 2022). The emission line maps are drizzled from the 2D grism to the image plane with `pixfrac`=1 and pixel size = 0''.03, for properly sampling NIRISS PSFs (FWHM=0''.040~0''.066).

2.2. Sample selection

We apply the emitter finder algorithm detailed in F. Wang et al. (2023) to select galaxies with possible [O III] emission lines. Briefly, the algorithm first searches for peaks in 1D spectra and, assuming every peak as a candidate [O III] λ 5008, measures the SNR at the expected position of [O III] λ 4960. A good candidate has $\text{SNR}_{[\text{O III}]\lambda 4960} > 2$ and a color excess in the corresponding image band. We note that there are $z > 5$ [O III] emitters in ASPIRE and FRESCO that only have [O III] λ 5008 detection because the [O III] λ 4960 is too faint to be detected. We have ignored the sources where [O III] λ 4960 is not detected because they will decrease the SNR in our stack. We remove candidates with cross-contamination in the 2D spectra by visual inspection. Since we only have [O III] and $\text{H}\beta$ detection for our sample at $z > 5$, we have assumed the lower branch of the R3 relation when converting [O III]/ $\text{H}\beta$ ratio to metallicity. The measurements are unreliable if high-metallicity galaxies are mixed with the low-metallicity sample. One solution is to use the mass-

metallicity relation to estimate the metallicity of galaxies and ensure the applicability of choosing the lower branch solution. A. Sarkar et al. (2024) provided an empirical mass-metallicity-redshift relation formulated as: $12 + \log(\text{O}/\text{H}) = 6.29 + 0.237 \times \log(M_*/M_\odot) - 0.06 \times (1+z)$. From this relation, galaxies at $5 < z < 9$ with stellar masses $\log(M_*/M_\odot) \lesssim 9$ are expected to have metallicities $12 + \log(\text{O}/\text{H}) \lesssim 7.9$. We find that most of our sample galaxies are below $\log(M_*/M_\odot) = 9$. However, the ASPIRE and FRESCO samples still include a small fraction of higher-mass galaxies, with 12.6% and 4.1%, respectively. To eliminate the bias of metallicity estimation by massive galaxies, we have removed galaxies with $\log(M_*/M_\odot) > 9$ in our $z > 5$ sample, and the low-mass sample includes 284 and 47 galaxies in ASPIRE and FRESCO, respectively. Since there is still a considerable number ($N = 41$) of massive $\log(M_*/M_\odot) > 9$ galaxies in ASPIRE, we construct an additional massive sample with those galaxies, and we can measure their metallicity assuming the R3 upper branch solution (see Section “Metallicity gradients in mass bins”). Since we only have two galaxies with $\log(M_*/M_\odot) > 9$ in FRESCO, which is insufficient to do statistical study, we do not keep a $\log(M_*/M_\odot) > 9$ bin in FRESCO.

In the NGDEEP sample, we additionally require the detection of [O III], [O II], and $\text{H}\beta$, with the detection of either $\text{H}\alpha$ or $\text{H}\gamma$, to ensure the usage of both the R3 and R2 indices and usage of a reliable dust correction using the Balmer decrement. We have a SNR cut of three for both [O III] and [O II], which has been shown to yield reliable metallicity gradient measurements (X. Wang et al. 2020).

In our galaxy sample, we incorporate 89 galaxies traced by [O III] with high SNR at $1.7 < z < 3.5$ in NGDEEP, 325 galaxies at $5.3 < z < 7$ in ASPIRE, and 42 galaxies at $7 < z < 9$ in FRESCO GOOD-S and GOOD-N. From line ratio diagnostics, these galaxies are negligibly impacted by AGN contamination (see Appendix I).

From SED modeling, the stellar masses in NGDEEP range from $10^7 M_\odot$ to $10^{10} M_\odot$ with a median mass of $10^{8.43} M_\odot$, and the stellar masses in ASPIRE and FRESCO range from $10^7 M_\odot$ to $10^{10} M_\odot$ with a median mass $10^{8.16} M_\odot$ (Table 4). We use the oxygen-to-hydrogen abundance ratio, commonly expressed as $12 + \log(\text{O}/\text{H})$ as a proxy for gas-phase metallicity. We determine the metallicity of the gas in different regions of galaxies by analyzing the emission lines produced by hydrogen (e.g., $\text{H}\gamma$ and $\text{H}\beta$) and oxygen (e.g., [O II] and [O III]). These ratios serve as diagnostic indicators of metallicity. For sample galaxies at $1.7 < z < 3.5$, we use F. Bian et al. (2018) calibration, widely used for rel-

actively lower redshift galaxies. At $z > 5$, we use the calibration of R. L. Sanders et al. (2024), applicable for high-redshift galaxies including metal-poor galaxies. Note that the difference between the two calibrations is small and the metallicity gradients at $z > 5$ would change by less than 10% if we used F. Bian et al. (2018) for $z > 5$ sample. Such systematics are smaller than typical statistical uncertainties and do not impact evolutionary studies of the galaxy metallicity gradient.

Because of the low signal-to-noise ratio in our sample galaxies at $z > 5$, we are able to determine metallicity gradients for only six galaxies (Fig. 23). To increase the SNR of the galaxy sample at $z > 5$, we in addition applied a median stack for galaxies in ASPIRE and FRESCO, corresponding to two redshift bins of $5.3 < z < 7.0$ and $7.0 < z < 9.0$. We show the metallicity gradients measured in the stacks at $z = [5, 7]$ and $z = [7, 9]$ in Fig. 1. Since single galaxies in $1.7 < z < 3.5$ have a higher SNR, we can measure the metallicities for individual galaxies without stacking. We use the flux ratio of diagnostic [O III] to $H\beta$ (R3) for $z > 5$ stacks and we use [O III], [O II], $H\beta$, and $H\gamma$ to jointly constrain metallicity in the sample at $1.7 < z < 3.5$. To ensure the consistency between the measurements on individual galaxies and stacks, we also applied the same median stack for the NGDEEP sample at two redshift bins of $1.7 < z < 2.3$ and $2.3 < z < 3.5$, and the metallicity gradients from stacked emission maps are consistent with the median of individual measurements.

2.3. Photometric catalog

The sources in ASPIRE are identified using F356W as the detection image. Photometry is measured using SourceExtractor++ in F115W, F200W, and F356W after matching the PSFs to that of F356W ($0''.1$). Fluxes measured in Kron apertures with ($k=1.2$, $R=1.7$) are corrected to total magnitudes using the ratio for Kron fluxes measured in larger apertures ($k = 1.5$, $R = 2.5$). The uncertainties for each source’s photometry are measured by placing 1000 random apertures the size of the Kron aperture across the image and measuring the root mean square (RMS).

For the FRESCO and NGDEEP samples, we use the public catalogs retrieved from the Dawn JWST Archive (DJA). The fluxes are corrected to total fluxes.

3. METHODS

3.1. Stacking emission maps

We create median maps of [O III] and $H\beta$ by stacking individual galaxies in two redshift bins. As the galaxies in our sample have been observed under uniform conditions, and have stable PSFs, stacking gives us the ad-

vantage of not requiring individual emission lines to be detected with high SNR. The stacked maps allow us to explore the regions with larger radii and lower surface brightness. We first weight each map by [O III] flux measured in the 1D spectrum, to avoid excessive weighting toward bright sources (E. J. Nelson et al. 2016; X. Wang et al. 2022b). Before stacking the galaxies, we do not distort the maps either by rescaling, rotating, or deprojecting, to not introduce additional noise and systematics. We use DAOSTARFinder to fit the centroid of each galaxy’s emission map using a Gaussian kernel, and then stack the centrally aligned emission maps. Several relevant works also measure centers based on emission lines (N. M. Förster Schreiber et al. 2009; E. Wuyts et al. 2016; N. M. Förster Schreiber et al. 2018), although different methods may be applied. For example, N. M. Förster Schreiber et al. (2018) define the galaxy center as the morphological center of the outer isophote of the emission line map. An alternative approach is to fit the center based on the continuum, but we did not find a significant difference in the stacked line profiles. We create median stacks by measuring the median value at each pixel. The uncertainties of the radial profiles are computed by bootstrapping the stacks. The physical sizes of the stacks are computed using the median redshift $z = 6.28$ and $z = 7.24$ in ASPIRE and FRESCO stacks, respectively. The stacked results are presented in the third panel of Fig. 1.

3.2. SED fitting

The SED modeling of our sample is performed with the Bayesian code BEAGLE (J. Chevallard & S. Charlot 2016) with the broadband photometry and flux of [O III] lines as inputs. We adopt a delayed- τ star formation history (SFH), the SMC dust attenuation law, and a Chabrier initial mass function (IMF) (G. Chabrier 2003) with an upper limit of $100M_{\odot}$. We assume a flat prior in log-space for the characteristic star formation timescale, τ , spanning from 10^7 to $10^{10.5}$ years, and for stellar masses from 10^4M_{\odot} to $10^{12}M_{\odot}$. We set the optical depth in the V band to vary from 0 – 0.5 in log-space. In FRESCO, the spectral fitting is performed using three JWST NIRCам bands (F182M, F210M, and F444W) and eight HST bands (F435W, F606W, F775W, F810W, F105W, F125W, F140W, F160W). For the NGDEEP galaxy sample, we used eight JWST NIRCам bands (F090W, F182M, F210M, F277W, F335W, F356W, F410M, F444W), three JWST NIRISS bands (F115W, F150W and F200W), and eight HST bands (F435W, F606W, F775W, F810W, F105W, F125W, F140W, F160W). For ASPIRE, we used three JWST NIRCам bands (F115W, F200W, F356W). We note

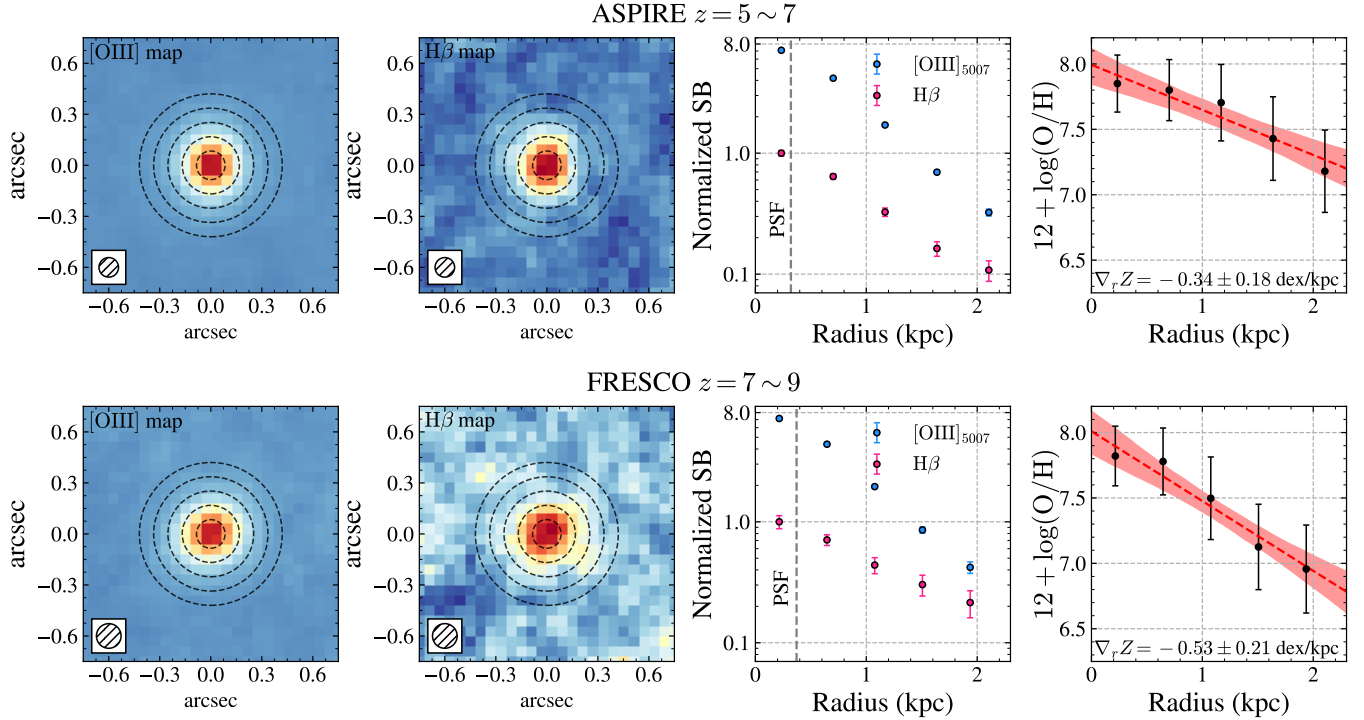


Figure 1. Stacking results of $5 < z < 7$ galaxies in ASPIRE (top) and $7 < z < 9$ galaxies in FRESCO (bottom). The first two columns show the median stack of emission maps ([O III], H β). The FWHM of PSFs are shown on the bottom left in each line map. The third column shows the surface brightness (SB) profiles of [O III] and H β , normalized by the peak H β flux. The vertical dashed line marks the angular resolution (half of PSF FWHM). The fourth column shows the fitted metallicity gradient. The black error bars include both statistical error and calibration error. The red shadow represents the 1σ confidence interval of the linear regression. Both samples in each redshift bin show steep gradients towards the center.

that for the ASPIRE and FRESCO samples, we lack photometric bands (e.g., JWST MIRI) to fully constrain the SED shape redward of the 4000 Å break, which is sensitive to age and dust properties of stellar populations. This leads to uncertainties for the derived physical properties. Q. Li et al. (2024) found stellar mass and SFR uncertainties can increase by ~ 0.1 dex without MIRI coverage. Although the SED code gives small errors on stellar masses, they only represent model-based statistical uncertainty. There are also notable systematic uncertainties in the assumed models, including star formation history, initial mass function, and dust attenuation laws. Stellar masses of young galaxies can differ significantly with different SFH. Since young stars dominate the observed rest-UV and optical SED, they outshine potential older stellar populations that may be present. Consequently, the inferred early star formation history, along with the estimated age and stellar mass of a given system, can be sensitive to the choice of SFH model. The parametric SFH like constant SFH tends to underestimate the stellar masses compared with non-parametric SFH, as they are not flexible enough to capture early star formation (L. Whitler et al. 2023; M. A. C. de los Reyes et al. 2024). Since many recent

works on mass-metallicity relations have adopted parametric SFH to estimate stellar masses (J. Matthee et al. 2023; M. Curti et al. 2024; A. Sarkar et al. 2024), and our sample selection directly relies on the MZR provided by A. Sarkar et al. (2024), the adherence of parametric SFH model can be more consistent to with their formalism.

3.3. Metallicity measurements

We jointly constrain metallicity, nebular dust extinction (A_v), and de-reddened H β flux ($f_{H\beta}$), by the Bayesian inference method for forward modeling (Z. Li et al. 2022; X. Wang et al. 2017). The likelihood function is defined as

$$\mathcal{L} \propto \exp \left(-\frac{1}{2} \cdot \sum_i \frac{(f_{\text{EL}_i} - R_i \cdot f_{H\beta})^2}{(\sigma_{\text{EL}_i})^2 + (f_{H\beta})^2 \cdot (\sigma_{R_i})^2} \right), \quad (1)$$

where f_{EL_i} and σ_{EL_i} represent the de-reddened emission-line (e.g., [O III], [O II], H γ , H β , H α) flux. R_i corresponds to the expected line-flux ratios between EL $_i$ and H β (i.e., R_i can be the Balmer decrement of H γ /H β = 0.6, H α /H β = 2.86, assuming case B recombination, and the metallicity diagnostics of [O III]/H β and [O II]/H β), and σ_{R_i} is their intrinsic scatter. We

perform MCMC sampling using the package EMCEE (D. Foreman-Mackey et al. 2013). Potential stellar absorption may impact the dust corrections. The typical equivalent width of $H\beta$ is found to be $EW(H\beta) \sim 1 - 6 \text{ \AA}$ in local $H\beta$ absorption line galaxies (R. M. McDermid et al. 2015). A. C. Carnall et al. (2023) reported $EW(H\delta) = 7.9 \text{ \AA}$ for a quiescent galaxy at $z = 4.658$. However, for star-forming galaxies dominated by young O and B stars, the equivalent widths of Balmer absorption lines are much weaker. The low-mass star-forming galaxies are found to exhibit high $[O \text{ III}]$ and $H\beta$ equivalent width both at $z \sim 2$ and higher redshift $z \sim 6$ (A. van der Wel et al. 2011; J. Matthee et al. 2023), with $H\beta$ emission reaching $EW(H\beta) \sim 100 \text{ \AA}$. The Balmer absorption line-strength contributes only to $\sim 1 - 10\%$ of emission line-strength and can be negligible. Several recent works also correct for dust by the observed Balmer emission line ratios without taking stellar absorption into account (M. Curti et al. 2023; J. Matharu et al. 2023).

For the $z > 5$ galaxy sample, we adopt the metallicity diagnostics presented by (R. L. Sanders et al. 2024). R. L. Sanders et al. (2024) built the empirical calibration using a sample of $z = 2 - 9$ galaxies with $[O \text{ III}]\lambda 4363$ detected using the direct T_e method, which better characterizes the properties of high-redshift galaxies. We also refer to D. Scholte et al. (2025); P. Chakraborty et al. (2025) who provide similar T_e calibrations. One caveat for the $[O \text{ III}]/H\beta$ (R3) diagnostics is that it yields a double-branched solution if given a line ratio. For our NGDEEP sample, we have detections of both $[O \text{ II}]\lambda 3727$ and $[O \text{ III}]\lambda 5007$. With the additional $[O \text{ II}]\lambda 3727$ we can distinguish the two solutions using $[O \text{ II}]\lambda 3727/H\beta$ (R2). However, in the ASPIRE and FRESCO sample, $[O \text{ II}]\lambda 3727$ is out of the spectral coverage. Thus we assume the lower branch solution with $12 + \log(O/H) \lesssim 7.9$, given the fact that most galaxies at similar redshifts of $z \geq 6 - 7$ have had their metal-poor nature verified using the T_e method (R. L. Sanders et al. 2024; M. Curti et al. 2023; K. Nakajima et al. 2023; J. R. Trump et al. 2023; T. Jones et al. 2023; P. Chakraborty et al. 2025).

We rely on the strong-line diagnostics from F. Bian et al. (2018) for sample galaxies at $1.7 < z < 3.5$, which was built from local analogs of $z \sim 2$ galaxies. As R. L. Sanders et al. (2024) is built from a sample of high-redshift galaxies with direct metallicity measurements, it is more applicable for our sample of relatively metal-poor $z > 5$ galaxies. However, this model does not well constrain potential higher metallicity galaxies as their calibration is fitted with insufficient numbers of high metallicity galaxies. Because of this issue with R. L.

Sanders et al. (2024), we choose to use F. Bian et al. (2018) as it is robust for higher metallicity galaxies and is widely used for galaxies at $z \approx 2$ (X. Wang et al. 2020).

In Appendix E, we test the systematic uncertainties arising from different strong-line calibrations and find that alternative methods (R. Maiolino et al. 2008; M. Curti et al. 2023; K. Nakajima et al. 2022) yield consistent metallicity gradient measurements with our fiducial measurements using R. L. Sanders et al. (2024) and F. Bian et al. (2018).

3.4. Gradient measurements

To securely measure metallicity gradients in the NGDEEP sample, we apply Voronoi tessellation (M. Cappellari & Y. Copin 2003) to each galaxy’s $[O \text{ III}]$ map to bin emission maps into subregions, each having $S/N > 5$ in $[O \text{ III}]$. Such an SNR cut is tested to recover robust gradient measurements (X. Wang et al. 2020). The Voronoi tessellation is superior to averaging the signal in radial annuli because the former keeps the information of azimuthal variations in metallicity. However, for our stacked sample, the azimuthal variations have already been averaged during stacking, so we simply average the flux in different annulus for $z > 5$ samples.

We use a simple linear least-square method to fit the metallicity gradients with the following formula:

$$12 + \log(O/H) = \theta_0 + \theta_1 r \quad (2)$$

where θ_0 is the intercept, θ_1 is the slope of the fitted line, and r is the galactocentric radius in kiloparsecs.

For the NGDEEP galaxies, we de-project the radius to the source plane. We assume the galaxies are circular disks, and the observed elasticity is due to projection effects. The inclination angle, i , is estimated by the axis ratio from Sérsic fitting: $\cos(i) = b/a$. The distance of each position to the center is then corrected by inclination. We note the assumption of disks may not apply for every galaxy at high-redshift, especially given the recent discovery of less disk galaxies towards high-redshift (R. C. Simons et al. 2017; V. Pandya et al. 2024). While some works have corrected for projection (Z. Li et al. 2022; X. Wang et al. 2020; N. M. Förster Schreiber et al. 2018), others directly use the projected distance to measure gradients (R. C. Simons et al. 2021; M. Curti et al. 2020b). We find a $\sim 0.1 \text{ dex kpc}^{-1}$ difference between the projected gradients and de-projected gradients, comparable to the 1-sigma statistical uncertainties. We use the de-projected results of NGDEEP sample throughout this article, to be consistent with our previous works (Z. Li et al. 2022; X. Wang et al. 2020).

Table 1. Metallicity gradients from median stacks in two $z > 5$ redshift bins.

Survey	Redshift	$\nabla_r \log(\text{O}/\text{H})$ [dex kpc $^{-1}$]
ASPIRE	$5.3 < z < 7.0$	-0.34 ± 0.18
FRESCO	$7.0 < z < 9.0$	-0.53 ± 0.21

The stacking method for the $z > 5$ sample averages the projection effects, so we do not correct for projection for the $z > 5$ sample.

The metallicity gradients measured from the median stacks are reported in Table 1, and the individual measurements of NGDEEP sample are reported in Table 4. In Figure 1, we show the measurements on median stacks, and the individual measurements of NGDEEP sample are shown in Figure 25. We note that the variation in R3 ratios could be due to the variation in ionization parameters (U) (P. Garg et al. 2024), which potentially leads to a bias in metallicity measurements. In Appendix H, we show that the variations in R3 ratios are more significant than can be accounted for by changes in the ionization parameter, and potential variation in U only leads to an uncertainty of ~ 0.1 dex kpc $^{-1}$. The steep gradients observed in Figure 1 are therefore robust.

4. RESULTS AND DISCUSSION

4.1. Redshift evolution of metallicity gradients

To have a more complete study of the evolution of the metallicity gradient, we have added existing measurements from a variety of sources, including a wealth of JWST observation (M. Ju et al. 2025), HST observations (X. Wang et al. 2017, 2020, 2022a; R. C. Simons et al. 2021) and ground-based adaptive optics (AO)-assisted observations (N. M. Förster Schreiber et al. 2018; T. Jones et al. 2013; A. M. Swinbank et al. 2012). These measurements are made mainly at $z \lesssim 2$. Additionally, we included samples obtained under seeing-limited conditions (L. van Zee et al. 1998; J. Queyrel et al. 2012; M. Curti et al. 2020b; D. Carton et al. 2018; E. Wuyts et al. 2016) for a more comprehensive analysis. Despite the fact that different metallicity calibrators (e.g., R23, N2, O3N2, R. Maiolino et al. 2008; M. Curti et al. 2020a) are used in different works, the systematic difference should not change the general trend in gradients (D. S. N. Rupke et al. 2010b; X. Wang et al. 2019), despite some potential impacts (H. Poetrodjojo et al. 2021). The collected literature sample covers the redshift range $0 < z < 2.5$.

Note that our $z > 6$ results are different from that of recent JWST NIRSpec observations by G. Venturi et al.

(2024) (Fig. 2). The results in G. Venturi et al. (2024) are based on the gradient measurement of four galaxies at $z > 6$, selected with the largest offset between UV/optical and far-infrared emission lines S. Carniani et al. (2021). Such offsets may indicate nontypical dust geometry and/or galactic structures so that the dust and star-forming regions are not uniformly distributed, possibly induced by merger events. Thus, their sample is different from our galaxy sample on main sequence. These interacting systems are expected to undergo violent gas mixing (P. B. Tissera et al. 2022), and, as such, the metal distribution is expected to be flatter than normal star-forming galaxies. These effects are likely to explain the differences with our sample. Thus, we have not included these systems in our high-redshift sample for statistical analysis.

In Fig. 2, we show the redshift evolution of the metallicity gradients from $z = 8$ to $z = 0$. We see that the cosmic evolution of the metallicity gradient shows ascending and descending phases before and after $z \approx 2$. Galaxies show steep negative gradients at the earliest times ($z > 5$). Such a steep gradient has been found in local extremely metal-poor galaxies (EMPGs, Y. Kashiwagi et al. 2021) and is indicative of inside-out growth and inefficient gas mixing. The metallicity gradients flatten over time until $z \sim 2$ and steepen again toward the present. To describe this trend, we first applied a linear regression analysis for individual galaxies. We divide the individual galaxies into two redshift bins, $1.75 < z < 3.5$ and $0 < z < 1.75$. The ascending phase with time can be described as -0.046 ± 0.012 dex kpc $^{-1}/\delta z$ from $z = 3.5$ to $z = 1.75$, followed by a descending phase of 0.040 ± 0.006 dex kpc $^{-1}/\delta z$ from $z = 1.75$ to $z = 0$. We applied the likelihood-ratio test to see if this evolution is significant compared with a non-evolving metallicity gradient. We find a p -value = 1.3×10^{-22} , indicating a strong preference for the model with redshift evolution.

To better characterize the rising and descending phases for the metallicity gradients we applied a double power law model:

$$\nabla_r \log(\text{O}/\text{H})(z) = \gamma_0 \frac{(1+z)^{\gamma_1}}{1 + [(1+z)/\gamma_2]^{\gamma_3}} - \gamma_4 \quad (3)$$

Fitting the above function to our observed data (Appendix D), we obtain the following constraints: $\gamma_0 = 0.40^{+0.30}_{-0.19}$, $\gamma_1 = 0.27^{+0.16}_{-0.09}$, $\gamma_2 = 5.17^{+1.15}_{-0.59}$, $\gamma_3 = 5.23^{+2.42}_{-2.01}$, $\gamma_4 = -0.50^{+0.20}_{-0.31}$. This fitting provides a first glimpse of the redshift evolution of the metallicity gradient with an ascending phase scaling as $\nabla_r \log(\text{O}/\text{H})(z) \propto (1+z)^{-5.23}$ at $2 \lesssim z \lesssim 8$, and transforms to a slowly descending phase to the present day, scaling as $\nabla_r \log(\text{O}/\text{H})(z) \propto (1+z)^{0.27}$. This analytical

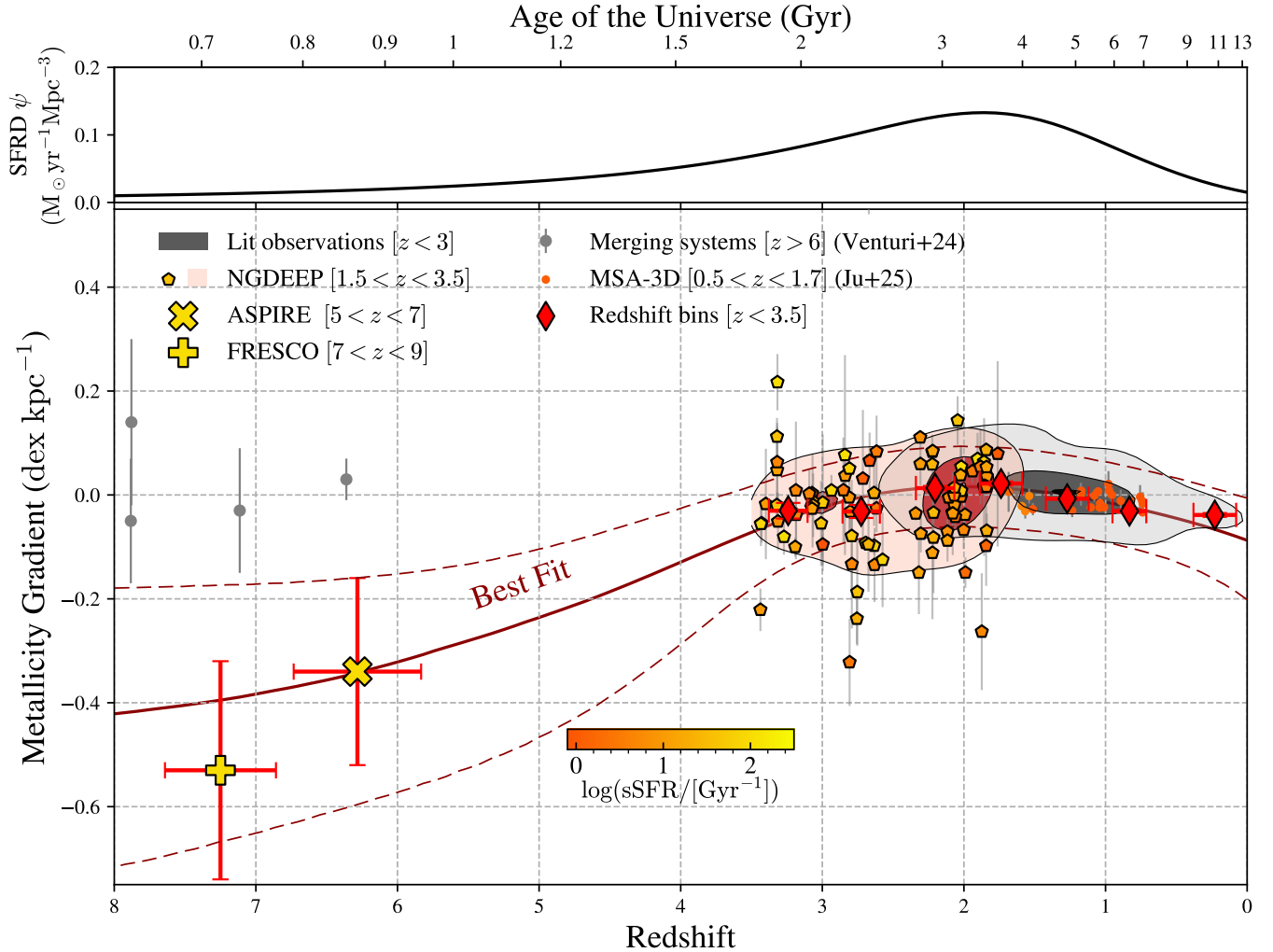


Figure 2. The redshift evolution of metallicity gradients. The thin red diamonds show the weighted mean in redshift bins at $z = [0, 3.5]$ from both this work and the literature. Red “x” and “+” represent the median stacks of the ASPIRE sample in $z \approx 6$ and FRESCO sample in $z \approx 7$. The NGDEEP sample at $z \approx 1 - 3$ is denoted by pentagons, color-coded by sSFR. Gray contours encompass individual measurements at $z < 3$ in the literature using HST (X. Wang et al. 2017, 2020; R. C. Simons et al. 2021), and ground-based AO-assisted surveys (A. M. Swinbank et al. 2012; T. Jones et al. 2013; N. M. Förster Schreiber et al. 2018). We also include seeing-limited observations (L. van Zee et al. 1998; J. Queyrel et al. 2012; M. Curti et al. 2020b; D. Carton et al. 2018; E. Wuyts et al. 2016). The red contour only encompasses our observations at $1.7 < z < 3.5$, overlapping with literature observations at $z \sim 2$. Gray circles with error bars represent interacting galaxies at $z > 6$ recently observed with JWST NIRSpec (G. Venturi et al. 2024). Recent JWST MSA-3D observations (M. Ju et al. 2025) are noted in circles color-coded by sSFR. The dark-red line shows our best fitting of all stacks, with dashed lines in the same color showing the 1σ confidence interval of the fit. In the upper panel, we plot the cosmic star formation rate density (SFRD (P. Madau & M. Dickinson 2014)), where the evolution of metallicity gradients also peaks at $z \sim 2$.

form suggests the transition to happen around $z \approx 2.1$. Intriguingly, it is close to the peak of SFRD (P. Madau & M. Dickinson 2014). Similar transitions at the same epoch include the break of fundamental metallicity relation (M. Curti et al. 2024) at $z > 2$ and the break of mass-metallicity relations of damped Lyman alpha systems (DLA) at $z > 2.6$ (P. Møller et al. 2013). They point to certain mode transitions about galaxy formation and chemical enrichment at cosmic noon.

Since galaxies are intrinsically smaller at higher redshift (T. Morishita et al. 2024), a fixed metallicity change implies steeper gradients in smaller systems. Given the correlation between galaxy size and stellar mass, expressing gradients relative to the effective radius R_e helps reduce dependence on mass and size (I. T. Ho et al. 2015; F. Bresolin 2019). In addition, the normalization of effective radius helps reduce the impact from beam-smearing effects of seeing limited data (E. Wuyts

et al. 2016). In Appendix B, we discuss the metallicity gradients measured with effective radius, and the trend of redshift evolution is consistent.

4.2. Comparison with hydrodynamical simulations

In Fig. 3, we compare our observations with simulations from MUGS (B. K. Gibson et al. 2013), MAGICC (B. K. Gibson et al. 2013), FIRE (X. Ma et al. 2017), FIRE-2 (X. Sun et al. 2024), TNG50 (Z. S. Hemler et al. 2021), EAGLE (P. B. Tissera et al. 2022), FOGGIE (A. Acharyya et al. 2025), and Illustris (A. M. Garcia et al. 2025). Those simulations adopt different settings for physical processes, including the treatment of feedback (See Appendix K).

In the FOGGIE simulation, the galaxies start with steep gradients at $z = 6$ and evolve to shallower gradients over time, with a trend similar to our observations from $z > 5$ to $z \sim 2$, although they predict overall steeper gradients. They attribute the flattening to an accretion-dominated phase towards $z \sim 1$. The Illustris simulation shows a similar trend as FOGGIE, in which the galaxies evolve initially with steep gradients and flatten over time. A. M. Garcia et al. (2025) obtained the redshift evolution from Illustris simulation as $-0.016 \pm 0.004 \text{ dex kpc}^{-1} \delta z$. In addition, from EAGLE (S. McAlpine et al. 2016), IllustrisTNG (D. Nelson et al. 2019) and SIMBA (R. Davé et al. 2019) simulations, A. M. Garcia et al. (2025) found similar redshift evolutions in the range of -0.015 to $-0.028 \text{ dex kpc}^{-1} \delta z$. While these values are broadly consistent with our observed ascending phase, the simulations do not reproduce the peaking gradients around $z \sim 2$. A. M. Garcia et al. (2025) suggest that simulations with smooth stellar feedback may not efficiently mix metals, which could contribute to the discrepancy between simulations and observations around $z \sim 2$.

At $z \lesssim 3$, our observations align more closely with the EAGLE, FIRE, FIRE-2, and MAGICC simulations, whereas TNG50 predicts slightly more negative gradients and MUGS yields overly steep gradients at $z \gtrsim 1$. Differences in the evolution of metallicity gradients in these simulations can be interpreted as a result of the use of different feedback models. The feedback drives outflows that transport metal-enriched gas to larger radii or out of the galaxy, meanwhile mix with metal-poor gas in the intergalactic medium (ISM). This process redistribute the metals and results in a flat metallicity gradient. The more bursty feedback in FIRE simulation produces flat gradients at $z \gtrsim 1$ (X. Ma et al. 2017), while the smooth feedback in TNG50 allows for more negative gradients (Z. S. Hemler et al. 2021). MAGICC is a variation of MUGS simulation, running with

the same code, except for the enhanced thermal feedback energy from SNe and the inclusion of radiation from massive stars in MAGICC simulation (B. K. Gibson et al. 2013). The enhanced feedback schemes in MAGICC produces more flat gradients at $z \sim 2$. However, the redshift evolution in the FIRE simulations is less evident, as they exhibit consistently flat gradients across all redshifts, likely due to the episodic nature of the strong feedback model used in FIRE (X. Ma et al. 2017; X. Sun et al. 2024). EAGLE simulations also suggest that galaxy mergers or interactions that trigger gas inflows and starbursts could flatten or invert metallicity gradients (P. B. Tissera et al. 2022). Therefore, the observed metallicity gradients at $z \sim 2$ generally prefer models with strong feedback as a consequence of bursty star formation, though the feedback strength should not result in persistently flat gradients. Thus, the evolution of metallicity gradient indicate an evolving feedback strength through cosmic time. There is evidence that the energy and momentum injection from massive stars peaks at $z \approx 2$ (T. M. Heckman & P. N. Best 2023). At this redshift, outflows are found to efficiently redistribute large proportions of metals from galaxies (R. L. Sanders et al. 2023), leading to flat/positive gradients (X. Wang et al. 2019). After this epoch, feedback strength should diminish as a consequence of decreased star formation rate (S. Yu et al. 2023), allowing negative gradients to develop.

In addition to outflow launched by feedback, inflows due to cosmic gas accretion from the intergalactic medium (IGM) may also mix with the ISM gas and redistribute metal contents. Cosmic accretion history in simulations suggests that cold-mode accretion dominates the total accretion rate at $z \sim 2$, and hot-mode accretion becomes increasingly important at lower redshifts (D. Kereš et al. 2009; F. van de Voort et al. 2011). At these lower redshifts, hot-mode accretion forms a shock shell around the massive halos $M_h \gtrsim 10^{12} M_\odot$ (Y. Birnboim & A. Dekel 2003; A. Dekel et al. 2009). As the cooling time is longer than the infall time, the shock-heated gas cannot cool and collapse inward efficiently, thereby limiting its ability to readily fuel star formation. However, the cold-mode accretion is predicted to penetrate deep inside the halo without being shock-heated because the cooling time is shorter than the shock compression time. Such cold flows reduce the metallicity in the galactic center via filaments penetrating halos, which causes the flattening/inverting of the metallicity gradients at cosmic noon (G. Cresci et al. 2010; Z. Li et al. 2022).

The joint effect of feedback and gas accretion may contribute to the flat/positive gradients observed during

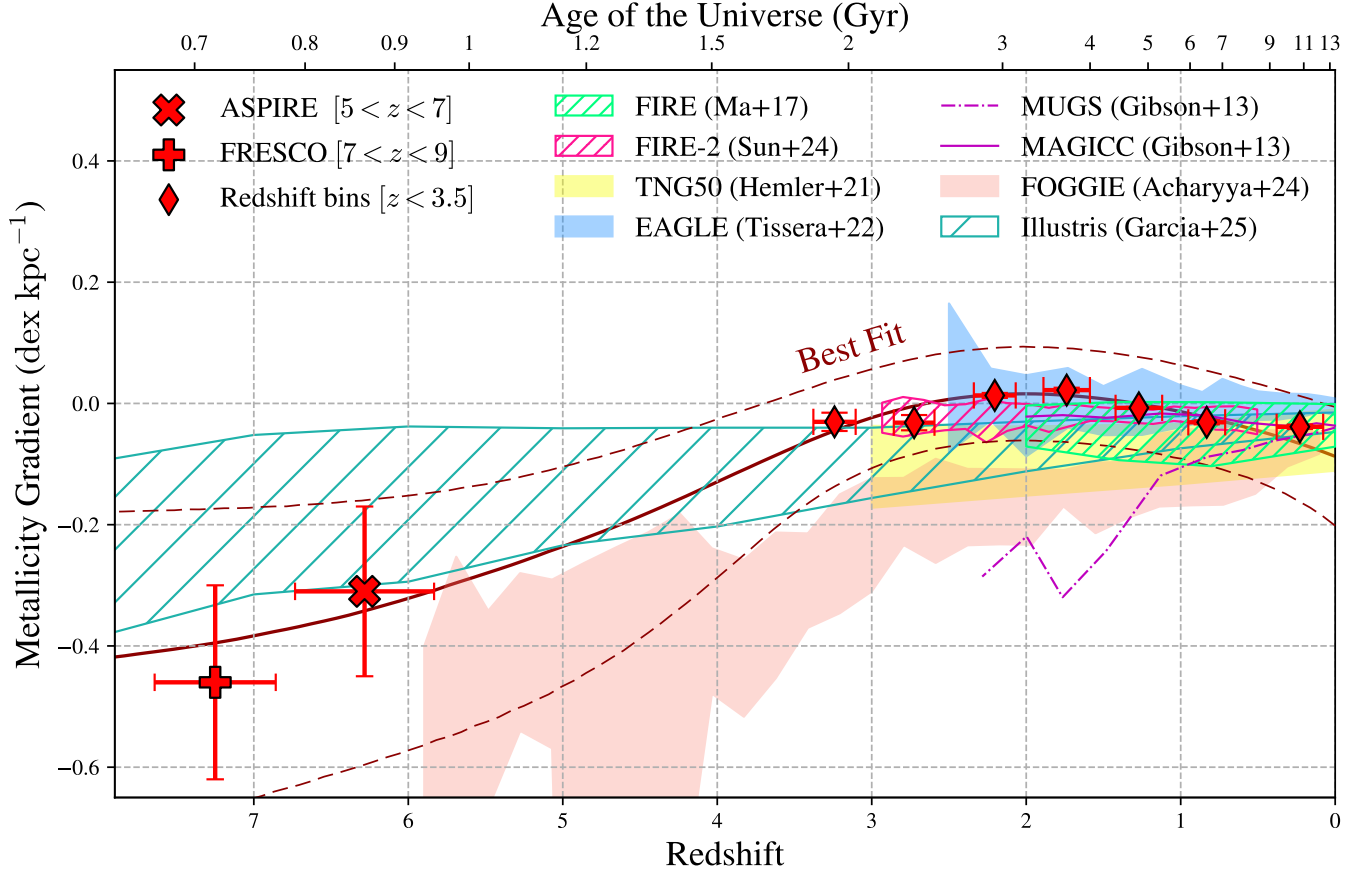


Figure 3. The comparison between the observed best-fit redshift evolution of metallicity gradients and predictions from different suites of cosmological simulations. The simulations including FIRE (X. Ma et al. 2017), FIRE-2 (X. Sun et al. 2024), TNG50 (Z. S. Hemler et al. 2021), EAGLE (P. B. Tissera et al. 2022), MUGS/MAGICC (B. K. Gibson et al. 2013), FOGGIE (A. Acharyya et al. 2025), and Illustris (A. M. Garcia et al. 2025) are marked in different colors.

cosmic noon. In contrast, measurements at $z \sim 6 - 8$ reveal steeper gradients compared to galaxies at $z \sim 2$, possibly indicating reduced gas mixing at cosmic dawn allowed for the existence of steeper gradients in early galaxies. Recent works have revealed numerous instances of star-forming galaxies that deviate from the main sequence of the fundamental metallicity relation (FMR) established at $z \lesssim 2$ (M. A. Lara-López et al. 2010). These deviations, characterized by significant metal deficiency at $z \gtrsim 7$ (K. E. Heintz et al. 2023; K. Nakajima et al. 2023), imply a continuous pristine gas inflow that effectively dilutes the metal abundances in these galaxies. With continuous gas inflow diluting galaxies, steep metallicity gradients may exist when star formation efficiency is high and the local metal production is high at the center. Theoretical models (E. Wang & S. J. Lilly 2022; P. Sharda et al. 2021b) have suggested the importance of in situ metal production in building negative metallicity gradients. The observed negative metallicity gradients suggest that in situ star formation and metal production, driven by intense cen-

tral starbursts, may dominate the metal distribution, while metal mixing by gas inflows and feedback-driven outflows likely plays a minor role.

At low-redshift ($z \lesssim 1$), metallicity gradients tend to become negative again. The underlying mechanisms likely differ from those at $z > 5$, as star formation is significantly suppressed in hot halos at $z = 0$, due to inefficient cooling (F. van de Voort & J. Schaye 2012; C. A. Correa et al. 2018) and reduced gas accretion rate (A. van der Wel et al. 2011; C.-A. Faucher-Giguère et al. 2011). From FIRE-2 simulation, R. L. Graf et al. (2024) suggest that as galaxies evolved, declining gas accretion (C. W. Trapp et al. 2022), reduced star formation (S. Yu et al. 2023) and feedback (M. E. Orr et al. 2022), and the settling of disks with reduced velocity dispersion and gas turbulence (J. C. Bird et al. 2021) led to a reduction in metal mixing, allowing negative gradients to develop and persist. Comparing observations in the local Universe and at $z \sim 2$ highlights a transition from strong turbulence, gas inflows, and feedback-driven mix-

ing at high-redshift to more settled, secular evolution by $z \sim 0$.

4.3. Mass-Metallicity Gradient Relation (MZGR)

We explore how metallicity gradients change with galaxy mass, in terms of mass-metallicity gradient relation (MZGR, also see M. Spolaor et al. 2009; P. Sharda et al. 2021a). We divided our FRESCO, ASPIRE samples into different mass bins and applied the same stacking method (Appendix A, Fig. 9, 10).

In Fig. 4, we show the metallicity gradients as a function of stellar mass (Mass-Metallicity Gradient Relation, MZGR), and compare the observations with the FIRE (X. Ma et al. 2017), TNG50 (Z. S. Hemler et al. 2021) and EAGLE (P. B. Tissera et al. 2022) simulations. The mass limits for JWST data in our work are deep enough to compare the change of metallicity gradients over redshift.

We observe that they follow distinct log-linear relations at $z \sim 2$ and $z > 5$. For galaxies at $z > 5$, we find a notable positive correlation in MZGR quantified as $\nabla_r \log(\text{O}/\text{H})_{5 < z < 9} = 0.30 \pm 0.19 \times \log(M_*/M_\odot) - 2.78 \pm 1.54$. This indicates that lower mass galaxies exhibit steeper negative gradients. However, literature data (gray contours) suggest a weak negative mass dependence of the metallicity gradient within the redshift range $0 < z < 3.5$. Our observations from the NGDEEP sample at $1.7 < z < 3.5$ also reveal a marginal anti-correlation, quantified as $\nabla_r \log(\text{O}/\text{H})_{1.7 < z < 3.5} = -0.020 \pm 0.018 \times \log(M_*/M_\odot) + 0.157 \pm 0.156$. This dependence on mass indicates the presence of different modes during those two periods.

A positive dependence on stellar mass is anticipated in secular galaxy evolution models, such that gradients flatten over time due to inside-out growth with the accumulation of stellar mass and metals (K. Pilkington et al. 2012). The positive mass dependence was previously observed in local galaxies (I. T. Ho et al. 2015; F. Bresolin 2019), which is also predicted by EAGLE simulations at $z = 0$ with weak feedback (magenta dashed line in Fig. 4, P. B. Tissera et al. 2019). W. M. Baker et al. (2024) also demonstrate the early signs of inside-out growth, with a galaxy at $z = 7.4$ that features a compact core and an extended star-forming disk, along with an increasing specific star formation rate (sSFR) as the radius increases. Our observed positive mass dependence further supports inside-out growth at cosmic dawn. The low-mass galaxies form earlier with concentrated cores and they grow outer disks with time, and they gradually accumulate masses and metal at larger radii. The flattening of metallicity gradients at high

masses highlights the dynamical view of galaxy growth at cosmic dawn.

On the other hand, a negative relation at $z \sim 1 - 2$ has been observed by X. Wang et al. (2020); S. Gillman et al. (2021); R. C. Simons et al. (2021), and they interpreted it as the effect of feedback-driven gas outflows, which is more pronounced in low-mass galaxies due to less restraint by lower gravitational potential (K. El-Badry et al. 2016; T. M. Heckman & P. N. Best 2023). FIRE simulations suggest that efficient gas outflow rates could efficiently mix metals causing significant fluctuations in metallicity gradients (X. Ma et al. 2017). A similar negative relation is also found in EAGLE simulations with enhanced SNe feedback (P. B. Tissera et al. 2019, see orange dotted line in Fig. 4). From TNG50 simulations, A. M. Garcia et al. (2023) indicates that when the enrichment timescale is shorter than the gas mixing timescale, galaxies can maintain steep gradients. Additionally, if feedback processes effectively generate high-velocity gas outflows and turbulence, this can reduce the gas mixing timescale, leading to shallower gradients. The flattening of metallicity gradients toward low-mass galaxies arises as the result of stronger feedback effects with lower gravitational potential. The two distinct MZGR at cosmic noon and cosmic dawn then indicate the weak feedback at $z > 5$ and strong feedback at $z \sim 2$.

4.4. Redshift evolution of MZGR

To further investigate whether the mass dependence of metallicity gradients evolves with redshift, we divide the sample of NGDEEP and literature observations into two four redshift bins, $z \leq 0.1$, $0.1 < z \leq 1.5$, $1.5 < z \leq 2.5$, and $2.5 < z \leq 3.5$. Specifically, we have included the measurements from the local universe at $z = 0$, reported by I. T. Ho et al. (2015); F. Bresolin (2019); T. Li et al. (2025). We perform a linear regression on these measurements using the package LINMIX (B. C. Kelly 2007), with errors on both metallicity gradients and stellar masses taken into account. The regression is formulated as:

$$\nabla_r \log(\text{O}/\text{H})(M_*) = \alpha + \beta \log(M_*/M_\odot) + N(0, \sigma), \quad (4)$$

where α is the intercept of the linear function and β is the slope of the linear function. $N(0, \sigma^2)$ represents a normal distribution with σ representing the intrinsic scatter about the regression in units of dex kpc^{-1} . T. Li et al. (2025) recently reported an inverted MZGR for low mass galaxies at $z = 0$ with $\log(M_*/M_\odot) < 9$, contrary to high mass trends. This turn-over pattern was also reported by F. Belfiore et al. (2017); H. Poettrich et al. (2021); A. H. Khoram & F. Belfiore (2025),

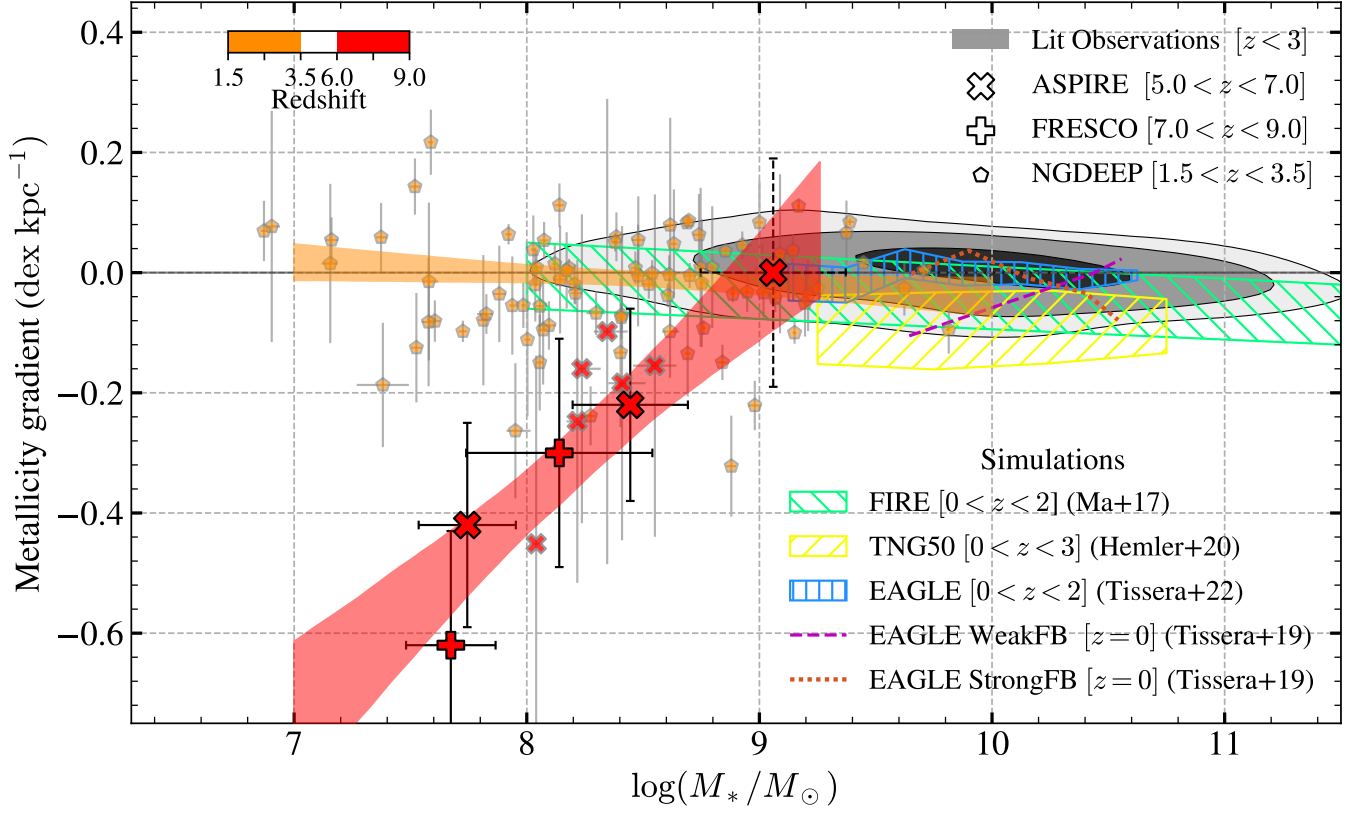


Figure 4. The mass dependence of metallicity gradients. Galaxies in NGDEEP, ASPIRE, and FRESCO are labeled with a pentagon, “x” and “+”, respectively, color-coded by redshift. The highest mass bin in ASPIRE is marked with a dashed error bar; for this bin, the metallicity gradients were derived using the higher-branch solution. The red and orange shaded areas represent the 1σ confidence intervals for the linear fit to the stacked data at $z > 5$ and the individual NGDEEP measurements within $1.5 < z < 3.5$, respectively. The literature observations (A. M. Swinbank et al. 2012; T. Jones et al. 2013; E. Wuyts et al. 2016; X. Wang et al. 2017; D. Carton et al. 2018; N. M. Förster Schreiber et al. 2018; X. Wang et al. 2020; M. Curti et al. 2020b; R. C. Simons et al. 2021; M. Ju et al. 2025) are included in gray-filled regions with 1, 2 and 3σ levels of the density contours of the distribution. Green, yellow, and blue hatched areas represent the 1σ interval from FIRE (X. Ma et al. 2017), TNG50 (Z. S. Hemler et al. 2021), and EAGLE (P. B. Tissera et al. 2022) simulations, respectively. The dashed magenta and dotted orange lines show the median metallicity gradients of EAGLE galaxies with strong feedback (StrongFB) and weak feedback (WeakFB) prescriptions (P. B. Tissera et al. 2019).

although the exact turnover point remains uncertain, in the range of $\log(M_*/M_\odot) \sim 9 - 10$. Here we assume the turnover point at $\log(M_*/M_\odot) = 9$ and divide the $z = 0$ sample into low mass ($\log(M_*/M_\odot) < 9$) and high mass ($\log(M_*/M_\odot) \geq 9$) bins, which are fitted separately. For higher-redshift observations, no compelling evidence of such a turnover pattern has been reported so far. Therefore, we perform a linear fit across the entire mass range for the other three high-redshift bins.

In Fig 5, we show the fitting results from the three redshift bins. The fitted parameters are shown in Table 2. In the local universe, the massive galaxies ($\log(M_*/M_\odot) > 9$) show a positive MZGR, indicating secular evolution. While for the finding of T. Li et al. (2025), we see that low mass galaxies ($\log(M_*/M_\odot) < 9$) exhibit a negative mass dependence. This suggests that

in the local universe, more massive, evolved galaxies predominantly undergo secular evolution, whereas low-mass dwarf galaxies remain influenced by metal mixing and transport processes, such as outflows driven by ongoing star formation. At redshift $z \sim 2$, we find the slopes are consistent with the value previously reported by X. Wang et al. (2020) for a sub-sample in the redshift range $1.2 < z < 2.5$. However, unlike local ($z = 0$) galaxies, the $z \sim 2$ population exhibits a negative MZGR within the same mass ranges. This negative MZGR suggests enhanced gas mixing due to feedback-driven wind at cosmic noon, as we have discussed in Section 4.3.

We find a mild evolution of MZGR slope β . The MZGR is positive at $z = 0$ for galaxies at $\log(M_*/M_\odot) > 9$, and it becomes negative at higher

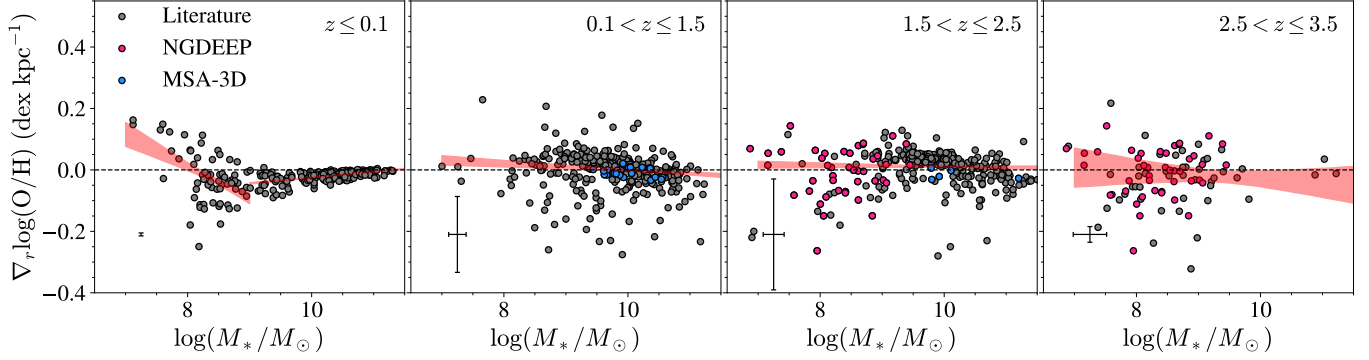


Figure 5. The mass-metallicity-gradient-relation for individual galaxies in four redshift bins. The red shadows represent the 1σ confidence interval of the linear regression. For $z \leq 0.1$ measurements, regressions are performed within two stellar mass bins: $\log(M_*/M_\odot) \leq 9$ and $\log(M_*/M_\odot) > 9$, while high-redshift measurements are performed across the entire mass range. The error bar on the left bottom of each figure represents median uncertainty in stellar masses and gradients. The pre-JWST observations are shown in gray circles (A. M. Swinbank et al. 2012; T. Jones et al. 2013; I. T. Ho et al. 2015; L. Sánchez-Menguiano et al. 2016; E. Wuyts et al. 2016; N. M. Förster Schreiber et al. 2018; D. Carton et al. 2018; F. Bresolin 2019; M. Curti et al. 2020b; R. C. Simons et al. 2021; T. Li et al. 2025); NGDEEP and recent JWST MSA-3D (M. Ju et al. 2025) observations are highlighted in red and blue, respectively.

Table 2. Fitted MZGR parameters in Eq. 4, and the Spearman coefficients (r, p).

Redshift	β [dex kpc $^{-1}$]	α [dex kpc $^{-1}$]	σ [dex kpc $^{-1}$]	r, p
$z = 0^a$	-0.100 ± 0.026	0.811 ± 0.218	0.063 ± 0.007	$-0.511, 0.000$
$z = 0^b$	0.019 ± 0.002	-0.211 ± 0.019	0.013 ± 0.001	$0.571, 0.000$
$0.1 < z \leq 1.5$	-0.009 ± 0.004	0.084 ± 0.037	0.036 ± 0.002	$-0.173, 0.002$
$1.5 < z \leq 2.5$	-0.002 ± 0.003	0.032 ± 0.029	0.031 ± 0.002	$0.027, 0.621$
$2.5 < z \leq 3.5$	-0.010 ± 0.022	0.064 ± 0.196	0.121 ± 0.015	$-0.060, 0.680$
$5.0 \leq z \leq 9.0^c$	0.304 ± 0.190	-2.784 ± 1.539	0.131 ± 0.125	$0.949, 0.014$

NOTE—^a Fitted within high mass bin $\log(M_*/M_\odot) \geq 9$. ^b Fitted within low mass bin $\log(M_*/M_\odot) < 9$. ^c In this redshift range, the MZGR is fitted on median stacks (Fig. 4)

redshifts. The significance of negative MZGR slope decreases with increasing redshift. At $z = 0$, The evolution of MZGR slope coincides with the evolution of the metallicity gradient (Fig. 2). This further indicates the evolution of feedback strength: with strong feedback at $z \sim 2$, the feedback promotes more positive gradients, meanwhile, it has a stronger impact on low-mass galaxies reflected in more negative MZGR. At higher redshift bins $2.5 < z \leq 3.5$, it starts to exhibit less negative MZGR, closer to the prediction without efficient outflows, and finally, the MZGR is significantly positive at $5.0 \leq z \leq 9.0$.

In Fig. 4, we show the mass distribution as a function of redshift in our sample. Since the galaxy sample is collected from a variety of works with different selection criteria, they have different stellar masses at different redshift bins. For example, the galaxies in $0.5 < z < 2.5$

bins are more massive (≈ 1 dex) than others, which corresponds to an -0.01 dex kpc $^{-1}$ reduction in metallicity gradients using the MZGR derived above. To quantify the impact of different stellar masses on our observed redshift evolution, we normalize the gradients at each redshift bin to the same stellar masses based on the observed MZGR. In Fig. 6b, we compare the observed and mass-normalized metallicity gradients. We see that the peak of gradients at $z \approx 2$ is more notable and the trend of redshift evolution in Fig. 2 is still consistent.

To investigate the intrinsic scatter for galaxies with different stellar masses, we divide the sample galaxies into low-mass ($M_* < 10^9 M_\odot$) and high-mass ($M_* > 10^9 M_\odot$) bins. At redshift $1.5 < z \leq 3.5$, the intrinsic scatter for low-mass galaxies is found to be $\sigma_{\text{MZGR}} = 0.098 \pm 0.02$, while for massive galaxies, it is smaller, with $\sigma_{\text{MZGR}} = 0.023 \pm 0.002$. In contrast, at

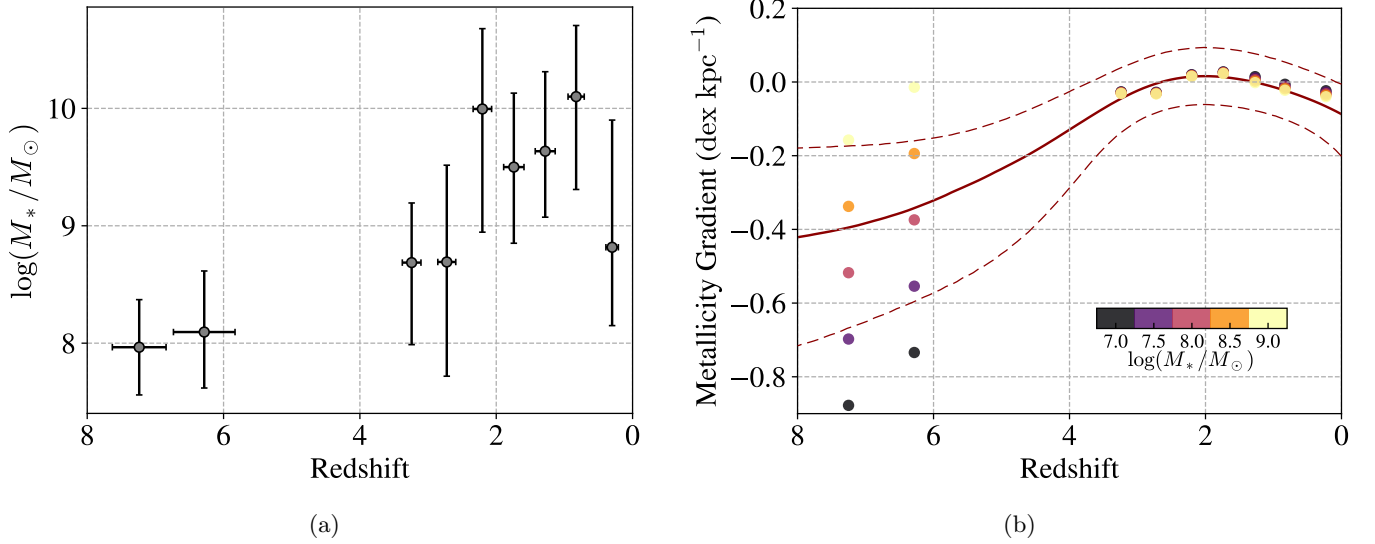


Figure 6. (a) The mass distribution of our full sample at each redshift bin. The circles represent the median of the stellar mass and the redshift. The errorbars represent 1σ intervals. (b) The redshift evolution of metallicity gradients with/without normalization by stellar masses. The red circles are the observed metallicity gradients, with the dark-red lines representing the best fitting, the same as Fig. 2. The circles represent metallicity gradients normalized to a fixed stellar mass, with colors indicating stellar masses normalized relative to the observed MZGR at each redshift.

lower redshifts ($0.01 < z \leq 1.5$), the scatter is reduced, with $\sigma_{\text{MZGR}} = 0.045 \pm 0.008$ for low-mass galaxies and $\sigma_{\text{MZGR}} = 0.037 \pm 0.002$ for massive galaxies. The increasing scattering of metallicity gradients towards the low-mass end was also found by X. Wang et al. (2020), who suggests more efficient feedback for low-mass galaxies, as shallower gravitational potentials are more susceptible to gas disruption (Y. Zhuang et al. 2019). In addition, the lowest mass galaxies have the highest sSFR (X. Wang et al. 2020), which could be triggered by either cold mode accretion (R. M. Woods et al. 2014), or merger-induced gas inflow (M. Martig & F. Bournaud 2008; J. P. Stott et al. 2013). The latter was found to be dominant in dwarf galaxies (X. Wang et al. 2020). The combined effects of metal production in merger-induced starbursts and gas dilution could lead to diverse chemical structures, reflected by large scatter in metallicity gradients at $z \sim 2$. The reduced scatters at $z < 1.5$ also suggests the impact of feedback on low-mass galaxies weakens at low-redshifts.

4.5. Toy models for metallicity gradients

To further understand how inflow and outflow take effect in our sample galaxies, we measure the gas fraction and metallicity in comparison with a simple analytical model (D. K. Erb 2008) (hereafter Erb08 model) and the Feedback-Free starburst (FFB) model (A. Dekel et al. 2023; Z. Li et al. 2024). The Erb08 model assumes that the surface density of star formation is proportional to the surface density of the gas (Kennicutt-Schmidt law)

and that the gas required by sustained star formation is regulated by inflows and outflows. This model has established basic guidelines for the relation between mass, metallicity, and gas fraction at $z \lesssim 3$ and such a “bath-tub” model is widely used to compare with observations (G. Cresci et al. 2010; K. Yabe et al. 2015; Y. Zhuang et al. 2019; X. Wang et al. 2019), although we acknowledge that it assumes no radial gas flows and constant star-formation efficiency (SFE). We consider two simple cases for the Erb08 model, one with pure inflow (with inflow rate defined as inflow gas mass per star formation $f_i = \dot{M}_{\text{in}}/\text{SFR}$) and the other with pure outflow (with outflow rate defined as outflow gas mass per star formation $f_o = \dot{M}_{\text{out}}/\text{SFR}$). The FFB scenario is proposed to characterize galaxies at $z \sim 10$ where the density of gas in star-forming clumps is above a threshold of $\sim 3 \times 10^3 \text{ cm}^{-3}$ with gas metallicity $\lesssim 0.2Z_{\odot}$, where Z_{\odot} is the solar metallicity. The FFB model predicts efficient star formation in thousands of globular-cluster-like clouds occurring on a free-fall timescale before the onset of effective stellar and supernova feedback. This allows multiple generations of starbursts, each with a high star-formation efficiency, separated by relatively quiescent periods. After each burst, SN feedback from massive stars will inevitably occur, yielding metals and enriching the galaxy. In Appendix J, we show that our galaxy sample satisfies the FFB criteria and is therefore suitable for applying this model.

We note that FFB is a simple analytical model aiming to illustrate the idea of efficient star formation

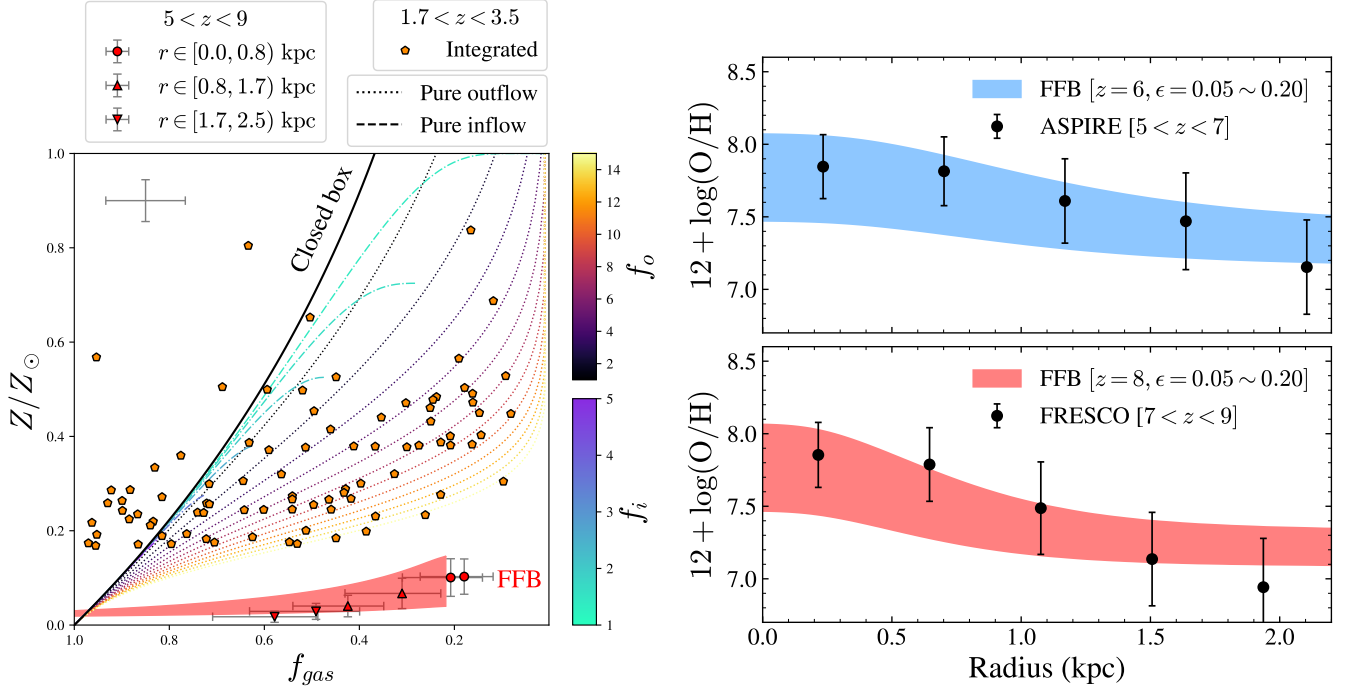


Figure 7. (a) The measured gas fraction and metallicity compared with the Erb08 model (D. K. Erb 2008) and the FFB model (A. Dekel et al. 2023; Z. Li et al. 2024). We consider Erb08 models with pure gas outflow ($f_i = 0$) and with pure inflow ($f_o = 0$). The curves for the Erb08 models are color-coded by inflow/outflow rate relative to SFR, with f_i denoting the inflow model (dash-dotted curves) and f_o denoting the outflow model (dotted curves). The solid black curve represents the closed-box model without outflow and inflow. The red shaded region shows the predictions of the FFB model (Z. Li et al. 2024) at redshift $z = 8$ with a star formation efficiency of $\epsilon = 0.05\text{--}0.20$ and a mass loading factor of 0.95, the maximum allowed value. The points in ASPIRE ($5 < z < 7$) and FRESCO ($7 < z < 9$) are estimated within different radial annuli (see Fig. 14), while the black points represent integrated measurements for the NGDEEP sample at $z = 1\text{--}3$. The gas fraction measurements of the ASPIRE and FRESCO galaxies include the uncertainty from unconstrained dust attenuation in estimating SFR maps. (b) The measured metallicity gradients at redshift $z = 5\text{--}7$ and $z = 7\text{--}9$ compared with the FFB model. The shaded regions represent the metallicity profiles predicted by the FFB model at redshifts 6 (blue) and 8 (red) with star formation efficiency $\epsilon = 0.2\text{--}0.5$, which is in line with our observations.

with inefficient metal mixing. We refer to more sophisticated models (e.g., J. Fu et al. 2013; M. Mollá et al. 2019; B. M. B. Henriques et al. 2020; P. Sharda et al. 2021a,b,c, 2024), which considers more physical processes such as metal diffusion, advection and more detailed feedback processes. M. A. Bellardini et al. (2021) demonstrated that neglecting diffusion leads to pronounced gradient steepening, whereas larger diffusion coefficients promote gradient flattening. Our simplified model thus illustrates the conditions under which metal mixing is inefficient in the absence of mechanisms such as diffusion.

Here, we consider a case of the steady-state solution for gas metallicity involving both high inflow rates and SFR, along with the resultant outflows in the FFB scheme (A. Dekel et al. 2023; Z. Li et al. 2024). In reality, the stars of FFB galaxies are expected to form in multiple generations of bursts rather than a continu-

ous process; therefore, this model should be considered a time-smoothed approximation. According to the conservation of gas mass among the ISM, gas inflow, SFR, and outflow (\dot{M}_{ISM} , \dot{M}_{in} , SFR, \dot{M}_{out}), and the conservation of the corresponding metal mass, we have

$$\dot{M}_{\text{ISM}} + \dot{M}_{\text{out}} = \dot{M}_{\text{in}} - (1 - f_{\text{sn}})\text{SFR} \quad (5)$$

$$Z_{\text{ISM}}\dot{M}_{\text{ISM}} + Z_{\text{out}}\dot{M}_{\text{out}} = Z_{\text{in}}\dot{M}_{\text{in}} - (Z_{\text{sf}} - Z_{\text{sn}}f_{\text{sn}})\text{SFR} \quad (6)$$

where f_{sn} and Z_{sn} are the mass fraction and metallicity of supernova ejecta respectively. The second equation assumes a steady state solution without metallicity evolution, i.e., $\dot{Z}_{\text{ISM}} = \dot{Z}_{\text{out}} = \dots = 0$. Below we estimate the metallicity and spherically averaged density profile, $\rho(r)$, of each component.

For a halo with an accretion rate of \dot{M}_{halo} , the gas accretion rate and SFR are $\dot{M}_{\text{in}} = f_b\dot{M}_{\text{halo}}$ and $\text{SFR} =$

$\epsilon \dot{M}_{\text{in}}$, respectively. In this equation, f_b is the cosmic baryonic fraction and ϵ is the star formation efficiency. The outflow rate is regulated by the mass loading factor, $\eta \equiv \dot{M}_{\text{out}}/\text{SFR}$. We introduce a parameter $f_{\text{out}} = \eta/\eta_{\text{max}} \leq 1$, where η_{max} is the maximum mass loading factor allowed for non-negative \dot{M}_{ism} , $\eta_{\text{max}} = \epsilon^{-1} - 1 + f_{\text{sn}}$. We then have $\dot{M}_{\text{out}} = f_{\text{out}}\eta_{\text{max}}\text{SFR}$ and $\dot{M}_{\text{ism}} = (1 - f_{\text{out}})\eta_{\text{max}}\text{SFR}$. We obtain the stellar mass and gas mass in ISM by integrating over time: $M_{\text{star}} = (1 - f_{\text{sn}})\epsilon f_b M_{\text{halo}}$ and $M_{\text{ism}} = (1 - f_{\text{out}})\eta_{\text{max}}\epsilon f_b M_{\text{halo}}$. Given the observed galaxy size R_e with a typical Sérsic index of $n_s = 1$, we estimate the density profile of stellar mass and ISM gas, $\rho_{\text{star}}(r)$ and $\rho_{\text{ism}}(r)$.

The model considers star formation occurring in the shock region with enhanced gas density at $R_{\text{shell}} \simeq 2R_e$, where the inflow encounters with the outflow (A. Dekel et al. 2023; Z. Li et al. 2024). We estimate the spherically averaged density of the inflow at radius r using mass flux $\dot{M}'_{\text{in}}(r)$ and inflow velocity $v_{\text{in}}(r) \sim v_{\text{vir}}$ (H. Aung et al. 2024): $\rho_{\text{in}}(r) = \dot{M}'_{\text{in}}(r)/4\pi r^2 v_{\text{in}}(r)$. For $r > R_{\text{shell}}$, we assume a constant inflow flux is $\dot{M}'_{\text{in}}(r) = \dot{M}_{\text{in}}$. Within R_{shell} , the flux decreases due to star formation and conversion to ISM, approximated by $\dot{M}'_{\text{in}}(r) = (\dot{M}_{\text{in}} - \text{SFR})(r^3/R_{\text{shell}}^3)$. After their birth, stars redistribute within the galaxy and launch outflows. We adopt the asymptotic solution for outflow density from R. A. Chevalier & A. W. Clegg (1985),

$$\rho_{\text{out}}(r) = \begin{cases} 0.3 \left(\frac{\dot{M}_{\text{out}}}{\dot{E}_{\text{sn}}} \right)^{1/2} \frac{\dot{M}_{\text{out}}}{R_{\text{shell}}^2} & \text{for } r < R_{\text{shell}}, \\ 0.05 \left(\frac{\dot{M}_{\text{out}}}{\dot{E}_{\text{sn}}} \right)^{1/2} \frac{\dot{M}_{\text{out}}}{r^2} & \text{for } r > R_{\text{shell}}, \end{cases} \quad (7)$$

where \dot{E}_{sn} is the SN energy returned by given SFR (Z. Li et al. 2024).

Assuming star formation from inflow gas without mixing (Z. Li et al. 2024), $Z_{\text{sf}} = Z_{\text{in}}$, and the outflow being launched from ISM, $Z_{\text{ism}} = Z_{\text{out}}$, we get

$$Z_{\text{ism}} = \frac{Z_{\text{in}}(1 - \epsilon) + Z_{\text{sn}}f_{\text{sn}}\epsilon}{(1 - \epsilon) + f_{\text{sn}}\epsilon}. \quad (8)$$

We then obtain the spherically averaged gas-phase metallicity profile as

$$Z(r) = \frac{Z_{\text{in}}\rho_{\text{in}}(r) + Z_{\text{ism}}[\rho_{\text{out}}(r) + \rho_{\text{ism}}(r)]}{\rho_{\text{in}}(r) + \rho_{\text{out}}(r) + \rho_{\text{ism}}(r)}, \quad (9)$$

and compute the projected metallicity and gas fraction profiles ($\Sigma_{\text{gas}}(r)/\Sigma_{\text{star+gas}}(r)$ where Σ represents the surface density) accordingly (Fig. 7). To mimic the observation, we compute the projected profiles for a galaxy sample with varying R_e . Our sample can be

approximated by a lognormal distribution with a scatter of $\sigma_{\ln R_e} = 0.5$ and a median value of $R_e = 0.53$ kpc for $z = 5 - 7$ and 0.36 kpc for $z = 7 - 9$.

We adopt $\epsilon = 0.05 \sim 0.2$, $Z_{\text{in}} = 0.01Z_{\odot}$, $Z_{\text{sn}} = 3Z_{\odot}$, $f_{\text{sn}} = 0.2$, and $f_{\text{out}} = 0.95$ (corresponding to $\eta = 18 \sim 4$), which reproduce the observation well. Eq. 8 gives $Z_{\text{ism}} = 0.04Z_{\odot}$ for $\epsilon = 0.05$ and $0.15Z_{\odot}$ for $\epsilon = 0.2$. The gas-phase metallicity is dominated by the enriched ISM in the central region and by the metal-poor inflows in the outskirts.

Different from Erb08, FFB model introduces radially dependent inflows and outflows. Assuming steady winds driven by supernovae in the FFB scheme, we consider a toy model for a steady solution of gas metallicity involving high inflow rates, SFR, and resultant outflows as a time-average approximation. At high-redshift, galaxies are fed by cold gas streams that penetrate deep into halos without significant mixing until joining the central galaxy (A. Dekel et al. 2009). These metal-poor cold inflows dominate the gas mass outside the galaxy, leading to low metallicity at large radii. This radially dependent gas flows are similar to accretion disk model proposed by E. Wang & S. J. Lilly (2022), and is consistent with inside-out growth scenario.

We then compare our observations with the predictions of different models. As shown in Fig. 7a, galaxies at cosmic noon can reasonably be predicted by the Erb08 models with a combination of inflow and outflow. While it requires high outflow rate to reach sufficiently low metallicity and low gas fraction. In contrast, the FFB model predicts lower metallicities ($Z < 0.1Z_{\odot}$) at low gas fractions, as expected by the high star formation efficiency and the dense cold inflows with inefficient mixing. From Fig. 7b, our observed metallicity gradients in the ASPIRE and FRESCO samples are also in agreement with the predictions of the FFB models at redshifts of $z = 6$ and $z = 8$, respectively. The inefficient gas mixing mechanism in the FFB scenario permits the existence of steep gradients at sufficiently high-redshift. This simple analytical model demonstrates that steep gradients can be maintained even in the presence of inflows and outflows, provided that central in situ star formation dominates the galaxy.

5. SUMMARY

We summarize the results from the synthesis of our new JWST observations and literature observations in Fig. 8. We find different phases in the redshift evolution of metallicity gradients, with a growing phase from sufficiently high-redshifts $z > 5$, which flattens at $z \approx 2$ and transitions to a descending phase until the present day. The implications of these three phases are as follow:

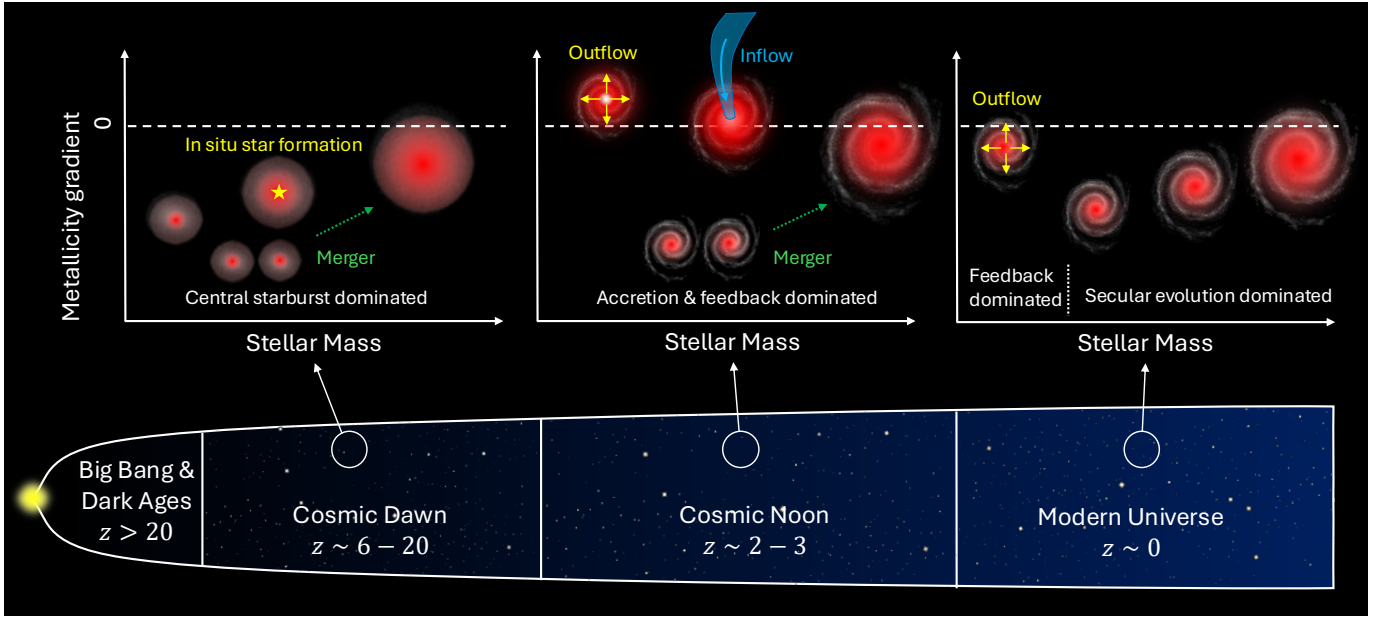


Figure 8. A sketch of how metallicity gradients are thought to evolve as galaxies grow across different cosmic epochs, based on our current knowledge. At cosmic dawn, the galaxies are observed with negative metallicity gradients, and they flatten with increasing stellar masses. This suggests metal mixing and transport process may be inefficient, and coincides with the inside-out growth scenario with in situ metal production. At cosmic noon, the galaxies are observed with nearly flat metallicity gradients, and they have anti-correlation with stellar masses. It suggests metal mixing and transport mechanisms including gas outflows, inflows and radial transport are efficient in redistributing metals in the ISM, which are sensitive with gravitational potentials. Mergers are also expected in dense high-redshift universe, which also contributes to gas mixing and flat gradients. In the local Universe, the MZGRs are observed to turn over at certain stellar masses, where higher-mass galaxies showing positive MZGRs while lower-mass galaxies showing the opposite trend. It suggests feedback-driven outflows may still be efficient for local dwarf galaxies, while the in situ metal production is dominating high-mass galaxies.

1. The ascending phase may indicate rapid growth in inside-out mode, supported by continuous replenishment from cold gas accretion. This stage reflects the early buildup of galaxies in a universe dominated by cold gas. The steep gradients align with inside-out growth and limited radial mixing. To explain this, we apply a toy model within the Feedback-Free Starburst scenario. In this framework, dense inflowing gas sustains efficient, localized star formation while the redistribution of metals is inefficient (A. Dekel et al. 2023; Z. Li et al. 2024). Such conditions preserve negative metallicity gradients, reflecting the early stages of galaxy assembly where internal chemical enrichment occurs earlier in the inner regions than in the outer disk. The observed positive correlation between metallicity gradient and stellar mass further supports the notion that massive galaxies grow more efficiently in an inside-out fashion during this period, linking their internal structure directly to their rapid mass accumulation history.
2. The metallicity gradients flatten over time toward $z \approx 2$, suggesting enhanced radial gas flows and

mixing mechanisms. This epoch corresponds to the peak of the SFRD, and is driven by a combination of intense cold gas accretion, elevated SFR, and strong stellar/SNe feedback (A. Dekel et al. 2009; T. M. Heckman & P. N. Best 2023; R. L. Sanders et al. 2023). The near-flat gradients observed at this time, along with large galaxy-to-galaxy scatter, reflect the turbulent internal dynamics triggered by gas accretion and feedback, which redistributes metals and flatten chemical abundances. The negative MZGR at this epoch signatures the dominant role of feedback in flattening gradients across stellar masses, especially in lower-mass systems (X. Ma et al. 2017).

3. The gradual decline in metallicity gradients observed at $z < 2$ coincides with the decrease in cold-mode accretion and a shift toward hot-mode accretion (F. van de Voort et al. 2011). This reduces the efficiency of star formation and limits pristine gas inflows, leading to slower chemical evolution. The reduced star formation activity and feedback at later times allows the galactic disks to stabilize and steepen the metallicity gradients. This

is reflected by the declining global SFRD and indicates the transition to a more gradual mode of galaxy growth driven by secular evolution. The positive MZGRs for massive galaxies also provide evidence. Although low-mass galaxies still show a negative MZGR (T. Li et al. 2025), feedback effects mainly impact young, low-mass systems in the local universe, whereas high-mass galaxies tend to be more evolved and dynamically stable with steeper metallicity gradients.

These findings highlight the intricate connection between galaxy internal star formation and the cosmic scale galaxy formation across cosmic time. The synchronized evolution pattern between metallicity gradients and cosmic star formation density reveals that gas accretion, star formation and feedback not only shape the evolutionary pathways of individual galaxies but also collectively drive the large-scale formation of the galaxy population in the universe. Nevertheless, how these various physical processes interact to drive the observed evolution remains inconclusive and calls for further extensive investigation with both observations and simulations.

ACKNOWLEDGMENTS

This work is based on observations made with the NASA/ESA/CSA James Webb Space Telescope, associated with the programs GO-2078, GO-1895, and GO-2079. The data were obtained from the Mikulski Archive for Space Telescopes at the Space Telescope Science Institute, which is operated by the Association of Universities for Research in Astronomy, Inc., under NASA contract NAS 5-03127 for JWST. The photometric catalog can be downloaded from the Dawn JWST Archive (DJA). The authors sincerely thank the FRESCO team (PI: Pascal Oesch) and the NGDEEP team (PI: Steven Finkelstein, Casey Papovich, and Nor Pirzkal) for developing their observing programs with a zero-exclusive-access period for the exquisite data. This work made use of the High-Performance Computing resources at Tsinghua University. This work uses images and photometry catalogs retrieved from the Dawn JWST Archive

(DJA). DJA is an initiative of the Cosmic Dawn Center, which is funded by the Danish National Research Foundation under grant No. 140.

We thank Steven Finkelstein and Raymond Simons for helpful discussions regarding NGDEEP data; Pascal Oesch and Romain Meyer for helpful discussions regarding FRESCO data. Z.H.L acknowledges Dandan Xu and Cheng Li for insightful discussions about the observational and theoretical context; Xiangcheng Ma, Guochao Sun, and Xunda Sun for valuable input about the FIRE simulations; Ayan Acharyya for helpful discussions on FOGGIE simulations and their theoretical interpretation; Alex Garcia for sharing results from EAGLE, Illustris, TNG and SIMBA simulations; Piyush Sharda for helpful discussions with metallicity gradient models; Prerak Grag for help with the photoionization model; Zechang Sun for maintaining High-Performance computers at Tsinghua University; Mengting Ju for sharing results from JWST MSA-3D.

Z.H.L., Z.C., X.L., and Y.W. are supported by the National Science Foundation of China (grant no. 12073014), the science research grants from the China Manned Space Project with No. CMS CSST-2021-A05, and the Tsinghua University Initiative Scientific Research Program (No. 20223080023). X. W. is supported by the China Manned Space Program with grant no. CMS-CSST-2025-A06, the National Natural Science Foundation of China (grant 12373009), the CAS Project for Young Scientists in Basic Research Grant No. YSBR-062, the Fundamental Research Funds for the Central Universities, the Xiaomi Young Talents Program. X. W. also acknowledges work carried out, in part, at the Swinburne University of Technology, sponsored by the ACAMAR visiting fellowship. Z.Z.L. acknowledges the European Union’s Horizon 2020 programme under the Marie Skłodowska-Curie grant No. 101109759 (“CuspCore”) and the Israel Science Foundation Grant ISF 861/20. SEIB is supported by the Deutsche Forschungsgemeinschaft (DFG) under Emmy Noether grant number BO 5771/1-1. F.W. acknowledges support from NSF grant AST-2308258. M.T. acknowledges support from the NWO grant 016.VIDI.189.162 (“ODIN”). S.ZOU acknowledges support from the National Natural Science Foundation of China (No.12303011).

REFERENCES

- | | |
|--|--|
| <p>Acharyya, A., Peeples, M. S., Tumlinson, J., et al. 2025, ApJ, 979, 129, doi: 10.3847/1538-4357/ad9dd8</p> | <p>Arribas, S., Perna, M., Rodríguez Del Pino, B., et al. 2024, A&A, 688, A146, doi: 10.1051/0004-6361/202348824</p> |
|--|--|

- Aung, H., Mandelker, N., Dekel, A., et al. 2024, MNRAS, 532, 2965, doi: [10.1093/mnras/stae1673](https://doi.org/10.1093/mnras/stae1673)
- Bagley, M. B., Pirzkal, N., Finkelstein, S. L., et al. 2024, ApJL, 965, L6, doi: [10.3847/2041-8213/ad2f31](https://doi.org/10.3847/2041-8213/ad2f31)
- Baker, W. M., Tacchella, S., Johnson, B. D., et al. 2024, Nature Astronomy, doi: [10.1038/s41550-024-02384-8](https://doi.org/10.1038/s41550-024-02384-8)
- Belfiore, F., Maiolino, R., Tremonti, C., et al. 2017, MNRAS, 469, 151, doi: [10.1093/mnras/stx789](https://doi.org/10.1093/mnras/stx789)
- Bellardini, M. A., Wetzel, A., Loebman, S. R., et al. 2021, MNRAS, 505, 4586, doi: [10.1093/mnras/stab1606](https://doi.org/10.1093/mnras/stab1606)
- Bian, F., Kewley, L. J., & Dopita, M. A. 2018, ApJ, 859, 175, doi: [10.3847/1538-4357/aabd74](https://doi.org/10.3847/1538-4357/aabd74)
- Bird, J. C., Loebman, S. R., Weinberg, D. H., et al. 2021, MNRAS, 503, 1815, doi: [10.1093/mnras/stab289](https://doi.org/10.1093/mnras/stab289)
- Birkin, J. E., Hutchison, T. A., Welch, B., et al. 2023, ApJ, 958, 64, doi: [10.3847/1538-4357/acf712](https://doi.org/10.3847/1538-4357/acf712)
- Birnboim, Y., & Dekel, A. 2003, MNRAS, 345, 349, doi: [10.1046/j.1365-8711.2003.06955.x](https://doi.org/10.1046/j.1365-8711.2003.06955.x)
- Boissier, S., & Prantzos, N. 2000, MNRAS, 312, 398, doi: [10.1046/j.1365-8711.2000.03133.x](https://doi.org/10.1046/j.1365-8711.2000.03133.x)
- Brammer, G., Strait, V., Matharu, J., & Momcheva, I. 2022,, 1.5.0, Zenodo Zenodo, doi: [10.5281/zenodo.6672538](https://doi.org/10.5281/zenodo.6672538)
- Bresolin, F. 2019, MNRAS, 488, 3826, doi: [10.1093/mnras/stz1947](https://doi.org/10.1093/mnras/stz1947)
- Cai, Z., Fan, X., Yang, Y., et al. 2017, ApJ, 837, 71, doi: [10.3847/1538-4357/aa5d14](https://doi.org/10.3847/1538-4357/aa5d14)
- Cappellari, M., & Copin, Y. 2003, MNRAS, 342, 345, doi: [10.1046/j.1365-8711.2003.06541.x](https://doi.org/10.1046/j.1365-8711.2003.06541.x)
- Carnall, A. C. 2017, arXiv e-prints, arXiv:1705.05165, doi: [10.48550/arXiv.1705.05165](https://doi.org/10.48550/arXiv.1705.05165)
- Carnall, A. C., McLure, R. J., Dunlop, J. S., et al. 2023, Nature, 619, 716, doi: [10.1038/s41586-023-06158-6](https://doi.org/10.1038/s41586-023-06158-6)
- Carniani, S., Arribas, S., Bunker, A., et al. 2021,, JWST Proposal. Cycle 1, ID. #1893
- Carton, D., Brinchmann, J., Wang, J., et al. 2015, MNRAS, 451, 210, doi: [10.1093/mnras/stv967](https://doi.org/10.1093/mnras/stv967)
- Carton, D., Brinchmann, J., Contini, T., et al. 2018, MNRAS, 478, 4293, doi: [10.1093/mnras/sty1343](https://doi.org/10.1093/mnras/sty1343)
- Chabrier, G. 2003, PASP, 115, 763, doi: [10.1086/376392](https://doi.org/10.1086/376392)
- Chakraborty, P., Sarkar, A., Smith, R., et al. 2025, ApJ, 985, 24, doi: [10.3847/1538-4357/adc7b5](https://doi.org/10.3847/1538-4357/adc7b5)
- Cheng, Y., Giallisco, M., Simons, R. C., et al. 2024, ApJ, 964, 94, doi: [10.3847/1538-4357/ad234a](https://doi.org/10.3847/1538-4357/ad234a)
- Chevalier, R. A., & Clegg, A. W. 1985, Nature, 317, 44, doi: [10.1038/317044a0](https://doi.org/10.1038/317044a0)
- Chevallard, J., & Charlot, S. 2016, MNRAS, 462, 1415, doi: [10.1093/mnras/stw1756](https://doi.org/10.1093/mnras/stw1756)
- Coil, A. L., Aird, J., Reddy, N., et al. 2015, ApJ, 801, 35, doi: [10.1088/0004-637X/801/1/35](https://doi.org/10.1088/0004-637X/801/1/35)
- Considère, S., Coziol, R., Contini, T., & Davoust, E. 2000, A&A, 356, 89, doi: [10.48550/arXiv.astro-ph/0001286](https://doi.org/10.48550/arXiv.astro-ph/0001286)
- Correa, C. A., Schaye, J., Wyithe, J. S. B., et al. 2018, MNRAS, 473, 538, doi: [10.1093/mnras/stx2332](https://doi.org/10.1093/mnras/stx2332)
- Crain, R. A., & van de Voort, F. 2023, ARA&A, 61, 473, doi: [10.1146/annurev-astro-041923-043618](https://doi.org/10.1146/annurev-astro-041923-043618)
- Cresci, G., Mannucci, F., Maiolino, R., et al. 2010, Nature, 467, 811, doi: [10.1038/nature09451](https://doi.org/10.1038/nature09451)
- Curti, M., Mannucci, F., Cresci, G., & Maiolino, R. 2020a, MNRAS, 491, 944, doi: [10.1093/mnras/stz2910](https://doi.org/10.1093/mnras/stz2910)
- Curti, M., Maiolino, R., Cirasuolo, M., et al. 2020b, MNRAS, 492, 821, doi: [10.1093/mnras/stz3379](https://doi.org/10.1093/mnras/stz3379)
- Curti, M., D'Eugenio, F., Carniani, S., et al. 2023, MNRAS, 518, 425, doi: [10.1093/mnras/stac2737](https://doi.org/10.1093/mnras/stac2737)
- Curti, M., Maiolino, R., Curtis-Lake, E., et al. 2024, A&A, 684, A75, doi: [10.1051/0004-6361/202346698](https://doi.org/10.1051/0004-6361/202346698)
- Davé, R., Anglés-Alcázar, D., Narayanan, D., et al. 2019, MNRAS, 486, 2827, doi: [10.1093/mnras/stz937](https://doi.org/10.1093/mnras/stz937)
- de los Reyes, M. A. C., Asali, Y., Wechsler, R., et al. 2024, arXiv e-prints, arXiv:2409.03959, doi: [10.48550/arXiv.2409.03959](https://doi.org/10.48550/arXiv.2409.03959)
- Dekel, A., & Birnboim, Y. 2006, MNRAS, 368, 2, doi: [10.1111/j.1365-2966.2006.10145.x](https://doi.org/10.1111/j.1365-2966.2006.10145.x)
- Dekel, A., Sarkar, K. C., Birnboim, Y., Mandelker, N., & Li, Z. 2023, MNRAS, 523, 3201, doi: [10.1093/mnras/stad1557](https://doi.org/10.1093/mnras/stad1557)
- Dekel, A., Birnboim, Y., Engel, G., et al. 2009, Nature, 457, 451, doi: [10.1038/nature07648](https://doi.org/10.1038/nature07648)
- Edmunds, M. G., & Pagel, B. E. J. 1984, MNRAS, 211, 507, doi: [10.1093/mnras/211.3.507](https://doi.org/10.1093/mnras/211.3.507)
- El-Badry, K., Wetzel, A., Geha, M., et al. 2016, ApJ, 820, 131, doi: [10.3847/0004-637X/820/2/131](https://doi.org/10.3847/0004-637X/820/2/131)
- Erb, D. K. 2008, ApJ, 674, 151, doi: [10.1086/524727](https://doi.org/10.1086/524727)
- Erb, D. K. 2015, Nature, 523, 169, doi: [10.1038/nature14454](https://doi.org/10.1038/nature14454)
- Evans, I. N. 1986, ApJ, 309, 544, doi: [10.1086/164623](https://doi.org/10.1086/164623)
- Faucher-Giguère, C.-A., Kereš, D., & Ma, C.-P. 2011, MNRAS, 417, 2982, doi: [10.1111/j.1365-2966.2011.19457.x](https://doi.org/10.1111/j.1365-2966.2011.19457.x)
- Ferrara, A., Vallini, L., Pallottini, A., et al. 2019, MNRAS, 489, 1, doi: [10.1093/mnras/stz2031](https://doi.org/10.1093/mnras/stz2031)
- Foreman-Mackey, D., Hogg, D. W., Lang, D., & Goodman, J. 2013, PASP, 125, 306, doi: [10.1086/670067](https://doi.org/10.1086/670067)
- Förster Schreiber, N. M., Genzel, R., Bouché, N., et al. 2009, ApJ, 706, 1364, doi: [10.1088/0004-637X/706/2/1364](https://doi.org/10.1088/0004-637X/706/2/1364)
- Förster Schreiber, N. M., Renzini, A., Mancini, C., et al. 2018, ApJS, 238, 21, doi: [10.3847/1538-4365/aadd49](https://doi.org/10.3847/1538-4365/aadd49)
- Franchetto, A., Mingozzi, M., Poggianti, B. M., et al. 2021, ApJ, 923, 28, doi: [10.3847/1538-4357/ac2510](https://doi.org/10.3847/1538-4357/ac2510)

- Frankel, N., Sanders, J., Rix, H.-W., Ting, Y.-S., & Ness, M. 2019, *ApJ*, 884, 99, doi: [10.3847/1538-4357/ab4254](https://doi.org/10.3847/1538-4357/ab4254)
- Fu, J., Kauffmann, G., Huang, M.-l., et al. 2013, *MNRAS*, 434, 1531, doi: [10.1093/mnras/stt1117](https://doi.org/10.1093/mnras/stt1117)
- Garcia, A. M., Torrey, P., Hemler, Z. S., et al. 2023, *MNRAS*, 519, 4716, doi: [10.1093/mnras/stac3749](https://doi.org/10.1093/mnras/stac3749)
- Garcia, A. M., Torrey, P., Bhagwat, A., et al. 2025, *arXiv e-prints*, arXiv:2503.03804, doi: [10.48550/arXiv.2503.03804](https://doi.org/10.48550/arXiv.2503.03804)
- Garg, P., Narayanan, D., Sanders, R. L., et al. 2024, *ApJ*, 972, 113, doi: [10.3847/1538-4357/ad5ae1](https://doi.org/10.3847/1538-4357/ad5ae1)
- Gibson, B. K., Pilkington, K., Brook, C. B., Stinson, G. S., & Bailin, J. 2013, *A&A*, 554, A47, doi: [10.1051/0004-6361/201321239](https://doi.org/10.1051/0004-6361/201321239)
- Gillman, S., Tiley, A. L., Swinbank, A. M., et al. 2021, *MNRAS*, 500, 4229, doi: [10.1093/mnras/staa3400](https://doi.org/10.1093/mnras/staa3400)
- Goddard, D., Thomas, D., Maraston, C., et al. 2017, *MNRAS*, 466, 4731, doi: [10.1093/mnras/stw3371](https://doi.org/10.1093/mnras/stw3371)
- Graf, R. L., Wetzel, A., Bailin, J., & Orr, M. E. 2024, *arXiv e-prints*, arXiv:2410.21377, doi: [10.48550/arXiv.2410.21377](https://doi.org/10.48550/arXiv.2410.21377)
- Grasha, K., Chen, Q. H., Battisti, A. J., et al. 2022, *ApJ*, 929, 118, doi: [10.3847/1538-4357/ac5ab2](https://doi.org/10.3847/1538-4357/ac5ab2)
- Harikane, Y., Zhang, Y., Nakajima, K., et al. 2023, *ApJ*, 959, 39, doi: [10.3847/1538-4357/ad029e](https://doi.org/10.3847/1538-4357/ad029e)
- Heckman, T. M., & Best, P. N. 2023, *Galaxies*, 11, 21, doi: [10.3390/galaxies11010021](https://doi.org/10.3390/galaxies11010021)
- Heintz, K. E., Brammer, G. B., Giménez-Arteaga, C., et al. 2023, *Nature Astronomy*, doi: [10.1038/s41550-023-02078-7](https://doi.org/10.1038/s41550-023-02078-7)
- Hemler, Z. S., Torrey, P., Qi, J., et al. 2021, *MNRAS*, 506, 3024, doi: [10.1093/mnras/stab1803](https://doi.org/10.1093/mnras/stab1803)
- Henriques, B. M. B., Yates, R. M., Fu, J., et al. 2020, *MNRAS*, 491, 5795, doi: [10.1093/mnras/stz3233](https://doi.org/10.1093/mnras/stz3233)
- Ho, I. T., Kudritzki, R.-P., Kewley, L. J., et al. 2015, *MNRAS*, 448, 2030, doi: [10.1093/mnras/stv067](https://doi.org/10.1093/mnras/stv067)
- Hopkins, P. F., Cox, T. J., Younger, J. D., & Hernquist, L. 2009, *ApJ*, 691, 1168, doi: [10.1088/0004-637X/691/2/1168](https://doi.org/10.1088/0004-637X/691/2/1168)
- Hopkins, P. F., Gurvich, A. B., Shen, X., et al. 2023, *MNRAS*, 525, 2241, doi: [10.1093/mnras/stad1902](https://doi.org/10.1093/mnras/stad1902)
- Isobe, Y., Ouchi, M., Suzuki, A., et al. 2022, *ApJ*, 925, 111, doi: [10.3847/1538-4357/ac3509](https://doi.org/10.3847/1538-4357/ac3509)
- Iwamoto, K., Brachwitz, F., Nomoto, K., et al. 1999, *ApJS*, 125, 439, doi: [10.1086/313278](https://doi.org/10.1086/313278)
- Izotov, Y. I., & Thuan, T. X. 2008, *ApJ*, 687, 133, doi: [10.1086/591660](https://doi.org/10.1086/591660)
- Izzard, R. G., Tout, C. A., Karakas, A. I., & Pols, O. R. 2004, *MNRAS*, 350, 407, doi: [10.1111/j.1365-2966.2004.07446.x](https://doi.org/10.1111/j.1365-2966.2004.07446.x)
- Jones, T., Ellis, R. S., Richard, J., & Jullo, E. 2013, *ApJ*, 765, 48, doi: [10.1088/0004-637X/765/1/48](https://doi.org/10.1088/0004-637X/765/1/48)
- Jones, T., Wang, X., Schmidt, K. B., et al. 2015, *AJ*, 149, 107, doi: [10.1088/0004-6256/149/3/107](https://doi.org/10.1088/0004-6256/149/3/107)
- Jones, T., Sanders, R., Chen, Y., et al. 2023, *ApJL*, 951, L17, doi: [10.3847/2041-8213/acd938](https://doi.org/10.3847/2041-8213/acd938)
- Ju, M., Wang, X., Jones, T., et al. 2025, *ApJL*, 978, L39, doi: [10.3847/2041-8213/ada150](https://doi.org/10.3847/2041-8213/ada150)
- Juneau, S., Bournaud, F., Charlot, S., et al. 2014, *ApJ*, 788, 88, doi: [10.1088/0004-637X/788/1/88](https://doi.org/10.1088/0004-637X/788/1/88)
- Kashiwagi, Y., Inoue, A. K., Isobe, Y., et al. 2021, *PASJ*, 73, 1631, doi: [10.1093/pasj/psab100](https://doi.org/10.1093/pasj/psab100)
- Kelly, B. C. 2007, *ApJ*, 665, 1489, doi: [10.1086/519947](https://doi.org/10.1086/519947)
- Kennicutt, Robert C., J. 1998, *ARA&A*, 36, 189, doi: [10.1146/annurev.astro.36.1.189](https://doi.org/10.1146/annurev.astro.36.1.189)
- Kennicutt, Jr., R. C. 1989, *ApJ*, 344, 685, doi: [10.1086/167834](https://doi.org/10.1086/167834)
- Kereš, D., Katz, N., Weinberg, D. H., & Davé, R. 2005, *MNRAS*, 363, 2, doi: [10.1111/j.1365-2966.2005.09451.x](https://doi.org/10.1111/j.1365-2966.2005.09451.x)
- Kereš, D., Katz, N., Fardal, M., Davé, R., & Weinberg, D. H. 2009, *Monthly Notices of the Royal Astronomical Society*, 395, 160, doi: [10.1111/j.1365-2966.2009.14541.x](https://doi.org/10.1111/j.1365-2966.2009.14541.x)
- Kewley, L. J., & Dopita, M. A. 2002, *ApJS*, 142, 35, doi: [10.1086/341326](https://doi.org/10.1086/341326)
- Khoram, A. H., & Belfiore, F. 2025, *A&A*, 693, A150, doi: [10.1051/0004-6361/202451980](https://doi.org/10.1051/0004-6361/202451980)
- Kojima, T., Ouchi, M., Rauch, M., et al. 2020, *ApJ*, 898, 142, doi: [10.3847/1538-4357/aba047](https://doi.org/10.3847/1538-4357/aba047)
- Kormendy, J., & Kennicutt, Robert C., J. 2004, *ARA&A*, 42, 603, doi: [10.1146/annurev.astro.42.053102.134024](https://doi.org/10.1146/annurev.astro.42.053102.134024)
- Lagos, P., Loubser, S. I., Scott, T. C., et al. 2022, *MNRAS*, 516, 5487, doi: [10.1093/mnras/stac2535](https://doi.org/10.1093/mnras/stac2535)
- Lang, M., Holley-Bockelmann, K., & Sinha, M. 2014, *ApJL*, 790, L33, doi: [10.1088/2041-8205/790/2/L33](https://doi.org/10.1088/2041-8205/790/2/L33)
- Langeroodi, D., & Hjorth, J. 2023, *arXiv e-prints*, arXiv:2307.06336, doi: [10.48550/arXiv.2307.06336](https://doi.org/10.48550/arXiv.2307.06336)
- Lara-López, M. A., Cepa, J., Bongiovanni, A., et al. 2010, *A&A*, 521, L53, doi: [10.1051/0004-6361/201014803](https://doi.org/10.1051/0004-6361/201014803)
- Larson, R. B. 1974, *MNRAS*, 166, 585, doi: [10.1093/mnras/166.3.585](https://doi.org/10.1093/mnras/166.3.585)
- Leethochawalit, N., Jones, T. A., Ellis, R. S., et al. 2016, *ApJ*, 820, 84, doi: [10.3847/0004-637X/820/2/84](https://doi.org/10.3847/0004-637X/820/2/84)
- Li, Q., Conselice, C. J., Adams, N., et al. 2024, *MNRAS*, 531, 617, doi: [10.1093/mnras/stae964](https://doi.org/10.1093/mnras/stae964)
- Li, T., Zhang, H.-X., Lyu, W., et al. 2025, *arXiv e-prints*, arXiv:2504.17541, doi: [10.48550/arXiv.2504.17541](https://doi.org/10.48550/arXiv.2504.17541)
- Li, Z., Dekel, A., Sarkar, K. C., et al. 2024, *A&A*, 690, A108, doi: [10.1051/0004-6361/202348727](https://doi.org/10.1051/0004-6361/202348727)
- Li, Z., Wang, X., Cai, Z., et al. 2022, *ApJL*, 929, L8, doi: [10.3847/2041-8213/ac626f](https://doi.org/10.3847/2041-8213/ac626f)

- Li, Z., Kakiichi, K., Christensen, L., et al. 2025, arXiv e-prints, arXiv:2504.18616, doi: [10.48550/arXiv.2504.18616](https://doi.org/10.48550/arXiv.2504.18616)
- Lian, J., Thomas, D., Maraston, C., et al. 2018, MNRAS, 476, 3883, doi: [10.1093/mnras/sty425](https://doi.org/10.1093/mnras/sty425)
- Lilly, S. J., Carollo, C. M., Pipino, A., Renzini, A., & Peng, Y. 2013, ApJ, 772, 119, doi: [10.1088/0004-637X/772/2/119](https://doi.org/10.1088/0004-637X/772/2/119)
- Lyu, C., Wang, E., Zhang, H., et al. 2025, ApJL, 981, L6, doi: [10.3847/2041-8213/adb4ed](https://doi.org/10.3847/2041-8213/adb4ed)
- Ma, X., Hopkins, P. F., Faucher-Giguère, C.-A., et al. 2016, MNRAS, 456, 2140, doi: [10.1093/mnras/stv2659](https://doi.org/10.1093/mnras/stv2659)
- Ma, X., Hopkins, P. F., Feldmann, R., et al. 2017, MNRAS, 466, 4780, doi: [10.1093/mnras/stx034](https://doi.org/10.1093/mnras/stx034)
- Madau, P., & Dickinson, M. 2014, ARA&A, 52, 415, doi: [10.1146/annurev-astro-081811-125615](https://doi.org/10.1146/annurev-astro-081811-125615)
- Magrini, L., Coccato, L., Stanghellini, L., Casasola, V., & Galli, D. 2016, A&A, 588, A91, doi: [10.1051/0004-6361/201527799](https://doi.org/10.1051/0004-6361/201527799)
- Magrini, L., Vilchez, J. M., Mampaso, A., Corradi, R. L. M., & Leisy, P. 2007, A&A, 470, 865, doi: [10.1051/0004-6361:20077445](https://doi.org/10.1051/0004-6361:20077445)
- Maiolino, R., Nagao, T., Grazian, A., et al. 2008, A&A, 488, 463, doi: [10.1051/0004-6361:200809678](https://doi.org/10.1051/0004-6361:200809678)
- Maiolino, R., Scholtz, J., Curtis-Lake, E., et al. 2023, arXiv e-prints, arXiv:2308.01230, doi: [10.48550/arXiv.2308.01230](https://doi.org/10.48550/arXiv.2308.01230)
- Maiolino, R., Risaliti, G., Signorini, M., et al. 2024, arXiv e-prints, arXiv:2405.00504, doi: [10.48550/arXiv.2405.00504](https://doi.org/10.48550/arXiv.2405.00504)
- Markov, V., Carniani, S., Vallini, L., et al. 2022, A&A, 663, A172, doi: [10.1051/0004-6361/202243336](https://doi.org/10.1051/0004-6361/202243336)
- Marszewski, A., Sun, G., Faucher-Giguère, C.-A., Hayward, C. C., & Feldmann, R. 2024, ApJL, 967, L41, doi: [10.3847/2041-8213/ad4cee](https://doi.org/10.3847/2041-8213/ad4cee)
- Martig, M., & Bournaud, F. 2008, MNRAS, 385, L38, doi: [10.1111/j.1745-3933.2008.00429.x](https://doi.org/10.1111/j.1745-3933.2008.00429.x)
- Matharu, J., & Brammer, G. 2022, 0.0 Zenodo, doi: [10.5281/zenodo.7447545](https://doi.org/10.5281/zenodo.7447545)
- Matharu, J., Muzzin, A., Sarrouh, G. T. E., et al. 2023, ApJL, 949, L11, doi: [10.3847/2041-8213/acd1db](https://doi.org/10.3847/2041-8213/acd1db)
- Matthee, J., Mackenzie, R., Simcoe, R. A., et al. 2023, ApJ, 950, 67, doi: [10.3847/1538-4357/acc846](https://doi.org/10.3847/1538-4357/acc846)
- McAlpine, S., Helly, J. C., Schaller, M., et al. 2016, Astronomy and Computing, 15, 72, doi: [10.1016/j.ascom.2016.02.004](https://doi.org/10.1016/j.ascom.2016.02.004)
- McDermid, R. M., Alatalo, K., Blitz, L., et al. 2015, MNRAS, 448, 3484, doi: [10.1093/mnras/stv105](https://doi.org/10.1093/mnras/stv105)
- Molina, J., Ibar, E., Swinbank, A. M., et al. 2017, MNRAS, 466, 892, doi: [10.1093/mnras/stw3120](https://doi.org/10.1093/mnras/stw3120)
- Mollá, M., Díaz, Á. I., Cavichia, O., et al. 2019, MNRAS, 482, 3071, doi: [10.1093/mnras/sty2877](https://doi.org/10.1093/mnras/sty2877)
- Møller, P., Fynbo, J. P. U., Ledoux, C., & Nilsson, K. K. 2013, MNRAS, 430, 2680, doi: [10.1093/mnras/stt067](https://doi.org/10.1093/mnras/stt067)
- Morishita, T., Stiavelli, M., Chary, R.-R., et al. 2024, ApJ, 963, 9, doi: [10.3847/1538-4357/ad1404](https://doi.org/10.3847/1538-4357/ad1404)
- Nagao, T., Maiolino, R., & Marconi, A. 2006, A&A, 459, 85, doi: [10.1051/0004-6361:20065216](https://doi.org/10.1051/0004-6361:20065216)
- Nakajima, K., Ouchi, M., Isobe, Y., et al. 2023, ApJS, 269, 33, doi: [10.3847/1538-4365/acd556](https://doi.org/10.3847/1538-4365/acd556)
- Nakajima, K., Ouchi, M., Xu, Y., et al. 2022, ApJS, 262, 3, doi: [10.3847/1538-4365/ac7710](https://doi.org/10.3847/1538-4365/ac7710)
- Nelson, D., Springel, V., Pillepich, A., et al. 2019, Computational Astrophysics and Cosmology, 6, 2, doi: [10.1186/s40668-019-0028-x](https://doi.org/10.1186/s40668-019-0028-x)
- Nelson, E. J., van Dokkum, P. G., Förster Schreiber, N. M., et al. 2016, ApJ, 828, 27, doi: [10.3847/0004-637X/828/1/27](https://doi.org/10.3847/0004-637X/828/1/27)
- Oesch, P. A., Brammer, G., Naidu, R. P., et al. 2023, MNRAS, 525, 2864, doi: [10.1093/mnras/stad2411](https://doi.org/10.1093/mnras/stad2411)
- Orr, M. E., Fielding, D. B., Hayward, C. C., & Burkhart, B. 2022, ApJ, 932, 88, doi: [10.3847/1538-4357/ac6c26](https://doi.org/10.3847/1538-4357/ac6c26)
- Pagel, B. E. J., & Edmunds, M. G. 1981, ARA&A, 19, 77, doi: [10.1146/annurev.aa.19.090181.000453](https://doi.org/10.1146/annurev.aa.19.090181.000453)
- Pallottini, A., Ferrara, A., Gallerani, S., et al. 2022, MNRAS, 513, 5621, doi: [10.1093/mnras/stac1281](https://doi.org/10.1093/mnras/stac1281)
- Pandya, V., Zhang, H., Huertas-Company, M., et al. 2024, ApJ, 963, 54, doi: [10.3847/1538-4357/ad1a13](https://doi.org/10.3847/1538-4357/ad1a13)
- Pérez, E., Cid Fernandes, R., González Delgado, R. M., et al. 2013, ApJL, 764, L1, doi: [10.1088/2041-8205/764/1/L1](https://doi.org/10.1088/2041-8205/764/1/L1)
- Pilkington, K., Few, C. G., Gibson, B. K., et al. 2012, A&A, 540, A56, doi: [10.1051/0004-6361/201117466](https://doi.org/10.1051/0004-6361/201117466)
- Poetrodjojo, H., Groves, B., Kewley, L. J., et al. 2018, MNRAS, 479, 5235, doi: [10.1093/mnras/sty1782](https://doi.org/10.1093/mnras/sty1782)
- Poetrodjojo, H., Groves, B., Kewley, L. J., et al. 2021, MNRAS, 502, 3357, doi: [10.1093/mnras/stab205](https://doi.org/10.1093/mnras/stab205)
- Queyrel, J., Contini, T., Kissler-Patig, M., et al. 2012, A&A, 539, A93, doi: [10.1051/0004-6361/201117718](https://doi.org/10.1051/0004-6361/201117718)
- Raiteri, C. M., Villata, M., & Navarro, J. F. 1996, A&A, 315, 105
- Reddy, N. A., Topping, M. W., Sanders, R. L., Shapley, A. E., & Brammer, G. 2023, ApJ, 952, 167, doi: [10.3847/1538-4357/acd754](https://doi.org/10.3847/1538-4357/acd754)
- Renaud, F., Ratcliffe, B., Minchev, I., et al. 2025, A&A, 694, A56, doi: [10.1051/0004-6361/202452219](https://doi.org/10.1051/0004-6361/202452219)
- Roca-Fàbrega, S., Kim, J.-H., Primack, J. R., et al. 2024, ApJ, 968, 125, doi: [10.3847/1538-4357/ad43de](https://doi.org/10.3847/1538-4357/ad43de)
- Rupke, D. S. N., Kewley, L. J., & Barnes, J. E. 2010a, ApJL, 710, L156, doi: [10.1088/2041-8205/710/2/L156](https://doi.org/10.1088/2041-8205/710/2/L156)

- Rupke, D. S. N., Kewley, L. J., & Chien, L. H. 2010b, *ApJ*, 723, 1255, doi: [10.1088/0004-637X/723/2/1255](https://doi.org/10.1088/0004-637X/723/2/1255)
- Sánchez-Menguiano, L., Sánchez, S. F., Pérez, I., et al. 2016, *A&A*, 587, A70, doi: [10.1051/0004-6361/201527450](https://doi.org/10.1051/0004-6361/201527450)
- Sánchez-Menguiano, L., Sánchez, S. F., Pérez, I., et al. 2018, *A&A*, 609, A119, doi: [10.1051/0004-6361/201731486](https://doi.org/10.1051/0004-6361/201731486)
- Sanders, R. L., Shapley, A. E., Topping, M. W., Reddy, N. A., & Brammer, G. B. 2024, *ApJ*, 962, 24, doi: [10.3847/1538-4357/ad15fc](https://doi.org/10.3847/1538-4357/ad15fc)
- Sanders, R. L., Shapley, A. E., Jones, T., et al. 2023, *ApJ*, 942, 24, doi: [10.3847/1538-4357/aca46f](https://doi.org/10.3847/1538-4357/aca46f)
- Sandles, L., D'Eugenio, F., Maiolino, R., et al. 2023, *arXiv e-prints*, arXiv:2306.03931, doi: [10.48550/arXiv.2306.03931](https://doi.org/10.48550/arXiv.2306.03931)
- Sarkar, A., Chakraborty, P., Vogelsberger, M., et al. 2024, *arXiv e-prints*, arXiv:2408.07974, doi: [10.48550/arXiv.2408.07974](https://doi.org/10.48550/arXiv.2408.07974)
- Schmidt, M. 1959, *ApJ*, 129, 243, doi: [10.1086/146614](https://doi.org/10.1086/146614)
- Scholte, D., Cullen, F., Carnall, A. C., et al. 2025, *MNRAS*, doi: [10.1093/mnras/staf834](https://doi.org/10.1093/mnras/staf834)
- Scholtz, J., Maiolino, R., D'Eugenio, F., et al. 2023, *arXiv e-prints*, arXiv:2311.18731, doi: [10.48550/arXiv.2311.18731](https://doi.org/10.48550/arXiv.2311.18731)
- Sharda, P., Ginzburg, O., Krumholz, M. R., et al. 2024, *MNRAS*, 528, 2232, doi: [10.1093/mnras/stae088](https://doi.org/10.1093/mnras/stae088)
- Sharda, P., Krumholz, M. R., Wisnioski, E., et al. 2021a, *MNRAS*, 504, 53, doi: [10.1093/mnras/stab868](https://doi.org/10.1093/mnras/stab868)
- Sharda, P., Krumholz, M. R., Wisnioski, E., et al. 2021b, *MNRAS*, 502, 5935, doi: [10.1093/mnras/stab252](https://doi.org/10.1093/mnras/stab252)
- Sharda, P., Wisnioski, E., Krumholz, M. R., & Federrath, C. 2021c, *MNRAS*, 506, 1295, doi: [10.1093/mnras/stab1836](https://doi.org/10.1093/mnras/stab1836)
- Shibuya, T., Ouchi, M., & Harikane, Y. 2015, *ApJS*, 219, 15, doi: [10.1088/0067-0049/219/2/15](https://doi.org/10.1088/0067-0049/219/2/15)
- Shields, G. A. 1990, *ARA&A*, 28, 525, doi: [10.1146/annurev.aa.28.090190.002521](https://doi.org/10.1146/annurev.aa.28.090190.002521)
- Shimizu, I., Todoroki, K., Yajima, H., & Nagamine, K. 2019, *MNRAS*, 484, 2632, doi: [10.1093/mnras/stz098](https://doi.org/10.1093/mnras/stz098)
- Shuntov, M., McCracken, H. J., Gavazzi, R., et al. 2022, *A&A*, 664, A61, doi: [10.1051/0004-6361/202243136](https://doi.org/10.1051/0004-6361/202243136)
- Simons, R. C., Kassin, S. A., Weiner, B. J., et al. 2017, *ApJ*, 843, 46, doi: [10.3847/1538-4357/aa740c](https://doi.org/10.3847/1538-4357/aa740c)
- Simons, R. C., Papovich, C., Momcheva, I., et al. 2021, *ApJ*, 923, 203, doi: [10.3847/1538-4357/ac28f4](https://doi.org/10.3847/1538-4357/ac28f4)
- Spolaor, M., Proctor, R. N., Forbes, D. A., & Couch, W. J. 2009, *ApJL*, 691, L138, doi: [10.1088/0004-637X/691/2/L138](https://doi.org/10.1088/0004-637X/691/2/L138)
- Springel, V., & Hernquist, L. 2003, *MNRAS*, 339, 289, doi: [10.1046/j.1365-8711.2003.06206.x](https://doi.org/10.1046/j.1365-8711.2003.06206.x)
- Stott, J. P., Sobral, D., Smail, I., et al. 2013, *MNRAS*, 430, 1158, doi: [10.1093/mnras/sts684](https://doi.org/10.1093/mnras/sts684)
- Strom, A. L., Steidel, C. C., Rudie, G. C., Trainor, R. F., & Pettini, M. 2018, *ApJ*, 868, 117, doi: [10.3847/1538-4357/aae1a5](https://doi.org/10.3847/1538-4357/aae1a5)
- Sun, F., Egami, E., Pirzkal, N., et al. 2023, *ApJ*, 953, 53, doi: [10.3847/1538-4357/acd53c](https://doi.org/10.3847/1538-4357/acd53c)
- Sun, X., Wang, X., Ma, X., et al. 2024, *arXiv e-prints*, arXiv:2409.09290, doi: [10.48550/arXiv.2409.09290](https://doi.org/10.48550/arXiv.2409.09290)
- Swinbank, A. M., Sobral, D., Smail, I., et al. 2012, *MNRAS*, 426, 935, doi: [10.1111/j.1365-2966.2012.21774.x](https://doi.org/10.1111/j.1365-2966.2012.21774.x)
- Tacchella, S., Johnson, B. D., Robertson, B. E., et al. 2023, *MNRAS*, 522, 6236, doi: [10.1093/mnras/stad1408](https://doi.org/10.1093/mnras/stad1408)
- Tang, M., Stark, D. P., Chen, Z., et al. 2023, *MNRAS*, 526, 1657, doi: [10.1093/mnras/stad2763](https://doi.org/10.1093/mnras/stad2763)
- Tapia-Contreras, B., Tissera, P. B., Sillero, E., et al. 2025, *arXiv e-prints*, arXiv:2502.02080, doi: [10.48550/arXiv.2502.02080](https://doi.org/10.48550/arXiv.2502.02080)
- Thielemann, F. K., Nomoto, K., & Yokoi, K. 1986, *A&A*, 158, 17
- Thorp, M. D., Ellison, S. L., Simard, L., Sánchez, S. F., & Antonio, B. 2019, *MNRAS*, 482, L55, doi: [10.1093/mnrasl/sly185](https://doi.org/10.1093/mnrasl/sly185)
- Tinsley, B. M. 1980, *Fundamentals of Cosmic Physics*, 5, 287, doi: [10.48550/arXiv.2203.02041](https://doi.org/10.48550/arXiv.2203.02041)
- Tissera, P. B., Machado, R. E. G., Sanchez-Blazquez, P., et al. 2016, *A&A*, 592, A93, doi: [10.1051/0004-6361/201628188](https://doi.org/10.1051/0004-6361/201628188)
- Tissera, P. B., Rosas-Guevara, Y., Bower, R. G., et al. 2019, *MNRAS*, 482, 2208, doi: [10.1093/mnras/sty2817](https://doi.org/10.1093/mnras/sty2817)
- Tissera, P. B., Rosas-Guevara, Y., Sillero, E., et al. 2022, *MNRAS*, 511, 1667, doi: [10.1093/mnras/stab3644](https://doi.org/10.1093/mnras/stab3644)
- Torrey, P., Cox, T. J., Kewley, L., & Hernquist, L. 2012, *ApJ*, 746, 108, doi: [10.1088/0004-637X/746/1/108](https://doi.org/10.1088/0004-637X/746/1/108)
- Trapp, C. W., Kereš, D., Chan, T. K., et al. 2022, *MNRAS*, 509, 4149, doi: [10.1093/mnras/stab3251](https://doi.org/10.1093/mnras/stab3251)
- Troncoso, P., Maiolino, R., Sommariva, V., et al. 2014, *A&A*, 563, A58, doi: [10.1051/0004-6361/201322099](https://doi.org/10.1051/0004-6361/201322099)
- Trump, J. R., Weiner, B. J., Scarlata, C., et al. 2011, *ApJ*, 743, 144, doi: [10.1088/0004-637X/743/2/144](https://doi.org/10.1088/0004-637X/743/2/144)
- Trump, J. R., Arrabal Haro, P., Simons, R. C., et al. 2023, *ApJ*, 945, 35, doi: [10.3847/1538-4357/acba8a](https://doi.org/10.3847/1538-4357/acba8a)
- Vallini, L., Ferrara, A., Pallottini, A., Carniani, S., & Gallerani, S. 2021, *MNRAS*, 505, 5543, doi: [10.1093/mnras/stab1674](https://doi.org/10.1093/mnras/stab1674)
- Vallini, L., Witstok, J., Sommovigo, L., et al. 2024, *MNRAS*, 527, 10, doi: [10.1093/mnras/stad3150](https://doi.org/10.1093/mnras/stad3150)
- van de Voort, F., & Schaye, J. 2012, *MNRAS*, 423, 2991, doi: [10.1111/j.1365-2966.2012.20949.x](https://doi.org/10.1111/j.1365-2966.2012.20949.x)

- van de Voort, F., Schaye, J., Booth, C. M., & Dalla Vecchia, C. 2011, MNRAS, 415, 2782, doi: [10.1111/j.1365-2966.2011.18896.x](https://doi.org/10.1111/j.1365-2966.2011.18896.x)
- van der Wel, A., Straughn, A. N., Rix, H. W., et al. 2011, ApJ, 742, 111, doi: [10.1088/0004-637X/742/2/111](https://doi.org/10.1088/0004-637X/742/2/111)
- van Zee, L., Salzer, J. J., Haynes, M. P., O'Donoghue, A. A., & Balonek, T. J. 1998, AJ, 116, 2805, doi: [10.1086/300647](https://doi.org/10.1086/300647)
- Venturi, G., Carniani, S., Parlanti, E., et al. 2024, A&A, 691, A19, doi: [10.1051/0004-6361/202449855](https://doi.org/10.1051/0004-6361/202449855)
- Vila-Costas, M. B., & Edmunds, M. G. 1992, MNRAS, 259, 121, doi: [10.1093/mnras/259.1.121](https://doi.org/10.1093/mnras/259.1.121)
- Vilchez, J. M., Pagel, B. E. J., Diaz, A. I., Terlevich, E., & Edmunds, M. G. 1988, MNRAS, 235, 633, doi: [10.1093/mnras/235.3.633](https://doi.org/10.1093/mnras/235.3.633)
- Wang, E., & Lilly, S. J. 2022, ApJ, 929, 95, doi: [10.3847/1538-4357/ac5e31](https://doi.org/10.3847/1538-4357/ac5e31)
- Wang, F., Yang, J., Hennawi, J. F., et al. 2023, ApJL, 951, L4, doi: [10.3847/2041-8213/accd6f](https://doi.org/10.3847/2041-8213/accd6f)
- Wang, X., Jones, T. A., Treu, T., et al. 2017, ApJ, 837, 89, doi: [10.3847/1538-4357/aa603c](https://doi.org/10.3847/1538-4357/aa603c)
- Wang, X., Jones, T. A., Treu, T., et al. 2019, ApJ, 882, 94, doi: [10.3847/1538-4357/ab3861](https://doi.org/10.3847/1538-4357/ab3861)
- Wang, X., Jones, T. A., Treu, T., et al. 2020, ApJ, 900, 183, doi: [10.3847/1538-4357/abacce](https://doi.org/10.3847/1538-4357/abacce)
- Wang, X., Jones, T., Vulcani, B., et al. 2022a, ApJL, 938, L16, doi: [10.3847/2041-8213/ac959e](https://doi.org/10.3847/2041-8213/ac959e)
- Wang, X., Li, Z., Cai, Z., et al. 2022b, ApJ, 926, 70, doi: [10.3847/1538-4357/ac3974](https://doi.org/10.3847/1538-4357/ac3974)
- Whitler, L., Stark, D. P., Endsley, R., et al. 2023, MNRAS, 519, 5859, doi: [10.1093/mnras/stad004](https://doi.org/10.1093/mnras/stad004)
- Woods, R. M., Wadsley, J., Couchman, H. M. P., Stinson, G., & Shen, S. 2014, MNRAS, 442, 732, doi: [10.1093/mnras/stu895](https://doi.org/10.1093/mnras/stu895)
- Woosley, S. E., & Weaver, T. A. 1995, ApJS, 101, 181, doi: [10.1086/192237](https://doi.org/10.1086/192237)
- Wuyts, E., Wisnioski, E., Fossati, M., et al. 2016, ApJ, 827, 74, doi: [10.3847/0004-637X/827/1/74](https://doi.org/10.3847/0004-637X/827/1/74)
- Yabe, K., Ohta, K., Akiyama, M., et al. 2015, ApJ, 798, 45, doi: [10.1088/0004-637X/798/1/45](https://doi.org/10.1088/0004-637X/798/1/45)
- Yang, J., Wang, F., Fan, X., et al. 2023, ApJL, 951, L5, doi: [10.3847/2041-8213/acc9c8](https://doi.org/10.3847/2041-8213/acc9c8)
- Yu, S., Bullock, J. S., Gurvich, A. B., et al. 2023, MNRAS, 523, 6220, doi: [10.1093/mnras/stad1806](https://doi.org/10.1093/mnras/stad1806)
- Zhang, S., Cai, Z., Xu, D., et al. 2023, Science, 380, 494, doi: [10.1126/science.abj9192](https://doi.org/10.1126/science.abj9192)
- Zhuang, Y., Leaman, R., van de Ven, G., et al. 2019, MNRAS, 483, 1862, doi: [10.1093/mnras/sty2916](https://doi.org/10.1093/mnras/sty2916)

APPENDIX

A. MEASURING METALLICITY GRADIENTS IN MASS BINS

The galaxies grow in different sizes and masses, which are correlated as mass-size relation (T. Shibuya et al. 2015; D. Langeroodi & J. Hjorth 2023). The metallicity gradients may be different for galaxies with different sizes. To investigate the impact of galaxy masses on the metallicity gradient, we divided the stacking into different mass bins at each redshift. For the ASPIRE sample, we utilized three mass bins: the most massive bin includes galaxies with $\log(M_*/M_\odot) > 9.00$, while the remaining lower-mass galaxies ($\log(M_*/M_\odot) < 9.00$) were evenly split into two bins: a low-mass bin ($7.18 < \log(M_*/M_\odot) < 8.09$) and a high-mass bin ($8.09 < \log(M_*/M_\odot) < 9.00$). The FRESCO sample are less massive, and we evenly divide them into low mass bin ($7.30 < \log(M_*/M_\odot) < 7.95$) and high mass bin ($7.95 < \log(M_*/M_\odot) < 8.70$). For comparison between individual and stacked measurements, we also separate the NGDEEP sample into low mass bin ($6.87 < \log(M_*/M_\odot) < 8.44$) and high mass bin ($8.44 < \log(M_*/M_\odot) < 9.81$). Within each mass bin, the stellar mass range spans approximately ~ 1 dex, corresponding to a change of $R_e \sim 0.1 - 0.2$ kpc as inferred from the mass-size relation (D. Langeroodi & J. Hjorth 2023). We applied the same median stacking method as used for galaxies in redshift bins. We applied the same R3 method (R. L. Sanders et al. 2024) to measure metallicity gradients for high mass bins and low mass bins in ASPIRE and FRESCO sample, shown in Fig. 9. However, since the bin with $\log(M_*/M_\odot) > 9.00$ is massive enough that MZR predicts these galaxies have higher metallicity which is out the lower branch range of R3 relation, we use upper branch instead to measure its metallicity gradient, shown in Fig. 10. For the NGDEEP sample, we use the same method with both R3 and R2 calibrations (F. Bian et al. 2018) to joint constrain metallicity as for individual galaxies, shown in Fig. 11. The stacks in mass bins provide a more representative characterization of the galaxy population with similar masses and sizes. From the stacked map of NGDEEP sample, we measure the MZGR slope of -0.019 dex kpc^{-1} using the two stacked points at low and high masses, which is consistent with the slope of -0.020 dex kpc^{-1} obtained from a linear regression on individual measurements (Section 4.3).

B. METALLICITY GRADIENTS IN UNITS OF EFFECTIVE RADIUS

As galaxies intrinsically have smaller sizes at higher redshift (T. Morishita et al. 2024), we expect steeper gradients for small galaxies if the changes in metallicity are the same. Galaxy size is also correlated to galaxy stellar mass, with massive galaxies having larger effective radii. Thus, the metallicity gradient measured with respect to effective radius R_e should provide a quantity that is less dependent on stellar mass and size.

We use a sérsic model convolved with PSF to fit galaxy morphology with GALFIT. With fitted R_e , we resample the emission maps to the pixel scale of $0.25 R_e$ with flux conservation. Then we stack the galaxy emission maps using the median stacking method, before measuring the gradients on the stacks. In Fig. 12, we show the stacked results from the ASPIRE and FRESCO samples. We still observe steep negative gradients in units of dex R_e^{-1} . This test eliminates possible bias from the variation of galaxy sizes.

The effective radii for the NGDEEP sample are measured on the F115W image. The metallicity gradients rescaled by R_e are shown in Fig. 13. We also include literature observations at high-redshift (D. Carton et al. 2018; R. C. Simons et al. 2021), and local observations from MaNGA (A. Franchetto et al. 2021), which provide metallicity gradients in the same units for comparison. The ascending phase at $3.5 < z < 1.75$ remains in the NGDEEP galaxies. The gradients at $z > 5$ are still more steep than galaxy populations at lower redshift despite their intrinsic smaller sizes. The redshift evolution of metallicity gradients measured with R_e is consistent with that measured with kpc.

C. GAS FRACTION ESTIMATION

The gas fraction is useful information when comparing our observations with analytical models shown in Fig. 4. In this subsection, we present our gas fraction estimate as follows. We estimate gas density by inverting the Kennicutt–Schmidt law (KS law, M. Schmidt 1959; R. C. Kennicutt 1989):

$$\Sigma_{\text{SFR}} = 10^{-12} \kappa_s \Sigma_{\text{gas}}^{1.4}, \quad (\text{C1})$$

where Σ_{SFR} is in $M_\odot \text{yr}^{-1} \text{kpc}^{-2}$, and Σ_{gas} is in $M_\odot \text{kpc}^{-2}$. κ_s is the burstiness parameter representing the deviation from the original KS relation (A. Ferrara et al. 2019). There is evidence that the KS relation is not universally

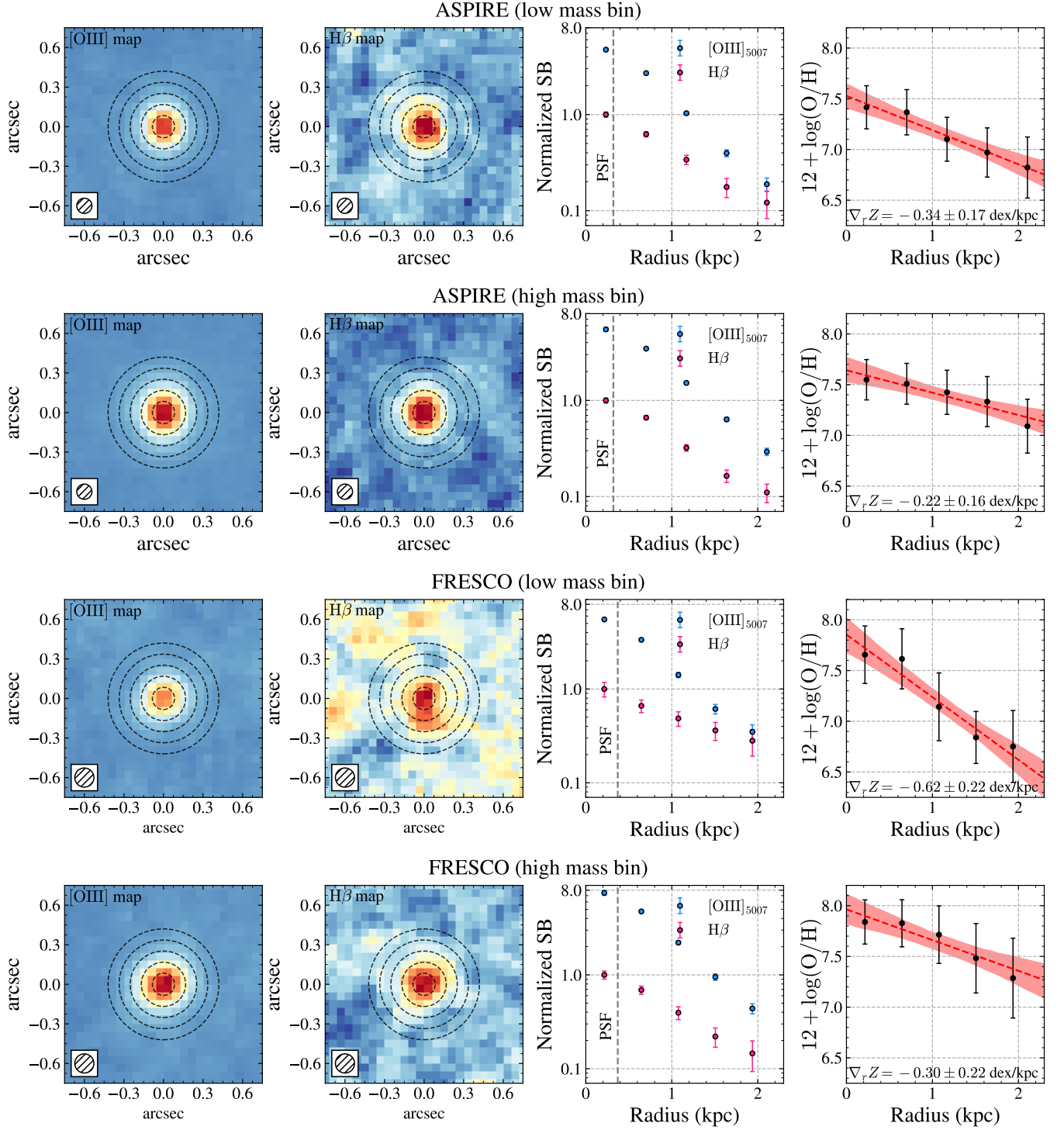


Figure 9. Stacking results in different mass bins. First two rows: results from ASPIRE galaxies in low-mass bin ($7.18 < \log(M_*/M_\odot) < 8.09$) and high mass bin ($8.09 < \log(M_*/M_\odot) < 9.00$). Last two rows: results from FRESCO galaxies in low-mass bin ($7.30 < \log(M_*/M_\odot) < 7.95$) and high mass bin ($7.95 < \log(M_*/M_\odot) < 8.70$).

applicable and may undergo an upward shift at higher redshifts (A. Pallottini et al. 2022; V. Markov et al. 2022). The highly star-forming galaxies are expected to have $\kappa_s > 1$. Thus, we adopt $\kappa_s = 10$ for the galaxy sample at $z \approx 1-3$, and a higher value of $\kappa_s = 20$ for galaxies at $z \approx 6-7$, due to burstier star formation suggested by recent measurements

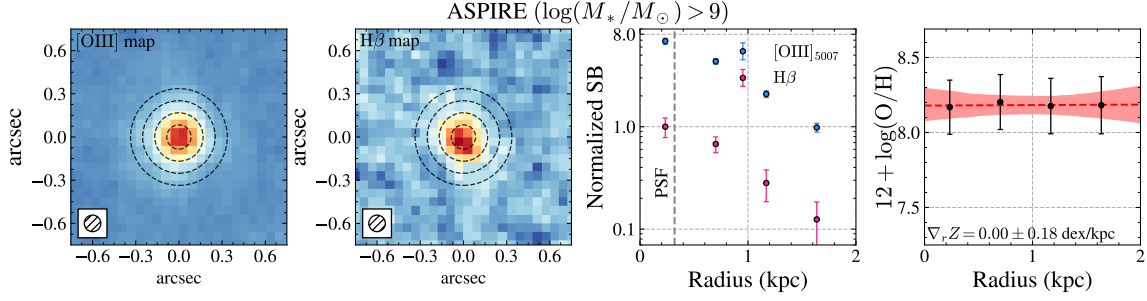


Figure 10. The same as Fig. 9, but for galaxies with highest stellar masses ($\log(M_*/M_\odot) > 9.00$) in ASPIRE sample. The metallicities are estimated using the upper branch solution of R3 relation in [R. L. Sanders et al. \(2024\)](#).

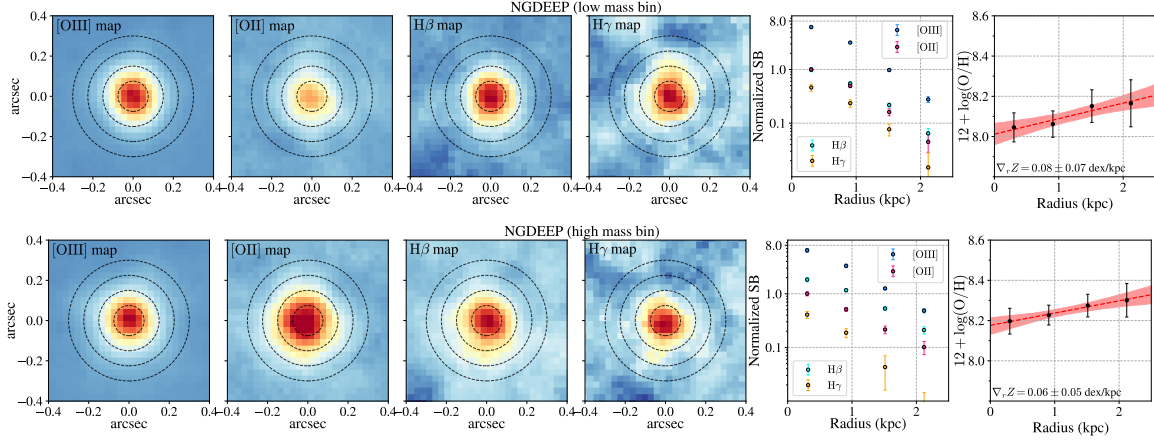


Figure 11. Stacking results from NGDEEP galaxies in low-mass bin ($6.87 < \log(M_*/M_\odot) < 8.44$) and high mass bin ($8.44 < \log(M_*/M_\odot) < 9.81$).

([V. Markov et al. 2022](#); [L. Vallini et al. 2021, 2024](#)). Since κ_s for individual galaxies is vastly unconstrained, we add 50% uncertainty to the values we adopted to have a conservative estimation of the gas fraction.

We adopt the Balmer ratio $H\alpha/H\beta = 2.86$ in Case B recombination, where we estimate the SFR by using $H\beta$ luminosity and the following calibration ([J. Kennicutt 1998](#)):

$$\text{SFR} = 13.16 \times 10^{-42} \frac{L_{H\beta}}{\text{erg s}^{-1}} (M_\odot \text{ yr}^{-1}). \quad (\text{C2})$$

Since we cannot derive spatially resolved dust attenuation without other Balmer series, we cannot directly correct the $H\beta$ flux for dust. Recent studies of galaxies within a similar mass range at $z > 5$ have been found with a certain amount of dust, either through SED modeling ([J. Matthee et al. 2023](#); [S. Tacchella et al. 2023](#)), or Balmer decrement ([L. Sandles et al. 2023](#)). The typical dust is expected to be $E(B-V) \sim 0.1$ corresponding to the uncertainty 35% for the SFR derived from the uncorrected flux $H\beta$. Since this uncertainty is not negligible, we add one-side 35% uncertainty to SFR maps. While for the NGDEEP sample, the $H\beta$ fluxes have been corrected by dust using the Balmer decrement between $H\alpha$, $H\beta$, and $H\gamma$ (equation 1).

The Σ_{star} is obtained by spatially resolved SED fitting to each pixel. We match the F115W and F200W with the PSF to the F356W band in the ASPIRE sample, and we match all the photometric bands with the PSF to F444W in the FRESCO sample. After the PSF matching, both the images and emission maps have the same PSF. We use a median stack for all cutouts in units of luminosity and convert back to flux density using the median redshifts $z = 6.28$ and $z = 7.24$ for ASPIRE and FRESCO respectively. We then apply the SED fitting to each pixel assuming the fixed redshift $z = 6.28$ and $z = 7.24$ for ASPIRE and FRESCO, respectively.

The gas surface density Σ_{gas} can be derived by the inverse KS law in Eq. C1. The gas fraction is then expressed as:

$$f_{\text{gas}} = \Sigma_{\text{gas}} / (\Sigma_{\text{gas}} + \Sigma_{\text{star}}). \quad (\text{C3})$$

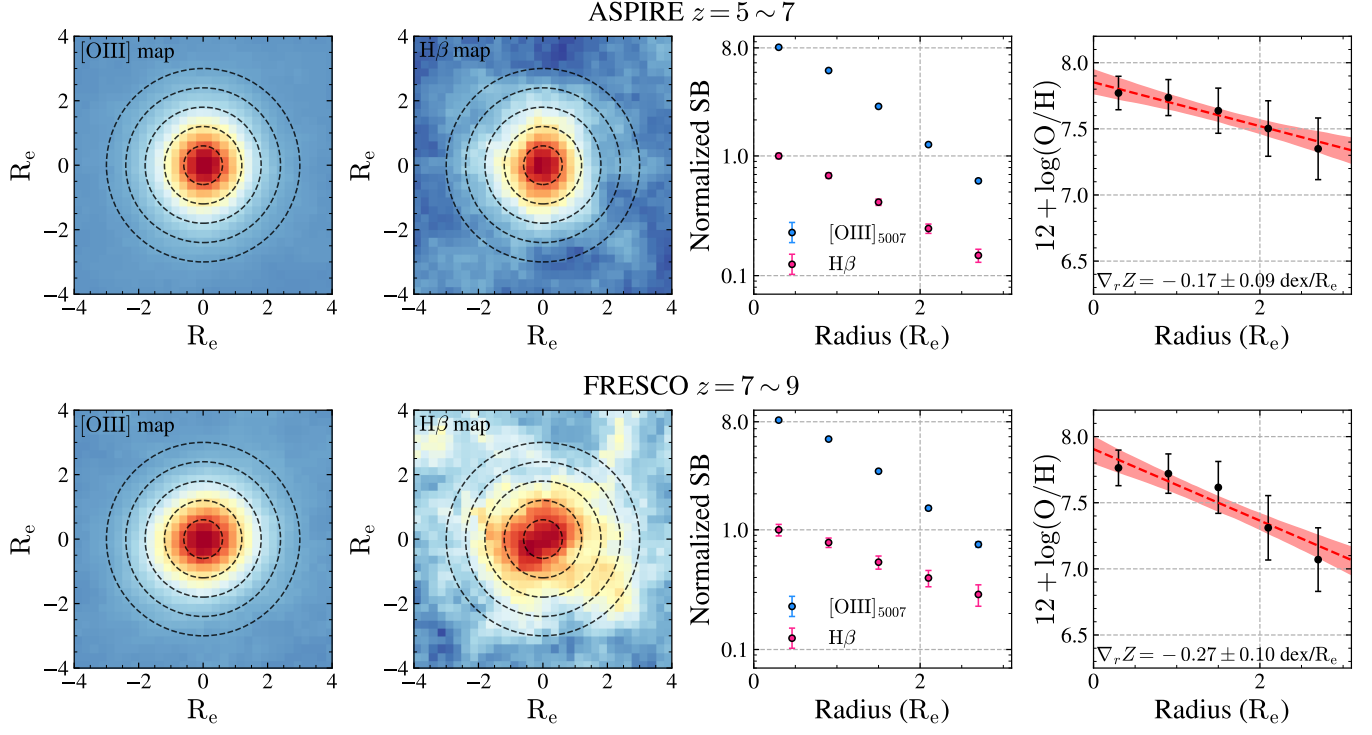


Figure 12. Stacking results in scale of effective radius (R_e).

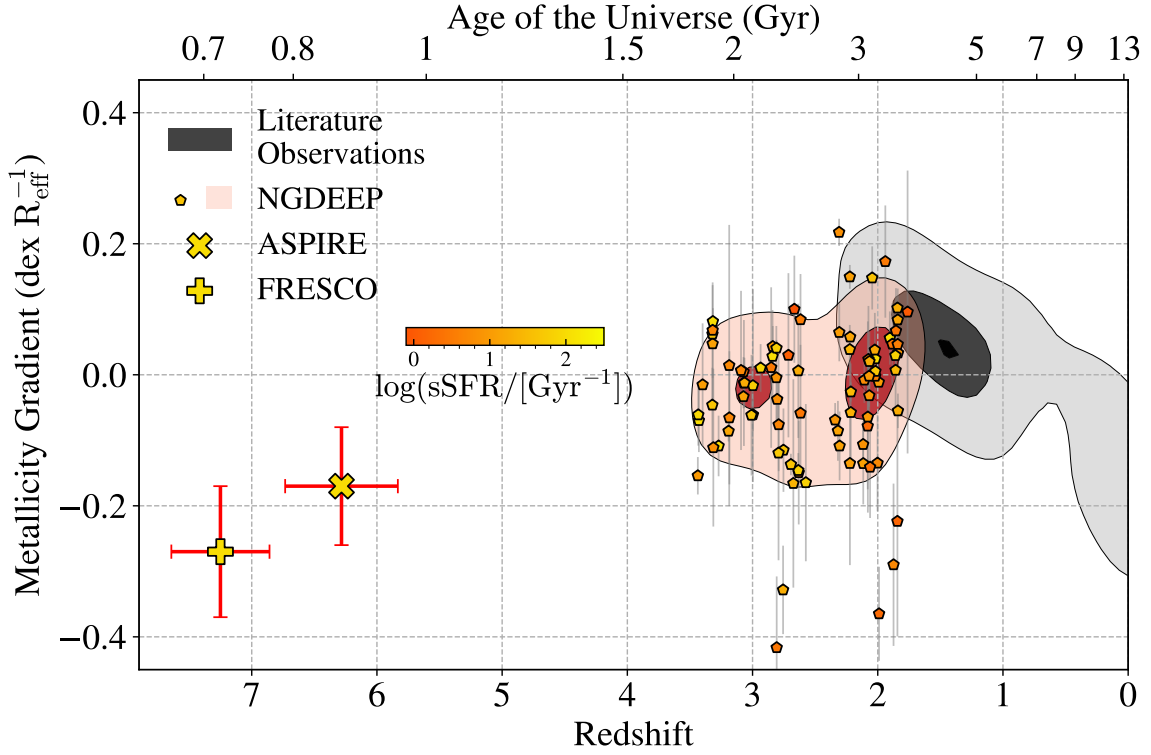


Figure 13. Metallicity gradients measured with respect to R_{eff} . The symbols are the same as in Fig. 2. The gray shadow encompasses literature observations (D. Carton et al. 2018; A. Franchetto et al. 2021; R. C. Simons et al. 2021).

The stellar mass surface density map, the SFR surface density map, and the derived gas fraction map are shown in Fig. 14. The gas fraction we derived here has been used in Fig. 7a.

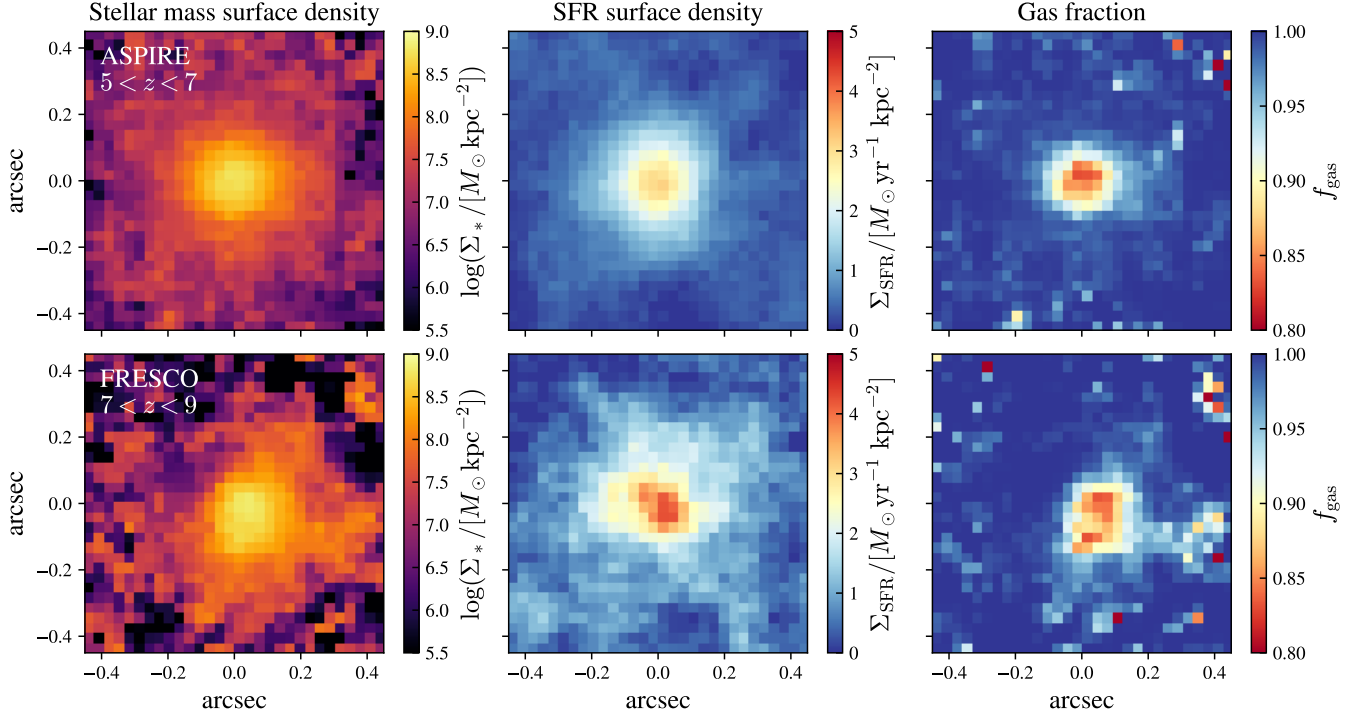


Figure 14. From left to right: stellar mass surface density, SFR surface density and gas fraction of ASPIRE (upper) and FRESCO (lower) samples.

D. FIT REDSHIFT EVOLUTION OF METALLICITY GRADIENTS

We perform MCMC sampling of the multidimensional parameter space with the package EMCEE (D. Foreman-Mackey et al. 2013) to fit the double-power-law model of Eq (3). We apply a flat prior for the following parameters: $\gamma_0 \sim \mathcal{U}(-10, 10)$, $\gamma_1 \sim \mathcal{U}(-1, 1)$, $\gamma_2 \sim \mathcal{U}(0, 10)$, $\gamma_3 \sim \mathcal{U}(-10, 10)$, and $\gamma_4 \sim \mathcal{U}(-10, 10)$. The sampling is performed with 32 walkers, 5000 iterations each, and with a burn-in period $n = 1000$. The posterior probability distribution for the parameters is shown in Fig. 15. The median model and 1σ prediction interval are shown in Fig. 2 and Fig. 3.

E. SYSTEMATICS USING DIFFERENT EMISSION-LINE CALIBRATIONS

To verify that our results are not significantly altered by different metallicity diagnostics, we compare our fiducial measurements using F. Bian et al. (2018) in the NGDEEP sample with other popular calibrations based on different samples and methods (R. Maiolino et al. 2008; M. Curti et al. 2020a; K. Nakajima et al. 2022). The calibrations in R. Maiolino et al. (2008) combine the direct electron temperature measurements from the Sloan Digital Sky Survey (SDSS) in the low-metallicity branch (T. Nagao et al. 2006) and the predictions of a photoionization model in the high-metallicity branch (L. J. Kewley & M. A. Dopita 2002). The calibrations in M. Curti et al. (2020a) are derived from a set of individual low-metallicity galaxies together with stacks of high-metallicity galaxies in the redshift range $0.027 < z < 0.25$, where auroral lines are detected in composite spectra, where the metallicities are self-consistently measured via the T_e method for both the high and low metallicity range. The calibrations in K. Nakajima et al. (2022) are derived from more metal-poor galaxies with auroral lines detected and selected from HSC-SSP and SDSS catalog and follow-up observations (T. Kojima et al. 2020; Y. Isobe et al. 2022), in addition to high metallicity galaxies used in M. Curti et al. (2020a).

Following the same procedures, we derive the metallicity maps, measure the metallicity gradients for each galaxy and the stacks, and compare those with the fiducial measurements. The comparisons are shown in Fig. 16. We find no significant bias using either of the three alternative calibrations, with all of the scatters around equality being within

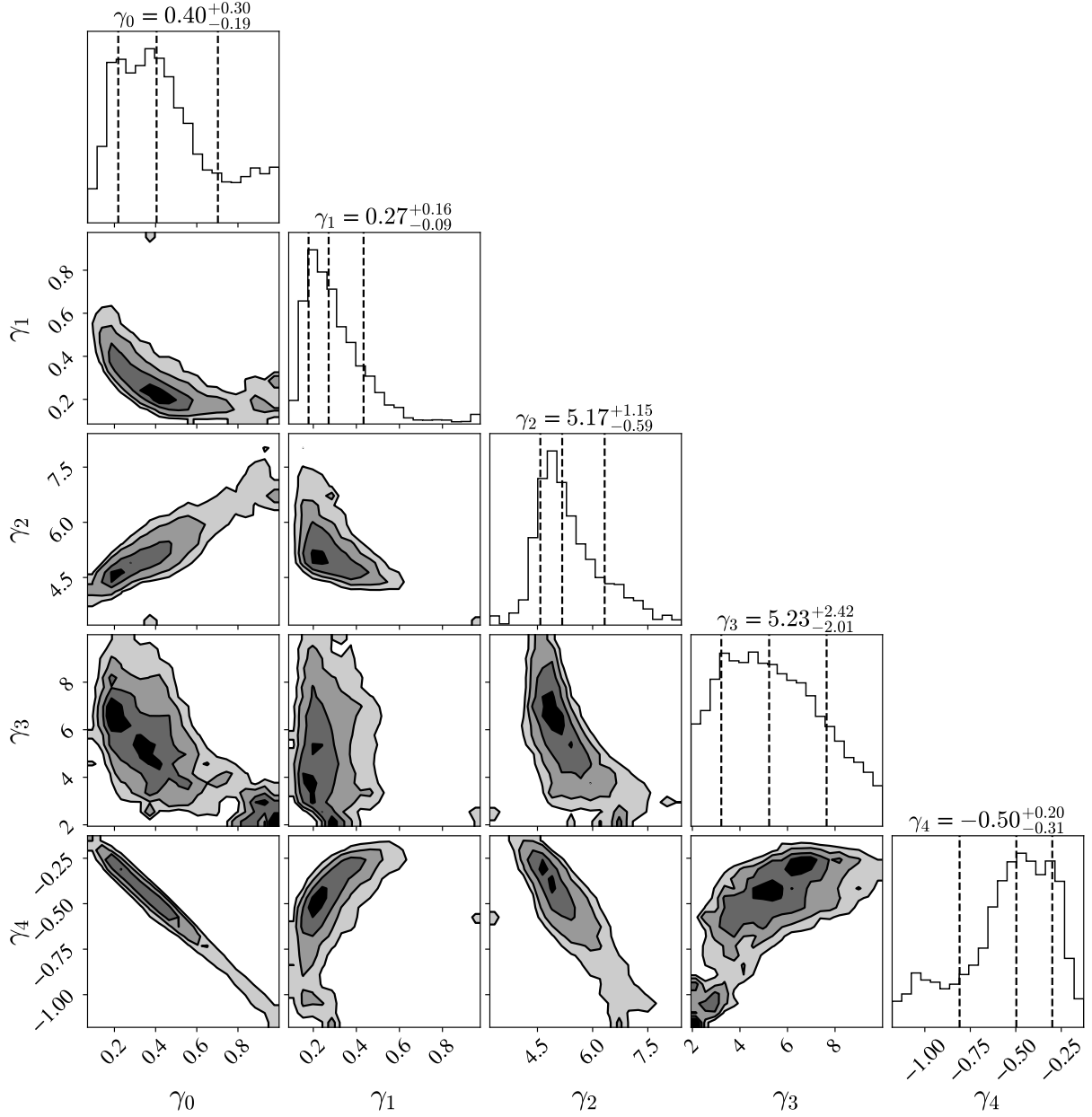


Figure 15. Posterior distribution of γ_0 , γ_1 , γ_2 , γ_3 , and γ_4 in Equation 3 from MCMC sampling. The values on the top of each column are the medians with 1σ interval.

1σ measurement uncertainties $\lesssim 0.1 \text{ dex kpc}^{-1}$. The different calibrations for two $z > 5$ stacks also introduces small uncertainties $\lesssim 0.1 \text{ dex kpc}^{-1}$. Thus, the choice of metallicity calibrations does not alter our results of the evolution of the metallicity gradient.

F. INTEGRATED METALLICITY OF $Z > 5$ SAMPLE

Here we measure the integrated metallicity of our stacks in Fig. 1. We resample our 1D spectra to rest-frame on a common 1 \AA wavelength grid with flux preserved using `spectres` (A. C. Carnall 2017). Following X. Wang et al. (2022b), to avoid the excessive weighting towards bright sources with stronger line fluxes, we normalized each spectra by their measured $[\text{O III}]$ flux. We take the median value of the normalized spectra at each wavelength grid and the uncertainty is estimated by measuring the standard deviation from 1000 bootstrap realizations of the sample. The median stacked 1D rest-frame spectra of ASPIRE and FRESCO are shown in Fig. 17. We fit $[\text{O III}]$ and $\text{H}\beta$ line

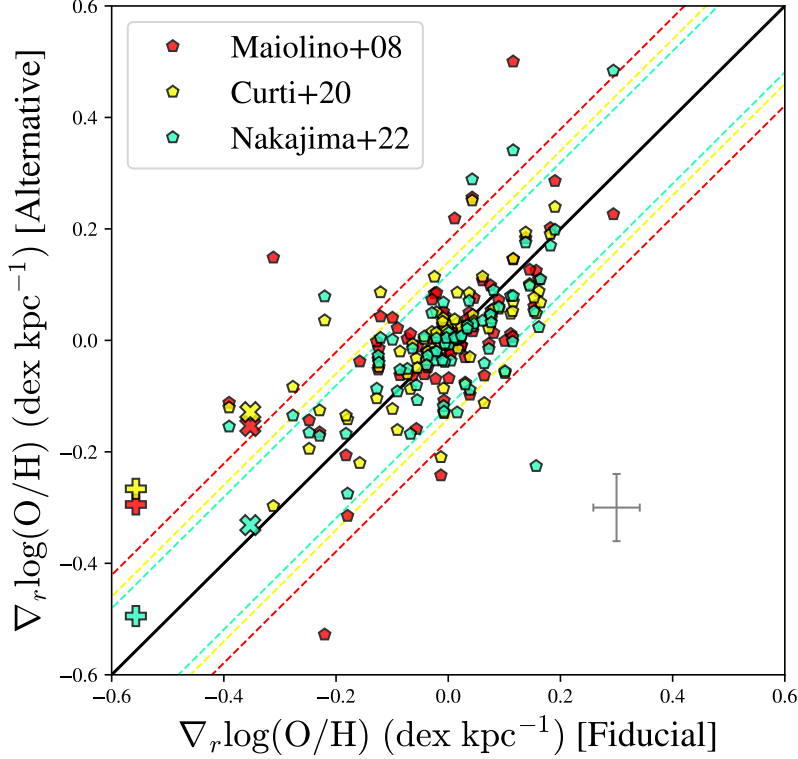


Figure 16. Comparisons between different strong-line calibrations for metallicity gradients. NGDEEP, ASPIRE and FRESCO measurements are marked with pentagons, “x” and “+” respectively. The x-axis is the fiducial measurements with [F. Bian et al. \(2018\)](#) for NGDEEP galaxies and [R. L. Sanders et al. \(2024\)](#) for ASPIRE and FRESCO galaxies, and the y-axis is the measurements using alternative calibrations ([R. Maiolino et al. 2008](#); [M. Curti et al. 2020a](#); [K. Nakajima et al. 2022](#)). The diagonal black line shows equality and the dashed lines show the standard deviation around equality for each calibration in the corresponding color.

fluxes using Gaussian profiles. We do not set line-ratio constraints between $[\text{O III}]_{5007}$ and $[\text{O III}]_{4959}$. Assuming the lower branch solution, the metallicities are measured using R3 calibrations from [R. L. Sanders et al. \(2024\)](#), the same as we use for metallicity gradient measurements. We also compare the metallicities from different calibrations in [K. Nakajima et al. \(2022\)](#). We list the integrated line fluxes and metallicities in Table 3. We note that [K. Nakajima et al. \(2022\)](#) calibration gives $\sim 0.1 - 0.2$ dex high metallicities. More detailed analysis of integrated metallicity and mass-metallicity relation of the ASPIRE and NGDEEP sample is presented in [Z. Li et al. \(2025\)](#) and X. He et al. submitted.

G. UNCERTAINTIES IN GRADIENT MEASUREMENTS

To quantify how uncertainties in emission may impact our measurements in the NGDEEP sample, we do a mock test in the same manner as in [Z. Li et al. \(2022\)](#). We fit a normal model to the distribution of effective radius R_e , and log-normal models to axis ratio b/a , and $\text{SNR}_{[\text{O III}]}$ in the NGDEEP sample and randomly generate mock galaxies with 2D Sérsic surface brightness profiles given the distribution of R_e , b/a and $\text{SNR}_{[\text{O III}]}$. We apply a flat gradient to all mock galaxies and use the same method discussed before to reconstruct the metallicity gradients. We measure the scatter of 200 mock galaxies and find the intrinsic scatter in the measurement to be ≈ 0.09 dex kpc^{-1} .

Since we used the stacking method for galaxies at $z > 5$ in ASPIRE and FRESCO, we also used the mock data set to test whether it reflects the median metallicity gradients by stacking emission maps. We start by randomly generating 300 galaxies with stellar masses following a log-norm distribution, which is fitted on our SED results. We then assign the effective radius and metallicity of each mock galaxy using the mass-size relation ([D. Langeroodi & J. Hjorth 2023](#)) and the mass-metallicity relation ([A. Sarkar et al. 2024](#)) measured at similar redshifts. We also considered the intrinsic scatter of these relations, so we added Gaussian noise to R_e and $12 + \log(\text{O}/\text{H})$, with $\sigma_{\log(R_e/\text{kpc})} = 0.25$ and $\sigma_{12+\log(\text{O}/\text{H})} = 0.16$ ([D. Langeroodi & J. Hjorth 2023](#); [A. Sarkar et al. 2024](#)). We fit a normal distribution

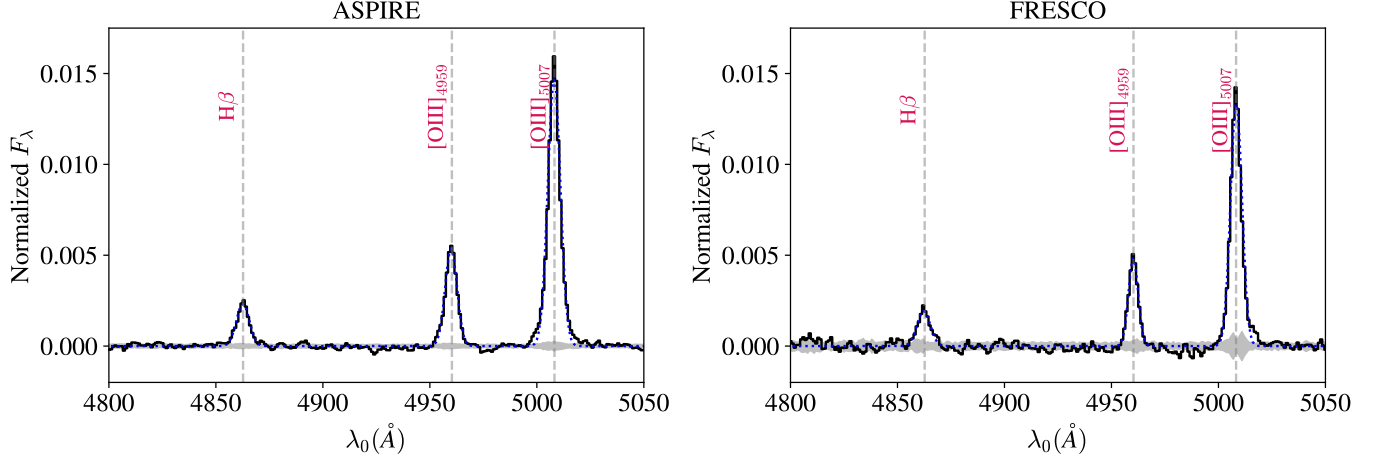


Figure 17. Median stacked 1D rest-frame spectra of galaxies in ASPIRE and FRESCO. The fluxes are normalized by [O III] 4959+5007 flux to avoid excessive weighting towards bright sources. The gray shadow represents the spectra uncertainty. The blue dotted lines are the best-fit Gaussian models.

Table 3. Measurements from stacked 1D spectra in ASPIRE and FRESCO.

Property	ASPIRE	FRESCO
$\log(R3)$	0.79 ± 0.02	0.78 ± 0.04
$^a F_{[\text{O III}]4959}$	34.17 ± 0.70	30.18 ± 1.64
$^a F_{H\beta}$	16.10 ± 0.60	16.51 ± 1.45
$^b 12 + \log(\text{O}/\text{H})_{\text{Sanders+23}}$	$7.61^{+0.07}_{-0.05}$	$7.57^{+0.18}_{-0.10}$
$^c 12 + \log(\text{O}/\text{H})_{\text{Nakajima+22}}$	$7.78^{+0.09}_{-0.06}$	$7.74^{+0.16}_{-0.10}$

NOTE—^aNormalized as $F_{[\text{O III}]5007} = 100$

^bWith [R. L. Sanders et al. \(2024\)](#) calibration assuming lower branch solution.

^cWith [K. Nakajima et al. \(2022\)](#) calibration assuming lower branch solution.

to the observed axis ratios and then randomly assigned the axis ratios to the Sérsic model of the emission maps using the normal distribution. Additionally, we found that $\text{SNR}_{[\text{O III}]}$ is not strongly correlated with other physical parameters, so we randomly assigned $\text{SNR}_{[\text{O III}]}$ for these galaxies using a log-normal distribution that best represents the observed $\text{SNR}_{[\text{O III}]}$ distribution. Finally, we construct two different mock sets, the one with metallicity gradients randomly chosen from a uniform distribution $\mathcal{U}(-0.6, 0)$, and the other with all zero gradients. We measure the median metallicity gradient from the stacked maps [O III] and H β . The inferred metallicity gradients are $k = -0.34 \pm 0.13$ for the negative gradient dataset and $k = -0.01 \pm 0.13$ for the flat gradient dataset, as shown in Fig. 18. We have found that the gradient measured from the stacked emission maps can effectively represent the median gradients of the mock sample. Therefore, the gradients observed for galaxies at $z \approx 6 - 7$ are strong representations of the populations.

H. THE IMPACT ON THE METALLICITY OF THE VARIATION OF THE IONIZATION PARAMETER (U)

The observed line ratios depend on both metallicity and the ionization parameter (U, the ratio of the number of ionizing photons to gas number density). Galaxies at $z \sim 2 - 9$ typically have values of $\log(U)$ varying from -3.5 to

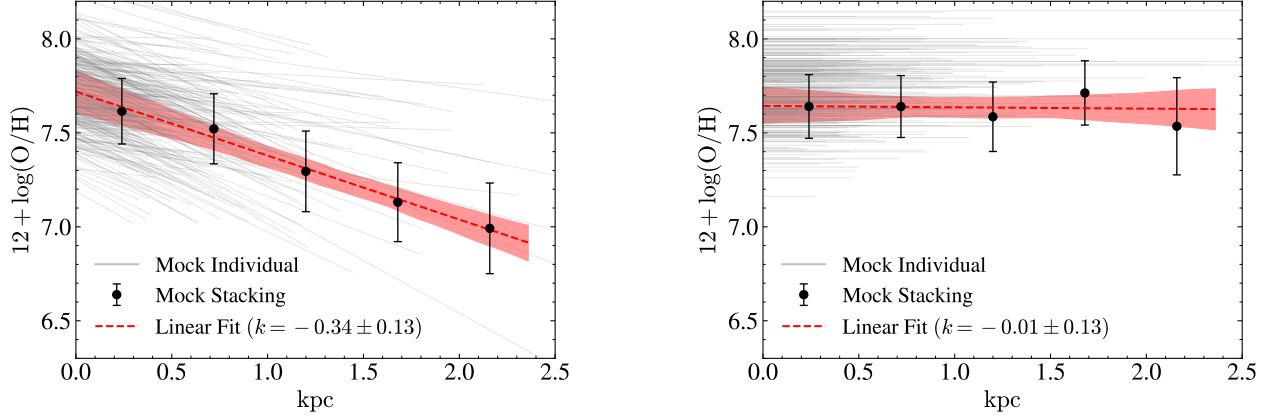


Figure 18. Metallicity gradients in the mock test. In the left panel, the metallicity gradients of mock galaxies are randomly chosen from a uniform distribution $\mathcal{U}(-0.6, 0)$, while all the mock galaxies in the right panel have a zero gradient. Gray lines represent individual galaxies, with length representing twice the effective radius of the galaxy. Black points are measured from the stacked emission maps, with errorbars showing the 1σ uncertainty. The red dashed line shows the linear fitting to the measured points, and the red shadowed region is its 1σ confidence interval.

-1.5 (A. L. Strom et al. 2018; N. A. Reddy et al. 2023; M. Tang et al. 2023; J. R. Trump et al. 2023). The varied $\log(\text{U})$ can lead to a line-ratio gradient, even if there is no gradient in metallicity.

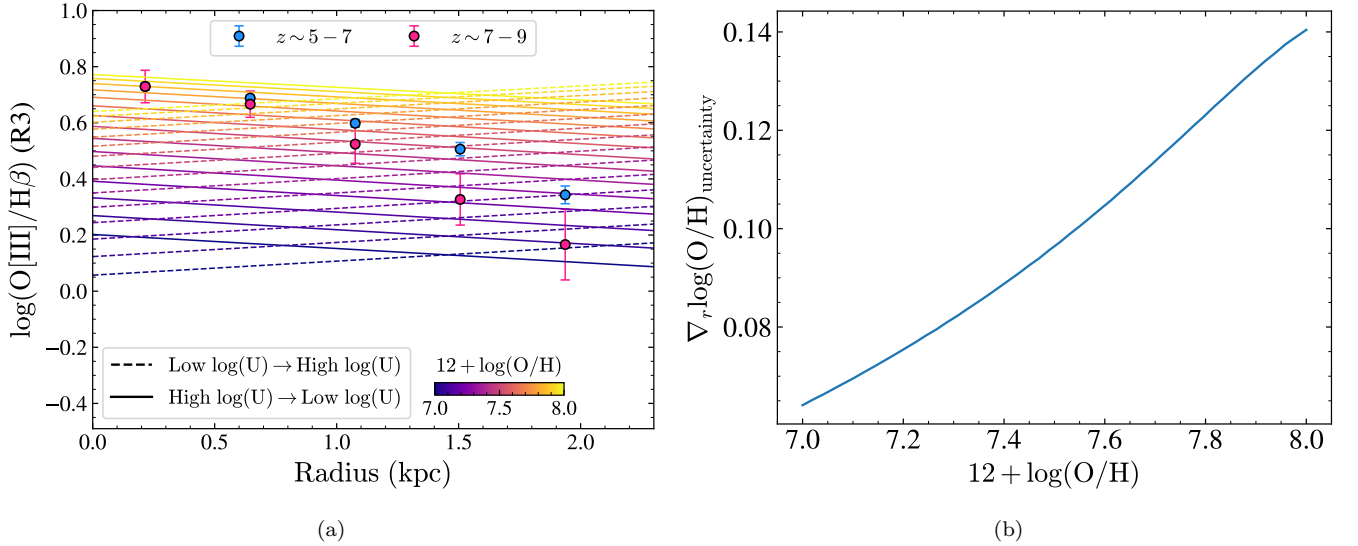


Figure 19. (a) The observed R3 ratio in two redshift bins (red and blue circles), and the modeled R3 ratio from P. Garg et al. (2024). The models are color-coded with different metallicities in the range $12 + \log(\text{O}/\text{H}) = 7-8$. We show that the ionization parameter, U , varies from high in the center to low in the outskirts (solid line), and from low in the center to high in the outskirts (dashed line). (b) The uncertainty of metallicity gradient due to variation of ionization parameters.

To quantify the effects of varied $\log(\text{U})$ on measured metallicity gradients, we examine the dependence of the observed line ratio on U using the recent photoionization model provided by P. Garg et al. (2024). We applied their two models that simulate galaxies at $z \approx 5$, one with low ionization (median $\log(\text{U}) = -2.3$) and the other with high ionization (median $\log(\text{U}) = -0.86$). In Fig. 19a, we vary $\log(\text{U})$ from the center to the outskirts, transitioning either from low to high or from high to low. In Fig. 19b, we observe that different $\log(\text{U})$ can produce the maximum $\approx 0.1-0.2$ dex in the R3 ratio. While our observed R3 ratios vary by ≈ 0.5 dex, larger than can be explained by ionization parameter. As a result, different metallicities are required to reproduce the observed R3 ratios.

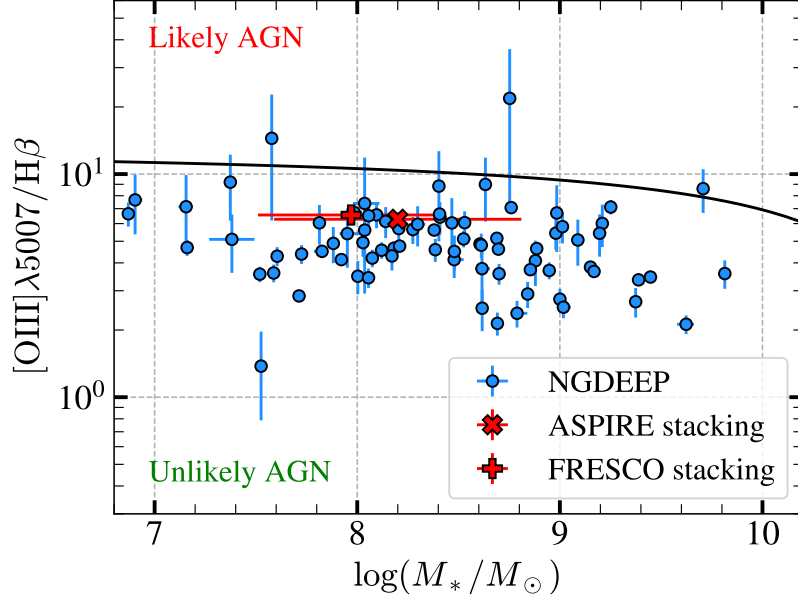


Figure 20. The mass-excitation diagram for our sample galaxies. The blue points show individual measurements in NGDEEP and the red cross represents the median stacked result in ASPIRE and FRESCO. The solid lines are the demarcation scheme (A. L. Coil et al. 2015), where the points below the line are unlikely to be AGNs. Our sample galaxies in NGDEEP at $z \approx 1 - 3$ are safely excluded from being AGNs, and the ASPIRE and FRESCO stackings at $z \approx 6 - 7$ are also negligibly contaminated by possible AGNs.

To further quantify the uncertainty induced by varied $\log(U)$. We consider the measurement of a galaxy out to radius $R = 2$ kpc (as in our observations). Assuming the galaxy with uniform metallicity, but with ionization parameter $\log(U)$ varying with radius, we expect to observe varied R3 ratios. Then we use the calibration from R. L. Sanders et al. (2024) to derive metallicity from such observed line ratios, we obtain a spurious non-zero metallicity gradient – either positive or negative – corresponding to positive or negative gradients of $\log(U)$, respectively. In right panel of Fig. 19, we show such uncertainty as a function of galaxy metallicity Z_{gal} . We see that the error increases with metallicity. For typical galaxies in our sample with $Z_{\text{gal}} \sim 7.6$, the induced uncertainty is ≈ 0.1 dex kpc^{-1} , with the maximum variation of $\log(U)$ from $\log(U) = -2.3$ to -0.86 (P. Garg et al. 2024). Compared with the metallicity gradient of $\nabla Z \approx -0.4$ dex kpc^{-1} in our JWST observations, the maximum uncertainty induced by $\log(U)$ falls within the range of the statistical error. In literature, H. Poetrodjojo et al. (2018) found no significant variation in ionization parameters with ionization parameter gradients $\lesssim 0.05$ dex R_e^{-1} . If the gradient continues to $4 R_e \sim 2$ kpc, the variation in $\log(U)$ is only $\lesssim 0.2$ dex, much less than we assumed extreme variation ~ 1.44 dex. Thus, possible variation in U does not dominate the variation of line ratios (also see G. Cresci et al. 2010), and we expect lower uncertainty < 0.1 dex kpc^{-1} from varied $\log(U)$.

I. AGN CONTAMINATION

Since galaxies with AGNs are powered by additional AGN ionization, the standard metallicity calibrations (F. Bian et al. 2018; R. L. Sanders et al. 2024) are not suitable for AGN-contaminated sources. As such, we remove sources with possible AGN contamination. We use the mass-excitation diagram (A. L. Coil et al. 2015) to separate AGNs from star-forming galaxies. In Fig. 20, we have removed the sources $\geq 2\sigma$ from the demarcation. As shown, all of our sample galaxies are classified as typical star-forming galaxies.

Nevertheless, we also note that AGN may be more common in high- z galaxies. Y. Harikane et al. (2023); R. Maiolino et al. (2023) find red AGN with broad line features take a fraction as high as 10 – 20% at $z > 5$. Y. Harikane et al. (2023); R. Maiolino et al. (2023) suggest an offset for high- z AGN in the BPT diagram (and also in the mass-excitation diagram). R. Maiolino et al. (2023) provided several possibilities for high- z AGN offset in BPT diagram. One is that the narrow line emission is dominated by star formation, instead of AGN narrow line region (NLR). R. Maiolino et al. (2024) further suggested a high covering factor of the broad line region (BLR), prohibiting photons from escaping

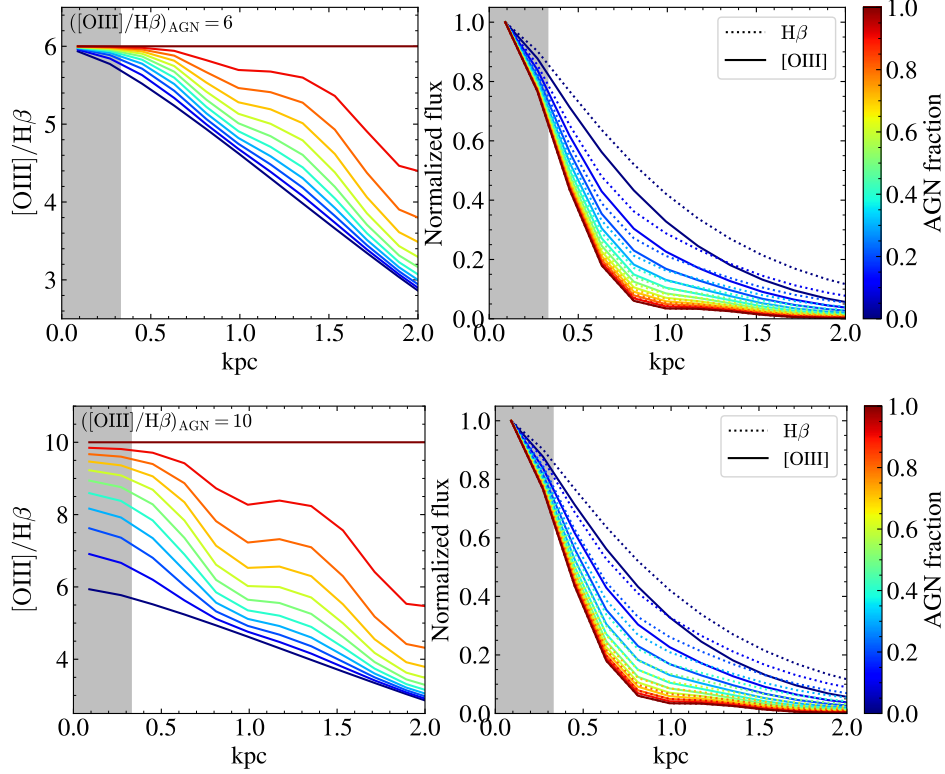


Figure 21. The $[\text{O III}]/\text{H}\beta$ ratios (left) and their normalized profiles (right) with varying AGN fractions. The profiles are normalized by their central peak flux. In the top row, we assume a ratio of $([\text{O III}]/\text{H}\beta)_{\text{AGN}} = 6$, indicative of AGN emission comparable to typical star-forming galaxies at $z > 5$. In the bottom row, we consider an enhanced $[\text{O III}]$ emission from AGN, with a ratio of $([\text{O III}]/\text{H}\beta)_{\text{AGN}} = 10$.

to produce NLR emissions. An alternative explanation is that the NLR of high- z AGN is characterized by low metallicities (Y. Harikane et al. 2023; R. Maiolino et al. 2023). With decreasing metallicity in NLR, the emission line ratios shift from the local AGN locus to be mixed with the star-forming locus. AGN may be confused with low-mass, low-metallicity star-forming-dominated galaxies. Y. I. Izotov & T. X. Thuan (2008) show that AGN non-thermal radiation should contribute less than 10% to total ionizing radiation in metal-poor ($12 + \log(\text{O}/\text{H}) < 8$) AGN host galaxies, to reproduce the shift in BPT diagram. In this case, the narrow line emission from black holes should still be much weaker ($< 10\%$) than emissions from stellar radiation. From these models, AGN contamination in our sample should be small, and the $[\text{O III}]$ fluxes should come predominately from star formation.

Type-2 AGN, however, has been observed to be similar or more prevalent than type-1 AGN at high-redshift. A similar issue has been raised by J. Scholtz et al. (2023) that type-2 AGN have offsets in the BPT diagram, and it is very difficult to distinguish from star-forming galaxies using the standard BPT diagram unless high ionization lines are detected. J. Scholtz et al. (2023) selected type-2 AGN from a sample of galaxies with JWST/NIRSpec observations using high ionization lines in combination with UV transitions. While they found that type-2 AGN have weaker $[\text{N II}]/\text{H}\alpha$ ratios, they have a similar $[\text{O III}]/\text{H}\beta$ ratio to star-forming galaxies, and they measured the $[\text{O III}]/\text{H}\beta$ ratio to be 4.55 ± 0.15 and 4.70 ± 0.14 from stacked spectra of type-2 AGN and star-forming galaxies, respectively. Although it is difficult to distinguish type-2 AGN solely based on $[\text{O III}]/\text{H}\beta$ ratios, nevertheless, the central AGN should not significantly change the line ratios, as type-2 AGN contributes to a very similar amount of $[\text{O III}]$ and $\text{H}\beta$ emission as star-forming galaxies do.

To further quantify the impact of AGN on emission maps at $z > 5$, we have conducted a set of mock tests. We define the AGN fraction as the AGN contribution of $[\text{O III}]$ luminosity to the total $[\text{O III}]$ luminosity of the galaxy. As AGN are point sources, their emissions are detected as PSF components in emission maps. We construct a mock galaxy at $z \sim 6$ with a sérsic profile, and we add a central AGN component as a NIRCам F356W PSF. We assume two cases, the one with high $[\text{O III}]/\text{H}\beta$ ratio as high as $([\text{O III}]/\text{H}\beta)_{\text{AGN}} = 10$, as is expected at lower redshift (S.

Juneau et al. 2014), and another with similar ratio as star-forming galaxy $([\text{O III}]/\text{H}\beta)_{\text{AGN}} = 6$, as is expected by recent AGN observations at $z > 4$ (J. Scholtz et al. 2023). In Fig. 21, we show the $[\text{O III}]$, $\text{H}\beta$ line, and line ratio profiles in galaxies with different AGN fractions. We find that an obvious sign of AGN in emission maps is a bump in line ratio profiles at $r = 1.5$ kpc, induced by the wing of PSF. We can also observe that when $([\text{O III}]/\text{H}\beta)_{\text{AGN}} = 10$, higher than the line ratio from star formation, the AGN component contributes to a steeper $[\text{O III}]/\text{H}\beta$ profile as a result of boosting $[\text{O III}]$ emission in the center. However, if the AGN emission $([\text{O III}]/\text{H}\beta)_{\text{AGN}} = 6$ is comparable to the emission from galaxies (e.g., as revealed in J. Scholtz et al. 2023), the change of $[\text{O III}]/\text{H}\beta$ slope is quite small if AGN fraction is below $\sim 50\%$. R. Maiolino et al. (2023, 2024) suggested that AGN NLR emission is subdominant possibly due to either the high cover fraction in BLR or the low metallicity nature of NLR. The AGN component should contribute to a small fraction of the total $[\text{O III}]$ emissions from the host galaxy. M. Curti et al. (2024) also found no significant change in MZR when including AGN candidates assuming the metallicity calibration is still valid with the contribution of AGN ionization. As a result, our measured metallicity gradient based on the $[\text{O III}]/\text{H}\beta$ is less likely to be biased by AGN contamination.

Similar concerns are raised by J. R. Trump et al. (2011). The positive metallicity gradient observed at $z \sim 2$ is associated with more extended $\text{H}\beta$ emission, resulting in a negative gradient of the R3 ratio. Since the metallicities fall on the upper branch of the R3 calibration, this corresponds to a positive gradient in metallicity. J. R. Trump et al. (2011) found more extended $\text{H}\beta$ emission at $z \sim 2$. They attributed this to the consequence of enhanced $[\text{O III}]$ emission boosted by central AGN. Based on our earlier discussion, if AGN are unlikely to dominate the flux profile, the observed trend can also be interpreted as a result of positive metallicity gradients, consistent with our results at $z \sim 2$.

J. HALO MASS-REDSHIFT DISTRIBUTION AND ANALYTIC PREDICTIONS

We estimate the halo masses using the empirical stellar-to-halo mass relation in M. Shuntov et al. (2022). It is worth noting that their highest redshift bin extends only to $z = 5.5$, whereas we extended this relation for our $5 < z < 9$ sample. We should be cautious to this halo mass estimation, which may deviate at higher redshifts. As this is a qualitative comparison, we are less sensitive to accurate halo masses. In Fig. 22, we show the halo mass vs. redshift for the whole galaxy sample, in comparison with the analytic predictions of cold/hot accretion (A. Dekel & Y. Birnboim 2006; A. Dekel et al. 2009), and FFB (A. Dekel et al. 2023). We find that at $z \gtrsim 2$, most of the sample galaxies could sustain cold streams. While at lower redshift $z \lesssim 2$, the inflow gas is expected to be shock heated for massive galaxies, and only low mass galaxies can be fed with cold streams. This suggests that the cold mode accretion is important at $z \sim 2$ and contributes to flat gradients, and the hot mode accretion gradually increases towards low-redshift and allows negative gradients.

At higher redshift $z \gtrsim 6$, most of the galaxies can fall within FFB regime. In massive halos above the green solid line, mean gas density in the ISM is expected reach FFB threshold to boost global star formation in FFB mode. The green dashed line shows the model with higher density contrast ($c = 10$, Eq. 37 in A. Dekel et al. 2023) between FFB clouds and the mean overdensity. For less massive galaxies between green solid and dashed lines, the gas clouds can reach FFB threshold when their contract reaching higher density than the mean gas density, so that the FFB can happen locally. If the gas can further collapse into higher density, we would expect lower halo mass threshold for the occurrence of local FFB. As a result, local FFB might happen in most of our sample galaxies, and supports the steep negative gradients in FFB scenario. This qualitative comparison hints the transition of different gas accretion and star formation scenarios across redshifts, supporting our interpretation in the main text.

K. DEGENERACIES IN SIMULATIONS

Simulations have shown that the radial distribution of metals is shaped by factors such as gas-phase structure, feedback mechanisms, metal yields, and diffusion in simulations (S. Roca-Fàbrega et al. 2024). Below, we briefly discuss the impact of these factors.

(i) **The gas-phase structure.** MUGS, FIRE, and FOGGIE all allow explicitly the multi-phase ISM, while the ISM gas in EAGLE and TNG50 rely on the effective equation of state (eEOS, e.g., V. Springel & L. Hernquist (2003)), resulting in different levels of metal mixing. The application of eEOS in TNG50 is not able to explicitly model small-scale (i.e. < 100 pc) structures that pressurize the ISM, such as turbulence (Z. S. Hemler et al. 2021). The unresolved small-scale turbulence may serve to radially mix chemically enriched gas and flatten the metallicity gradients (P. Sharda et al. 2021c). Moreover, they are not affected by the continuous burst of feedback, and they

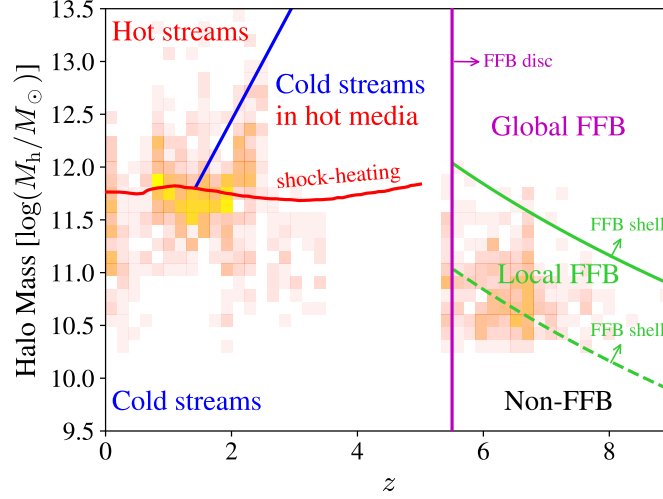


Figure 22. The 2d-histogram of halo mass and redshift distribution of all sample galaxies. The regimes predicted by analytic models of cold accretion, hot accretion (A. Dekel & Y. Birnboim 2006; A. Dekel et al. 2009), and FFB (A. Dekel et al. 2023) are demarcated by lines in different colors.

go through more steady star formation which consequently develops a steeper gradient (Z. S. Hemler et al. 2021). However, with continuous feedback, it can erase the metallicity gradient in simulations with multi-phase ISM (such as FIRE (X. Ma et al. 2017)).

(ii) Feedback strategy. The different implementations of feedback (e.g., stellar and AGN feedback) in different simulations yield vastly different halo baryon fractions (Fig. 9 of R. A. Crain & F. van de Voort (2023)), in particular at the low-mass end, influencing the mixing and evacuation of gas to different extents. TNG50 simulations include the feedback of both stars and AGN (Z. S. Hemler et al. 2021), and their sub-grid prescriptions result in smooth star formation and feedback. FIRE does not have AGN feedback, but their explicitly modeled strong stellar and radiative feedback will also play a significant role in the evacuation of gas from the circumgalactic medium (CGM) (X. Ma et al. 2017; X. Sun et al. 2024). For the supernova feedback, previous simulations have shown a factor of $\approx 2.5\times$ more powerful supernova feedback could lead to ≈ 0.2 dex kpc^{-1} higher metallicity gradient at $z \geq 1.5$ (B. K. Gibson et al. 2013). However, the supernova feedback prescription in FOGGIE simulations is insufficient and unable to expel enough metal-rich gas (A. Acharyya et al. 2025). Different modes of feedback can also cause different extents of gas transport. I. Shimizu et al. (2019) found kinetic-only feedback can more easily enrich the ISM and CGM than thermal-only feedback, leading to more metal-enriched outskirts and a shallower gradient. They also found turn-off cooling also influences SNe feedback efficiency. Thus, how we treat feedback and how we include different fractions of feedback models lead to different extents of metal enrichment.

(iii) The metal yield and diffusion. How the mass of stars converts to the mass of metals in the ISM and how the metal mixes with the ISM in simulations also influence the galaxy metallicity gradient. These two processes are described by the parameters of metal yield (the ratio between the metal mass and the stellar mass) and the yield reduction factor (ϕ_y , the fraction of metals mixed with the ISM). FIRE, MUGS and FOGGIE use three different metal yields, with FIRE using Type II Supernova (SNII), Type Ia Supernova (SNIa) and winds as sources (yields from S. E. Woosley & T. A. Weaver (1995), K. Iwamoto et al. (1999) and R. G. Izzard et al. (2004), respectively), MUGS only accounts for SNII (C. M. Raiteri et al. 1996) and SNIa (F. K. Thielemann et al. 1986), and FOGGIE uses a custom recipe for the metal enrichment. Different metal yield influences the absolute metals produced in galaxies, and, for example, can imprint on the normalization of mass-metallicity relations (e.g. X. Ma et al. 2016; A. Marszewski et al. 2024). While the absolute amount of metal is less important on the metallicity gradient, as the gradient relies on the relative abundance of metal at different radii. For the yield reduction factor, P. Sharda et al. (2021c) has shown that the galaxy metallicity gradient is inversely correlated with ϕ_y . In FOGGIE simulation, they found the scatter of metallicity gradients may be related to this yield reduction factor (A. Acharyya et al. 2025). Note that the gas-phase metallicity gradient measures the radial change of the oxygen abundance relative to hydrogen in the ionized gas, and it is less prone to the different values of stellar yield values assumed in the models. A factor of $10\times$ increase in the yield

reduction factor can only bring about $\lesssim 0.2$ dex change in gradient slopes according to analytical models (P. Sharda et al. 2021c). Thus, different cosmological simulation results can be compared here, for qualitative comparison. ”

These factors all influence the distribution of gas-phase metallicity in galaxies to different extents. Although the degeneracies inherent in these different simulation architectures complicate the ability to isolate individual effects based on limited observation constraints, understanding the relative importance of these factors helps improve our interpretation of galaxy formation and evolution processes. It is hard to quantify the exact mechanism to drive the metallicity gradients we observed, we generally prefer stronger feedback at $z \sim 2$ and less efficient feedback at higher redshift $z > 5$. This nuanced understanding is essential for future studies aiming to reconcile simulation outcomes with observational data.

L. MEASURED QUANTITIES OF INDIVIDUAL GALAXIES.

Table 4. Measured quantities of individual galaxies in our sample.

Field	ID	ra	dec	redshift	$\log(M_*/M_\odot)$	SFR	$12 + \log(\text{O}/\text{H})$	$\nabla_r \log(\text{O}/\text{H})$
-	-	[deg]	[deg]	-	-	$M_\odot \text{ yr}^{-1}$	-	[dex kpc $^{-1}$]
ASPIRE	Zgrad-1	315.583439	-14.976233	6.66	$8.41^{+0.10}_{-0.06}$	$25.67^{+6.76}_{-3.23}$	$7.73^{+0.14}_{-0.18}$	-0.18 ± 0.26
ASPIRE	Zgrad-2	137.723621	-4.222954	6.64	$8.24^{+0.08}_{-0.03}$	$17.26^{+3.53}_{-1.06}$	$7.75^{+0.12}_{-0.17}$	-0.16 ± 0.26
ASPIRE	Zgrad-3	137.700518	-4.272600	6.21	$8.22^{+0.04}_{-0.05}$	$16.67^{+1.62}_{-1.70}$	$7.72^{+0.15}_{-0.20}$	-0.25 ± 0.27
ASPIRE	Zgrad-4	46.318882	-31.839629	6.67	$8.55^{+0.09}_{-0.09}$	$33.19^{+6.64}_{-5.98}$	$7.61^{+0.21}_{-0.21}$	-0.15 ± 0.28
ASPIRE	Zgrad-5	17.475148	-30.798016	6.71	$8.35^{+0.09}_{-0.06}$	$22.16^{+4.98}_{-2.75}$	$7.69^{+0.16}_{-0.19}$	-0.10 ± 0.39
ASPIRE	Zgrad-6	140.957012	4.049241	6.39	$8.04^{+0.03}_{-0.02}$	$10.98^{+0.69}_{-0.60}$	$7.31^{+0.28}_{-0.17}$	-0.45 ± 0.31
NGDEEP	00060	53.150753	-27.804927	2.04	$7.52^{+0.02}_{-0.02}$	$1.36^{+0.05}_{-0.06}$	$7.87^{+0.06}_{-0.05}$	0.14 ± 0.05
NGDEEP	00096	53.151582	-27.803721	2.12	$8.41^{+0.03}_{-0.02}$	$1.83^{+0.10}_{-0.13}$	$8.29^{+0.05}_{-0.05}$	-0.07 ± 0.02
NGDEEP	00173	53.148643	-27.801635	2.12	$8.10^{+0.03}_{-0.05}$	$1.52^{+0.09}_{-0.07}$	$7.98^{+0.04}_{-0.04}$	-0.09 ± 0.04
NGDEEP	00197	53.153745	-27.801119	2.02	$7.16^{+0.03}_{-0.03}$	$1.34^{+0.05}_{-0.07}$	$7.87^{+0.05}_{-0.04}$	0.05 ± 0.04
NGDEEP	00228	53.150438	-27.800622	2.62	$9.00^{+0.02}_{-0.02}$	$3.26^{+0.22}_{-0.20}$	$8.50^{+0.06}_{-0.08}$	0.08 ± 0.07
NGDEEP	00242	53.160060	-27.800122	2.22	$8.00^{+0.01}_{-0.01}$	$1.11^{+0.04}_{-0.04}$	$7.93^{+0.07}_{-0.07}$	-0.11 ± 0.13
NGDEEP	00310	53.156367	-27.799048	2.67	$9.37^{+0.01}_{-0.01}$	$1.29^{+0.07}_{-0.06}$	$8.52^{+0.04}_{-0.05}$	0.07 ± 0.05
NGDEEP	00317	53.145614	-27.798979	2.62	$9.62^{+0.04}_{-0.04}$	$11.65^{+0.99}_{-0.82}$	$8.61^{+0.04}_{-0.04}$	-0.03 ± 0.05
NGDEEP	00407	53.171345	-27.797899	1.99	$8.84^{+0.02}_{-0.02}$	$1.23^{+0.13}_{-0.13}$	$8.47^{+0.04}_{-0.05}$	-0.15 ± 0.03
NGDEEP	00413	53.152521	-27.797787	3.00	$7.58^{+0.04}_{-0.03}$	$2.08^{+0.08}_{-0.11}$	$8.05^{+0.07}_{-0.07}$	-0.01 ± 0.13
NGDEEP	00436	53.170460	-27.797382	2.08	$9.02^{+0.04}_{-0.03}$	$1.72^{+0.12}_{-0.12}$	$8.42^{+0.05}_{-0.07}$	-0.03 ± 0.04
NGDEEP	00466	53.168830	-27.796994	1.99	$8.61^{+0.01}_{-0.01}$	$4.08^{+0.19}_{-0.24}$	$8.05^{+0.05}_{-0.05}$	-0.04 ± 0.02
NGDEEP	00508	53.173491	-27.796419	2.75	$7.38^{+0.11}_{-0.11}$	$0.99^{+0.09}_{-0.08}$	$8.01^{+0.12}_{-0.10}$	-0.19 ± 0.10
NGDEEP	00536	53.148336	-27.796032	2.02	$8.61^{+0.03}_{-0.03}$	$1.56^{+0.11}_{-0.13}$	$8.34^{+0.05}_{-0.05}$	-0.00 ± 0.03
NGDEEP	00618	53.146372	-27.795289	2.63	$8.69^{+0.01}_{-0.01}$	$2.38^{+0.13}_{-0.11}$	$8.59^{+0.04}_{-0.05}$	-0.13 ± 0.07
NGDEEP	00619	53.143575	-27.795297	2.02	$8.18^{+0.02}_{-0.01}$	$7.02^{+0.33}_{-0.32}$	$8.09^{+0.07}_{-0.06}$	0.01 ± 0.01
NGDEEP	00683	53.148356	-27.794324	2.63	$7.73^{+0.02}_{-0.02}$	$3.21^{+0.13}_{-0.11}$	$8.14^{+0.11}_{-0.11}$	-0.10 ± 0.02
NGDEEP	00729	53.172439	-27.793993	2.80	$8.95^{+0.02}_{-0.01}$	$5.88^{+0.12}_{-0.11}$	$8.39^{+0.06}_{-0.07}$	-0.03 ± 0.03
NGDEEP	00745	53.152584	-27.793907	3.07	$9.71^{+0.01}_{-0.01}$	$15.44^{+0.59}_{-0.39}$	$8.34^{+0.03}_{-0.03}$	0.00 ± 0.02
NGDEEP	00760	53.165077	-27.793719	2.34	$8.89^{+0.01}_{-0.01}$	$6.19^{+0.16}_{-0.15}$	$8.35^{+0.04}_{-0.04}$	-0.04 ± 0.01
NGDEEP	00782	53.147407	-27.793410	2.79	$7.81^{+0.02}_{-0.02}$	$3.08^{+0.15}_{-0.29}$	$8.12^{+0.09}_{-0.08}$	-0.08 ± 0.11
NGDEEP	00784	53.170795	-27.793366	2.67	$7.71^{+0.02}_{-0.02}$	$2.79^{+0.25}_{-0.19}$	$7.93^{+0.09}_{-0.07}$	0.59 ± 0.05
NGDEEP	00789	53.172714	-27.793316	2.81	$8.88^{+0.02}_{-0.02}$	$2.08^{+0.32}_{-0.31}$	$8.36^{+0.07}_{-0.07}$	-0.32 ± 0.08

Field	ID	ra	dec	redshift	$\log(M_*/M_\odot)$	SFR	$12 + \log(\text{O}/\text{H})$	$\nabla_r \log(\text{O}/\text{H})$
-	-	[deg]	[deg]	-	-	$M_\odot \text{ yr}^{-1}$	-	[dex kpc $^{-1}$]
NGDEEP	00860	53.153127	-27.792447	3.32	$8.63^{+0.02}_{-0.02}$	$4.95^{+0.18}_{-0.23}$	$8.17^{+0.06}_{-0.05}$	0.05 ± 0.09
NGDEEP	00868	53.151284	-27.792470	1.84	$8.85^{+0.03}_{-0.03}$	$5.95^{+0.21}_{-0.20}$	$8.28^{+0.04}_{-0.04}$	0.04 ± 0.01
NGDEEP	00917	53.147644	-27.791848	1.87	$7.95^{+0.07}_{-0.04}$	$0.45^{+0.02}_{-0.02}$	$8.41^{+0.05}_{-0.06}$	-0.26 ± 0.11
NGDEEP	00928	53.146782	-27.791739	2.79	$8.40^{+0.03}_{-0.02}$	$1.16^{+0.09}_{-0.08}$	$7.94^{+0.10}_{-0.10}$	-0.13 ± 0.12
NGDEEP	00996	53.178202	-27.790838	1.76	$8.62^{+0.02}_{-0.02}$	$0.41^{+0.02}_{-0.02}$	$8.19^{+0.08}_{-0.11}$	0.08 ± 0.18
NGDEEP	01014	53.153116	-27.790565	3.32	$8.14^{+0.02}_{-0.02}$	$5.61^{+0.25}_{-0.45}$	$7.96^{+0.07}_{-0.08}$	0.11 ± 0.04
NGDEEP	01066	53.167405	-27.790198	2.76	$8.27^{+0.02}_{-0.02}$	$3.63^{+0.23}_{-0.15}$	$8.16^{+0.08}_{-0.08}$	-0.24 ± 0.05
NGDEEP	01145	53.171118	-27.789204	2.84	$6.90^{+0.04}_{-0.02}$	$0.81^{+0.07}_{-0.04}$	$7.93^{+0.08}_{-0.08}$	0.08 ± 0.19
NGDEEP	01173	53.141930	-27.788913	2.71	$9.09^{+0.03}_{-0.03}$	$1.48^{+0.09}_{-0.08}$	$8.28^{+0.08}_{-0.07}$	0.03 ± 0.13
NGDEEP	01222	53.169688	-27.788158	3.18	$9.21^{+0.01}_{-0.01}$	$7.56^{+0.25}_{-0.25}$	$8.29^{+0.05}_{-0.04}$	-0.04 ± 0.06
NGDEEP	01223	53.146252	-27.788128	2.00	$8.30^{+0.04}_{-0.04}$	$1.00^{+0.04}_{-0.04}$	$8.20^{+0.04}_{-0.04}$	-0.07 ± 0.04
NGDEEP	01227	53.143415	-27.788081	3.40	$8.75^{+0.01}_{-0.01}$	$5.86^{+0.19}_{-0.17}$	$8.05^{+0.05}_{-0.05}$	-0.02 ± 0.11
NGDEEP	01233	53.152356	-27.788058	2.31	$8.39^{+0.01}_{-0.02}$	$2.52^{+0.08}_{-0.10}$	$8.23^{+0.06}_{-0.06}$	0.06 ± 0.04
NGDEEP	01237	53.163104	-27.787936	2.22	$7.37^{+0.03}_{-0.02}$	$0.57^{+0.06}_{-0.04}$	$8.08^{+0.05}_{-0.05}$	0.06 ± 0.06
NGDEEP	01255	53.174319	-27.787763	2.07	$8.20^{+0.02}_{-0.02}$	$1.43^{+0.03}_{-0.02}$	$8.09^{+0.06}_{-0.05}$	-0.02 ± 0.03
NGDEEP	01291	53.177252	-27.787383	3.00	$9.81^{+0.01}_{-0.01}$	$4.68^{+0.25}_{-0.24}$	$8.41^{+0.06}_{-0.06}$	-0.10 ± 0.04
NGDEEP	01346	53.180819	-27.787398	1.94	$8.93^{+0.04}_{-0.02}$	$2.54^{+0.18}_{-0.17}$	$8.39^{+0.03}_{-0.04}$	0.05 ± 0.02
NGDEEP	01385	53.180809	-27.786328	2.69	$8.76^{+0.01}_{-0.01}$	$23.20^{+0.43}_{-0.64}$	$8.13^{+0.04}_{-0.04}$	-0.09 ± 0.01
NGDEEP	01482	53.169359	-27.785060	1.90	$6.87^{+0.01}_{-0.01}$	$0.75^{+0.03}_{-0.02}$	$7.71^{+0.08}_{-0.10}$	0.07 ± 0.05
NGDEEP	01489	53.149093	-27.785142	2.06	$9.07^{+0.02}_{-0.02}$	$2.79^{+0.20}_{-0.20}$	$8.39^{+0.05}_{-0.05}$	-0.04 ± 0.02
NGDEEP	01494	53.178699	-27.785025	2.11	$8.70^{+0.03}_{-0.02}$	$2.95^{+0.20}_{-0.18}$	$8.38^{+0.05}_{-0.05}$	-0.00 ± 0.02
NGDEEP	01544	53.142345	-27.784448	2.94	$8.04^{+0.02}_{-0.02}$	$8.36^{+0.25}_{-0.26}$	$8.09^{+0.10}_{-0.12}$	0.01 ± 0.03
NGDEEP	01583	53.144136	-27.783940	2.81	$8.48^{+0.05}_{-0.03}$	$2.28^{+0.29}_{-0.24}$	$8.26^{+0.09}_{-0.10}$	-0.00 ± 0.08
NGDEEP	01633	53.157671	-27.783403	2.63	$8.17^{+0.02}_{-0.02}$	$2.59^{+0.17}_{-0.12}$	$8.22^{+0.10}_{-0.12}$	0.00 ± 0.06
NGDEEP	01634	53.182599	-27.783504	2.07	$8.47^{+0.02}_{-0.02}$	$1.63^{+0.10}_{-0.10}$	$8.28^{+0.05}_{-0.05}$	0.01 ± 0.03
NGDEEP	01635	53.182278	-27.783395	2.07	$8.54^{+0.02}_{-0.02}$	$3.45^{+0.13}_{-0.13}$	$8.33^{+0.04}_{-0.05}$	-0.00 ± 0.02
NGDEEP	01641	53.167902	-27.783264	2.08	$7.88^{+0.03}_{-0.03}$	$0.70^{+0.03}_{-0.03}$	$8.20^{+0.06}_{-0.06}$	-0.04 ± 0.08
NGDEEP	01751	53.167504	-27.781909	2.07	$8.12^{+0.01}_{-0.01}$	$2.36^{+0.26}_{-0.23}$	$7.87^{+0.05}_{-0.04}$	0.01 ± 0.03
NGDEEP	01774	53.165166	-27.781715	2.22	$8.69^{+0.01}_{-0.01}$	$5.49^{+0.34}_{-0.33}$	$8.15^{+0.05}_{-0.05}$	0.08 ± 0.01
NGDEEP	01786	53.151504	-27.781429	2.30	$8.41^{+0.02}_{-0.02}$	$3.05^{+0.15}_{-0.11}$	$8.12^{+0.05}_{-0.05}$	-0.07 ± 0.04
NGDEEP	01865	53.154815	-27.780452	2.57	$7.53^{+0.02}_{-0.02}$	$2.19^{+0.26}_{-0.23}$	$8.10^{+0.12}_{-0.11}$	-0.12 ± 0.09
NGDEEP	01874	53.157122	-27.780335	3.01	$7.94^{+0.02}_{-0.01}$	$3.63^{+0.11}_{-0.14}$	$8.05^{+0.09}_{-0.07}$	-0.05 ± 0.08
NGDEEP	01893	53.152903	-27.780194	1.85	$9.06^{+0.02}_{-0.02}$	$3.20^{+0.12}_{-0.13}$	$8.39^{+0.04}_{-0.04}$	0.02 ± 0.02
NGDEEP	01918	53.150506	-27.779833	3.07	$8.14^{+0.03}_{-0.03}$	$1.93^{+0.23}_{-0.16}$	$8.08^{+0.10}_{-0.10}$	-0.01 ± 0.09
NGDEEP	01966	53.157887	-27.779274	1.84	$8.62^{+0.04}_{-0.03}$	$0.61^{+0.05}_{-0.06}$	$8.32^{+0.05}_{-0.06}$	-0.10 ± 0.08
NGDEEP	01971	53.163741	-27.779153	3.27	$7.60^{+0.02}_{-0.03}$	$4.04^{+0.22}_{-0.26}$	$8.02^{+0.08}_{-0.08}$	-0.08 ± 0.03
NGDEEP	01986	53.176312	-27.778978	3.19	$9.15^{+0.01}_{-0.01}$	$20.62^{+0.71}_{-0.68}$	$8.39^{+0.05}_{-0.06}$	-0.10 ± 0.02
NGDEEP	02030	53.148379	-27.778614	3.32	$7.59^{+0.01}_{-0.01}$	$3.89^{+0.08}_{-0.11}$	$7.84^{+0.07}_{-0.06}$	0.22 ± 0.05
NGDEEP	02033	53.146435	-27.778375	1.86	$7.92^{+0.01}_{-0.01}$	$5.18^{+0.32}_{-0.24}$	$7.92^{+0.04}_{-0.03}$	0.06 ± 0.02
NGDEEP	02059	53.146068	-27.778118	1.86	$7.16^{+0.03}_{-0.04}$	$0.40^{+0.07}_{-0.05}$	$8.01^{+0.09}_{-0.12}$	0.02 ± 0.13

Field	ID	ra	dec	redshift	$\log(M_*/M_\odot)$	SFR	$12 + \log(\text{O}/\text{H})$	$\nabla_r \log(\text{O}/\text{H})$
-	-	[deg]	[deg]	-	-	$M_\odot \text{ yr}^{-1}$	-	[dex kpc $^{-1}$]
NGDEEP	02167	53.159582	-27.776803	3.43	$7.99^{+0.01}_{-0.01}$	$9.84^{+0.25}_{-0.23}$	$7.96^{+0.05}_{-0.04}$	-0.05 ± 0.04
NGDEEP	02180	53.144354	-27.776543	2.32	$8.06^{+0.02}_{-0.02}$	$1.56^{+0.07}_{-0.09}$	$8.14^{+0.08}_{-0.08}$	-0.15 ± 0.08
NGDEEP	02297	53.139253	-27.774915	1.84	$7.83^{+0.03}_{-0.04}$	$1.20^{+0.03}_{-0.04}$	$8.06^{+0.05}_{-0.04}$	-0.07 ± 0.03
NGDEEP	02304	53.167609	-27.774783	3.06	$8.04^{+0.02}_{-0.03}$	$1.93^{+0.19}_{-0.17}$	$8.08^{+0.11}_{-0.09}$	-0.02 ± 0.06
NGDEEP	02396	53.173541	-27.773773	1.88	$8.48^{+0.02}_{-0.03}$	$0.80^{+0.08}_{-0.06}$	$8.39^{+0.04}_{-0.05}$	0.05 ± 0.07
NGDEEP	02441	53.174137	-27.773047	3.44	$8.98^{+0.03}_{-0.03}$	$8.89^{+0.39}_{-0.32}$	$8.27^{+0.06}_{-0.05}$	-0.22 ± 0.04
NGDEEP	02446	53.148715	-27.773010	3.31	$9.20^{+0.01}_{-0.01}$	$10.61^{+0.30}_{-0.27}$	$8.28^{+0.06}_{-0.06}$	-0.05 ± 0.06
NGDEEP	02458	53.164201	-27.772965	2.84	$9.14^{+0.03}_{-0.02}$	$12.63^{+0.43}_{-0.38}$	$8.26^{+0.04}_{-0.04}$	0.04 ± 0.03
NGDEEP	02477	53.169766	-27.772581	3.32	$8.74^{+0.02}_{-0.03}$	$2.59^{+0.15}_{-0.12}$	$8.06^{+0.10}_{-0.09}$	0.06 ± 0.07
NGDEEP	02482	53.152918	-27.772575	1.84	$8.70^{+0.01}_{-0.01}$	$9.12^{+0.21}_{-0.46}$	$8.15^{+0.06}_{-0.05}$	0.09 ± 0.01
NGDEEP	02511	53.138215	-27.772110	2.81	$8.38^{+0.01}_{-0.01}$	$14.78^{+0.22}_{-0.19}$	$8.05^{+0.08}_{-0.05}$	0.05 ± 0.02
NGDEEP	02558	53.154498	-27.771493	2.22	$9.39^{+0.02}_{-0.01}$	$32.22^{+0.49}_{-1.05}$	$8.39^{+0.06}_{-0.10}$	0.08 ± 0.01
NGDEEP	02564	53.140975	-27.771279	2.22	$7.58^{+0.03}_{-0.03}$	$0.78^{+0.05}_{-0.04}$	$7.89^{+0.06}_{-0.06}$	-0.08 ± 0.11
NGDEEP	02578	53.144689	-27.771181	3.07	$9.25^{+0.02}_{-0.02}$	$22.67^{+0.41}_{-0.43}$	$8.27^{+0.03}_{-0.03}$	-0.03 ± 0.01
NGDEEP	02581	53.160020	-27.771086	1.84	$8.07^{+0.02}_{-0.02}$	$1.64^{+0.06}_{-0.06}$	$8.30^{+0.06}_{-0.06}$	0.05 ± 0.03
NGDEEP	02610	53.161804	-27.770720	3.32	$8.52^{+0.04}_{-0.03}$	$14.16^{+0.42}_{-0.45}$	$8.22^{+0.08}_{-0.08}$	-0.02 ± 0.02
NGDEEP	02649	53.152318	-27.770169	1.84	$9.45^{+0.02}_{-0.02}$	$10.07^{+0.35}_{-0.36}$	$8.35^{+0.04}_{-0.04}$	0.02 ± 0.01
NGDEEP	02685	53.173339	-27.769147	2.85	$8.80^{+0.02}_{-0.02}$	$1.95^{+0.11}_{-0.12}$	$8.14^{+0.08}_{-0.08}$	0.01 ± 0.10
NGDEEP	02724	53.169952	-27.768432	3.09	$9.01^{+0.01}_{-0.01}$	$5.13^{+0.12}_{-0.11}$	$8.14^{+0.08}_{-0.07}$	0.00 ± 0.05
NGDEEP	02743	53.165934	-27.767980	3.43	$8.06^{+0.02}_{-0.02}$	$9.06^{+0.81}_{-0.47}$	$8.08^{+0.07}_{-0.07}$	-0.06 ± 0.04
NGDEEP	02745	53.156388	-27.767910	2.02	$8.03^{+0.01}_{-0.01}$	$1.61^{+0.06}_{-0.07}$	$7.91^{+0.08}_{-0.08}$	0.04 ± 0.06
NGDEEP	02770	53.153851	-27.767378	2.31	$9.17^{+0.00}_{-0.01}$	$9.82^{+0.23}_{-0.13}$	$8.42^{+0.04}_{-0.04}$	0.11 ± 0.01
NGDEEP	02798	53.171741	-27.766728	3.19	$8.75^{+0.02}_{-0.02}$	$2.78^{+0.27}_{-0.21}$	$8.12^{+0.11}_{-0.12}$	0.01 ± 0.13
NGDEEP	02823	53.160498	-27.766138	2.67	$8.07^{+0.02}_{-0.02}$	$2.73^{+0.24}_{-0.21}$	$8.14^{+0.09}_{-0.10}$	-0.10 ± 0.09
NGDEEP	02897	53.172172	-27.763745	2.21	$8.21^{+0.03}_{-0.02}$	$4.65^{+0.26}_{-0.32}$	$7.96^{+0.04}_{-0.03}$	-0.03 ± 0.02

M. SPECTRA AND METALLICITY GRADIENTS OF INDIVIDUAL GALAXIES

Here we provide figures of spectra and metallicity gradient measurements for all individual galaxies in our sample, including 6 galaxies in ASPIRE sample (Fig. 23, 24), and 89 galaxies in NGDEEP sample (Fig. 25).

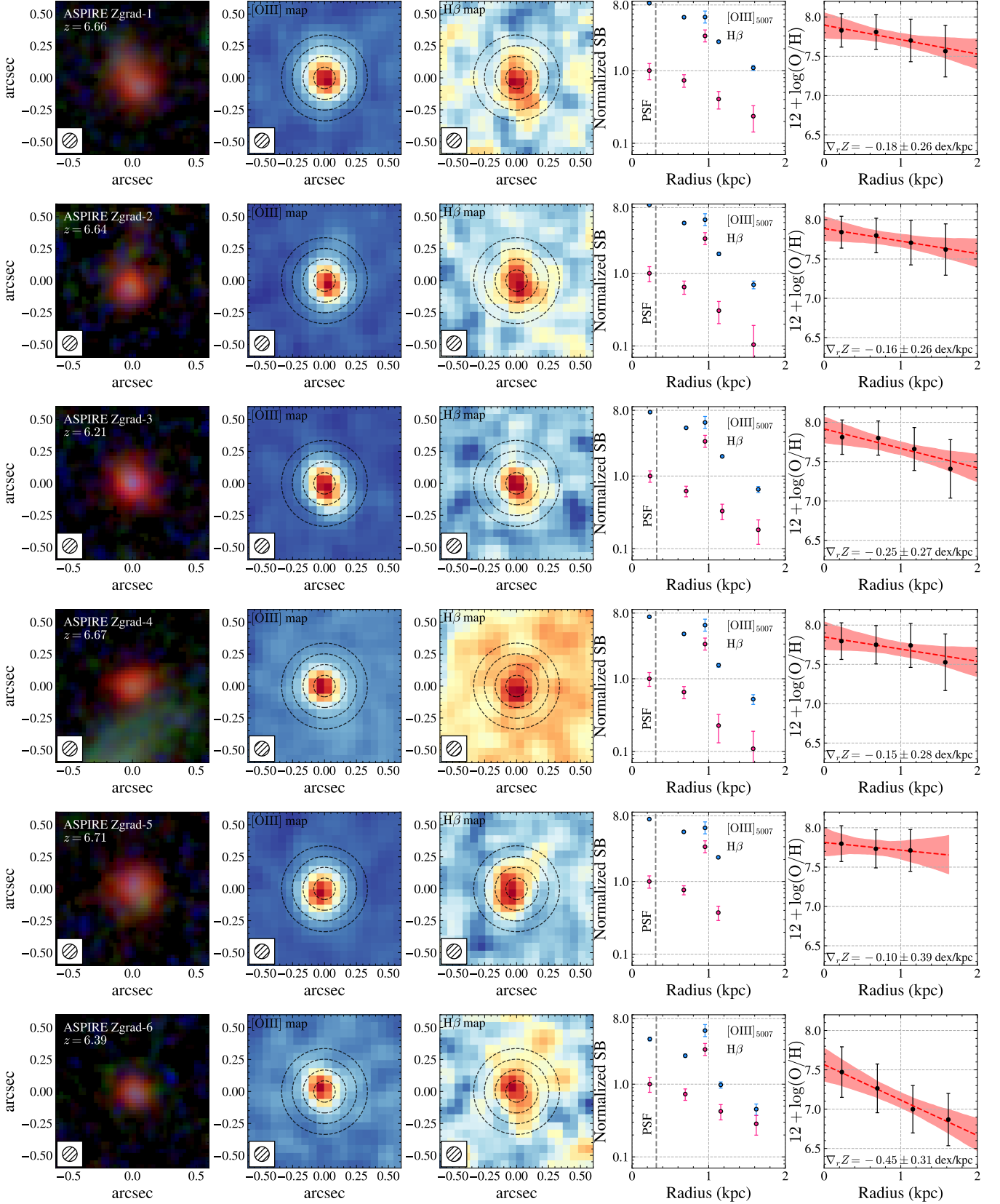


Figure 23. metallicity gradient measurements of individual galaxies in ASPIRE. The right four panels are the same as Fig. 1, but for individual galaxies with the highest SNR. The first panel shows the false-color JWST NIRCcam image (with F115W, F200W, and F356W) centered on each source.

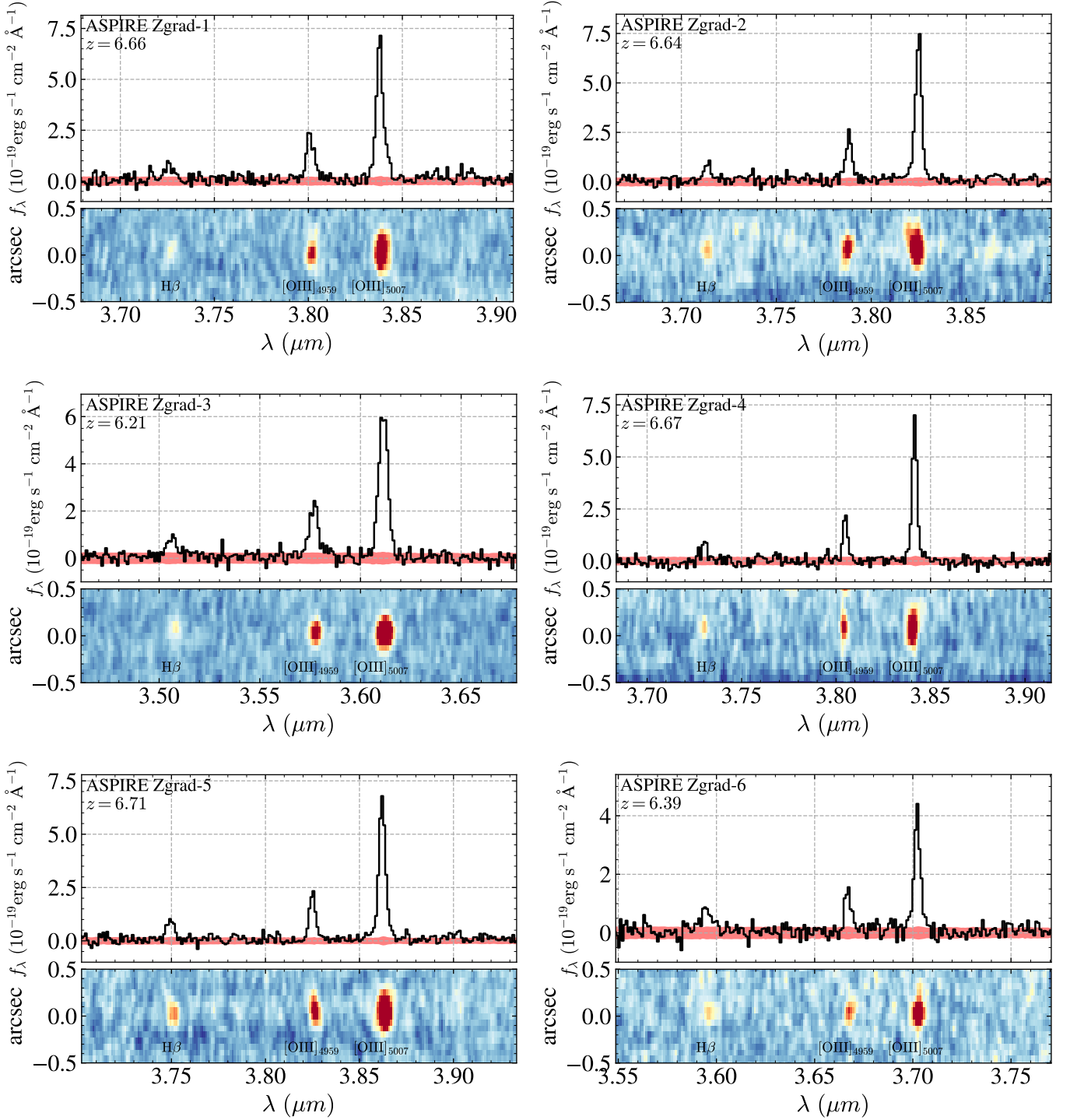


Figure 24. The 1D and 2D NIRCам F356W grism spectra of each source in Fig.23.

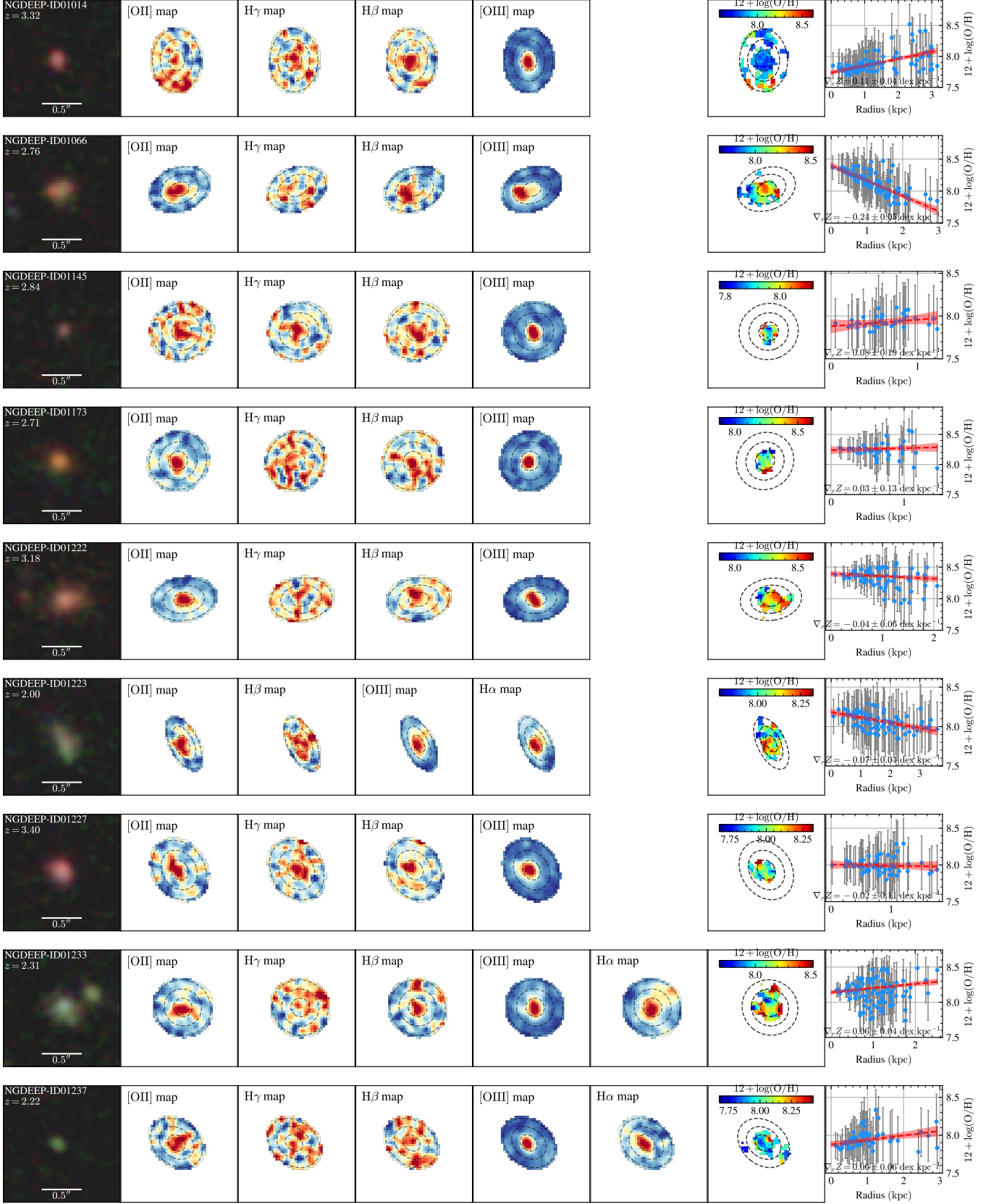


Figure 25. The false-color image, line maps, metallicity maps, and metallicity gradients for each source in the NGDEEP sample.

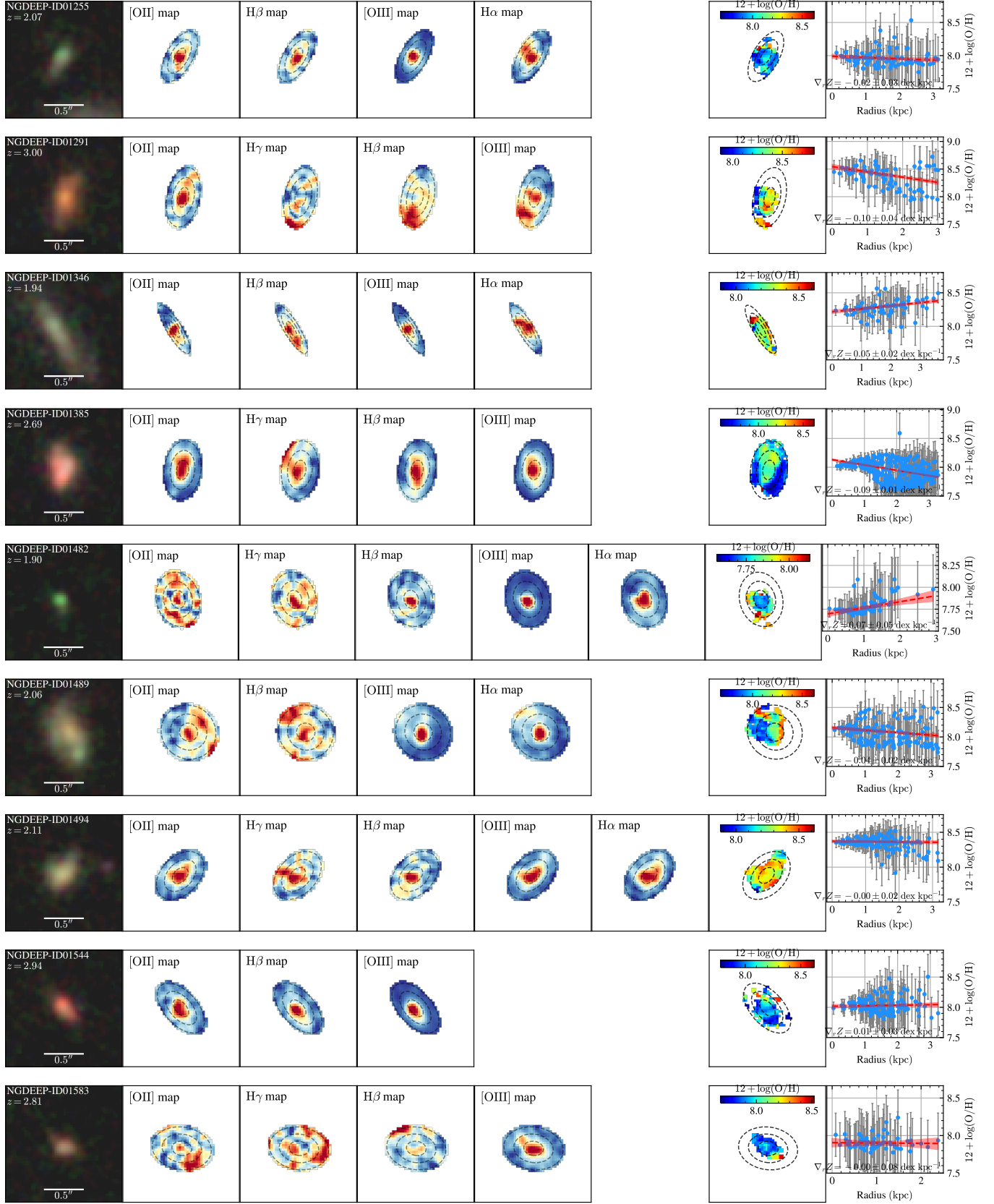


Figure 26. Continued.

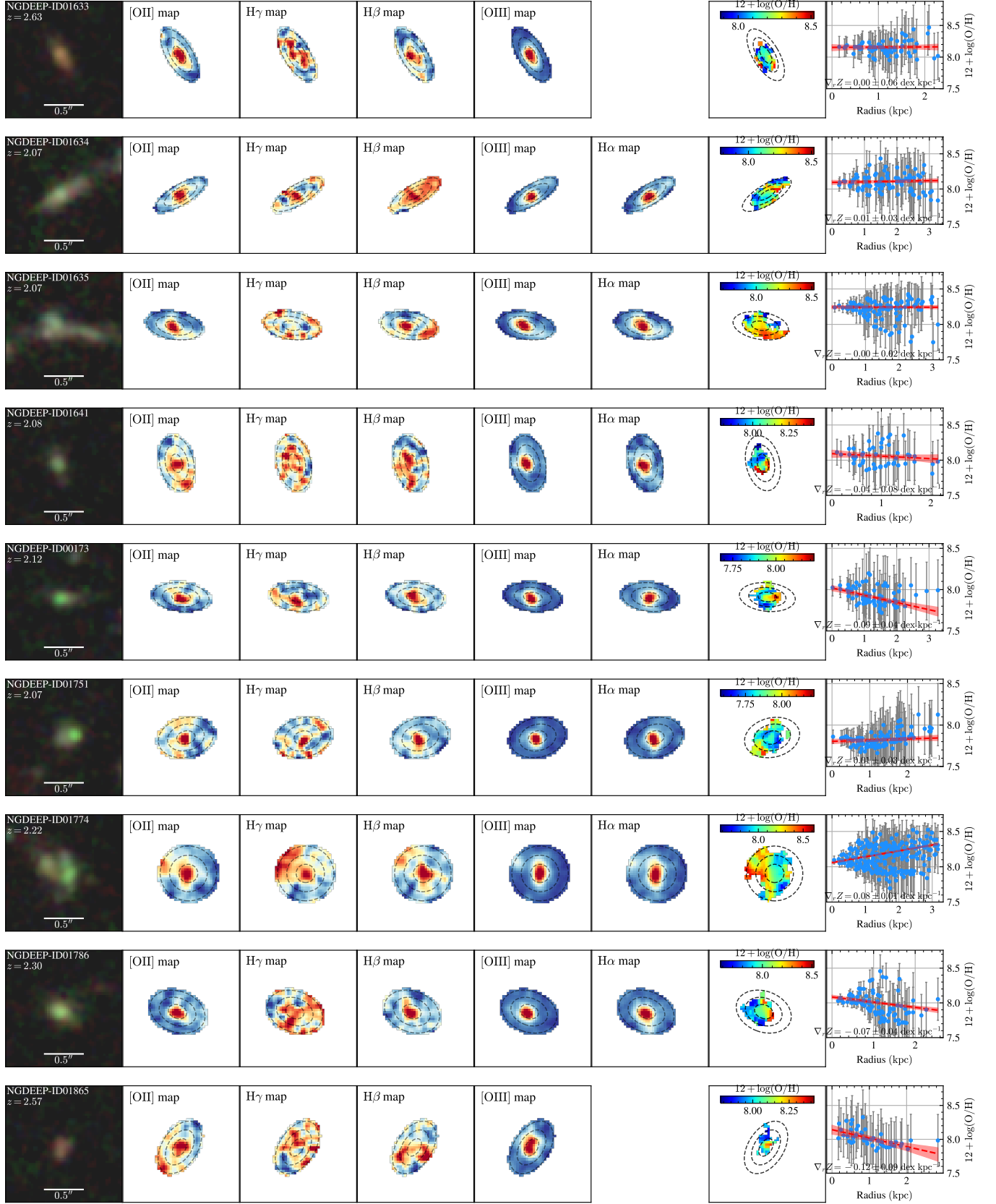


Figure 26. Continued.

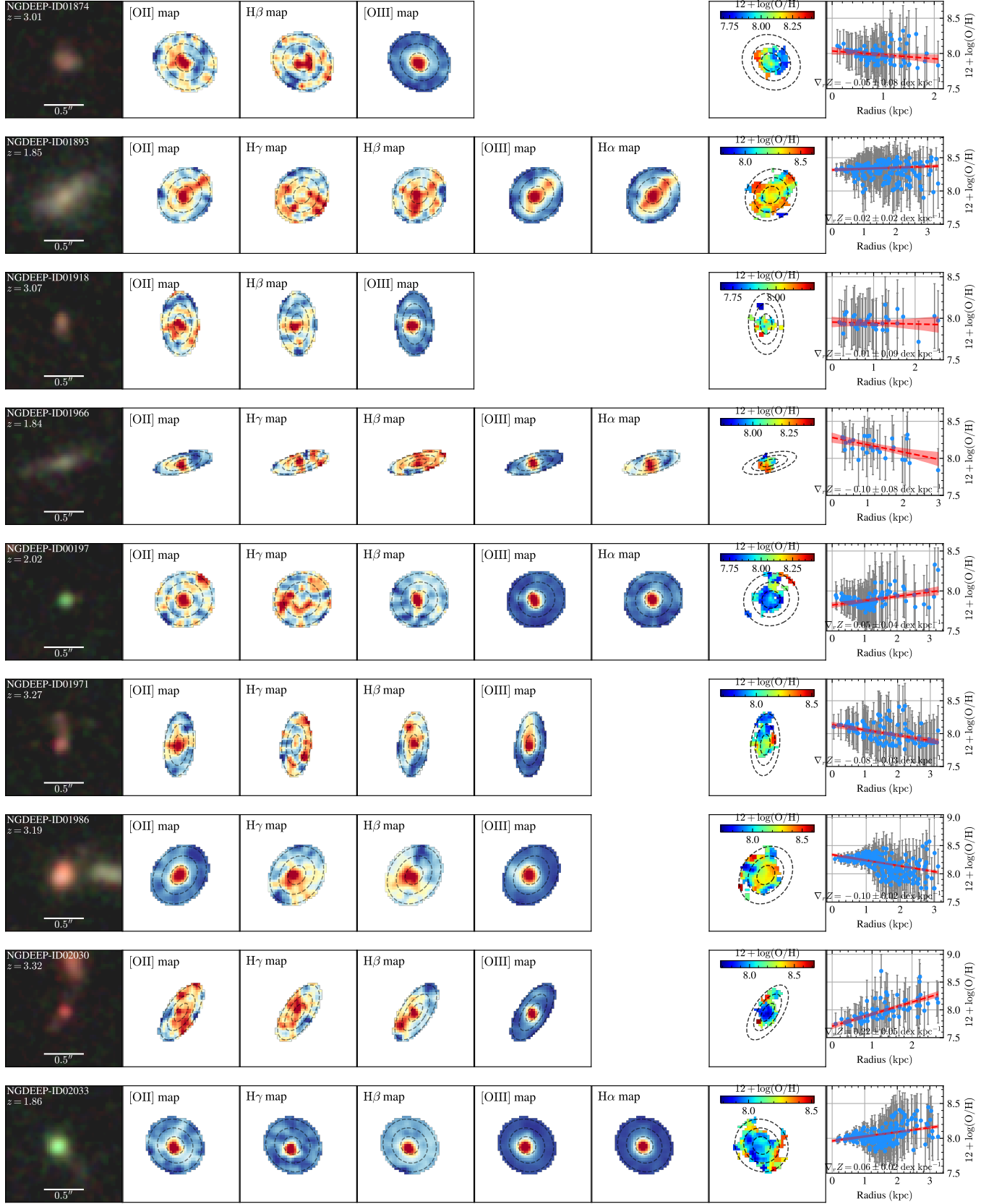


Figure 26. Continued.

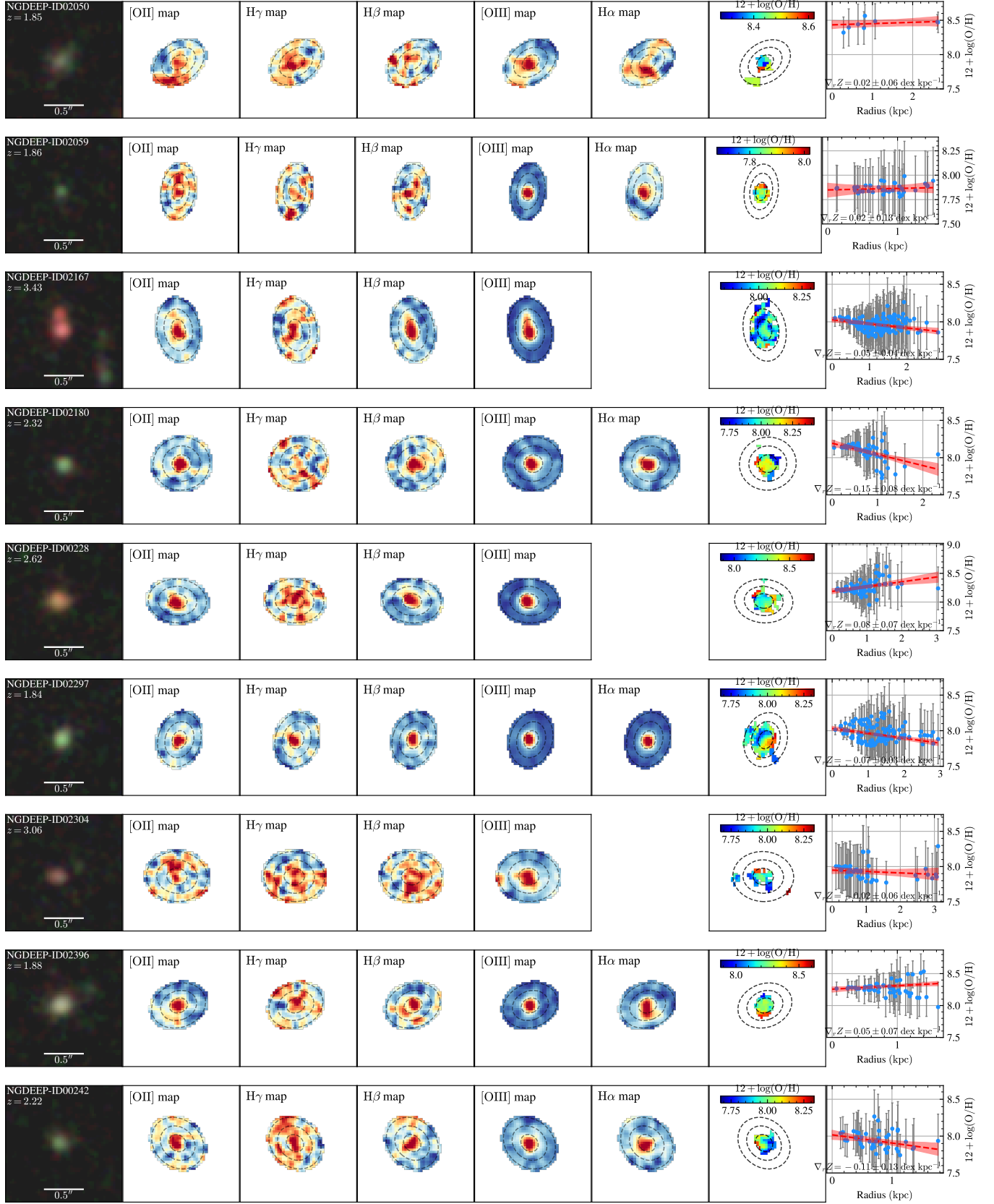


Figure 26. Continued.

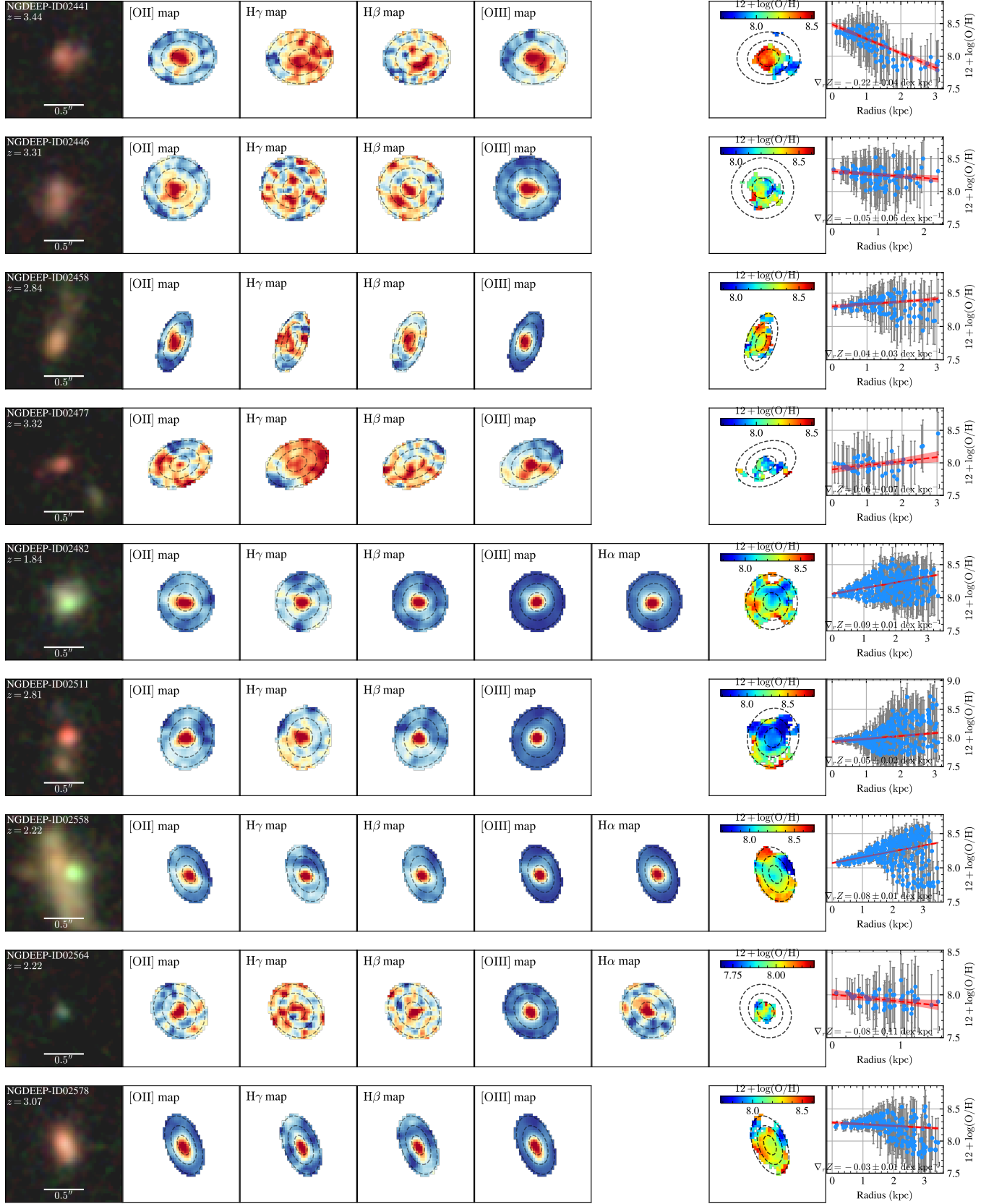


Figure 26. Continued.

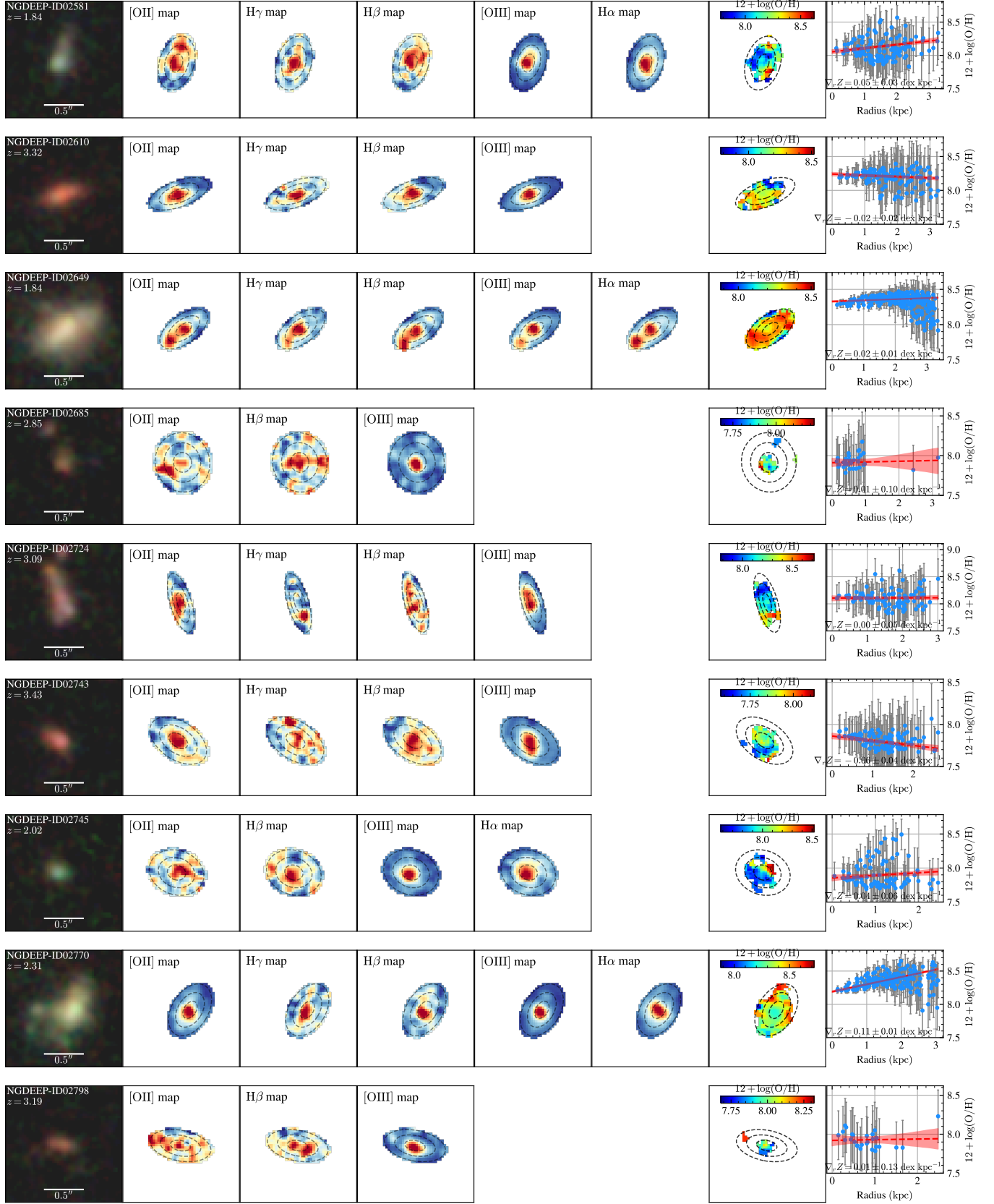


Figure 26. Continued.

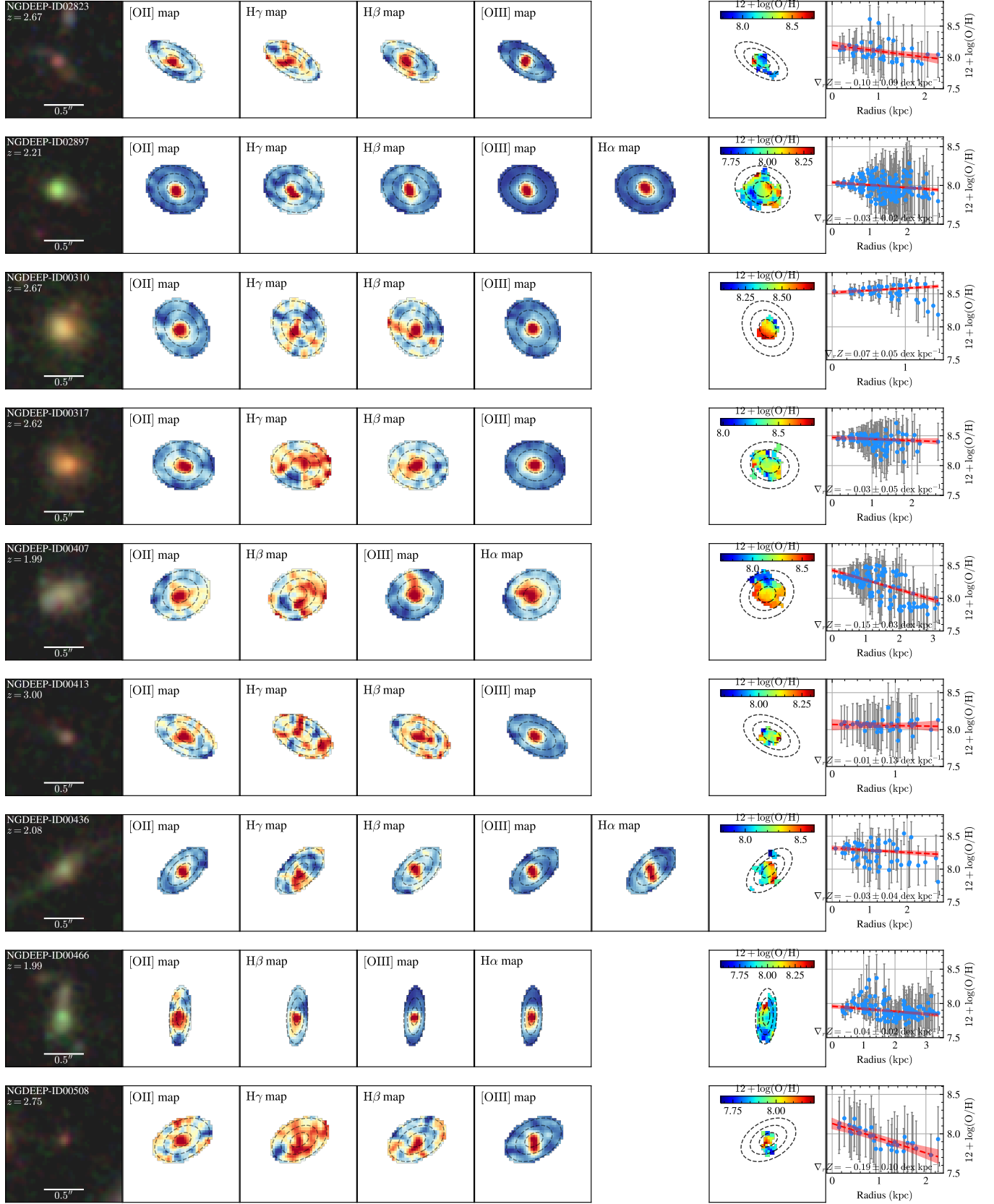


Figure 26. Continued.

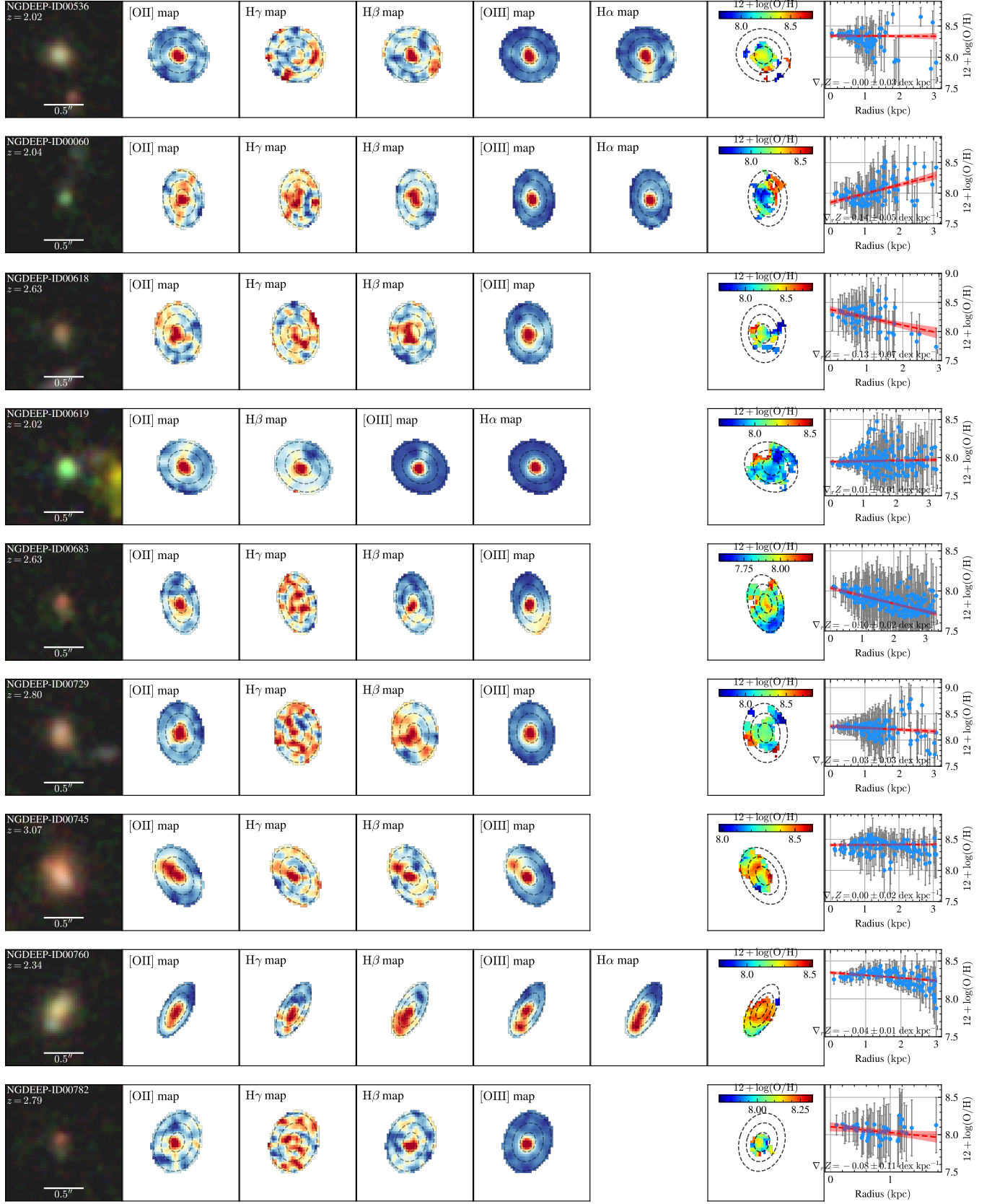


Figure 26. Continued.

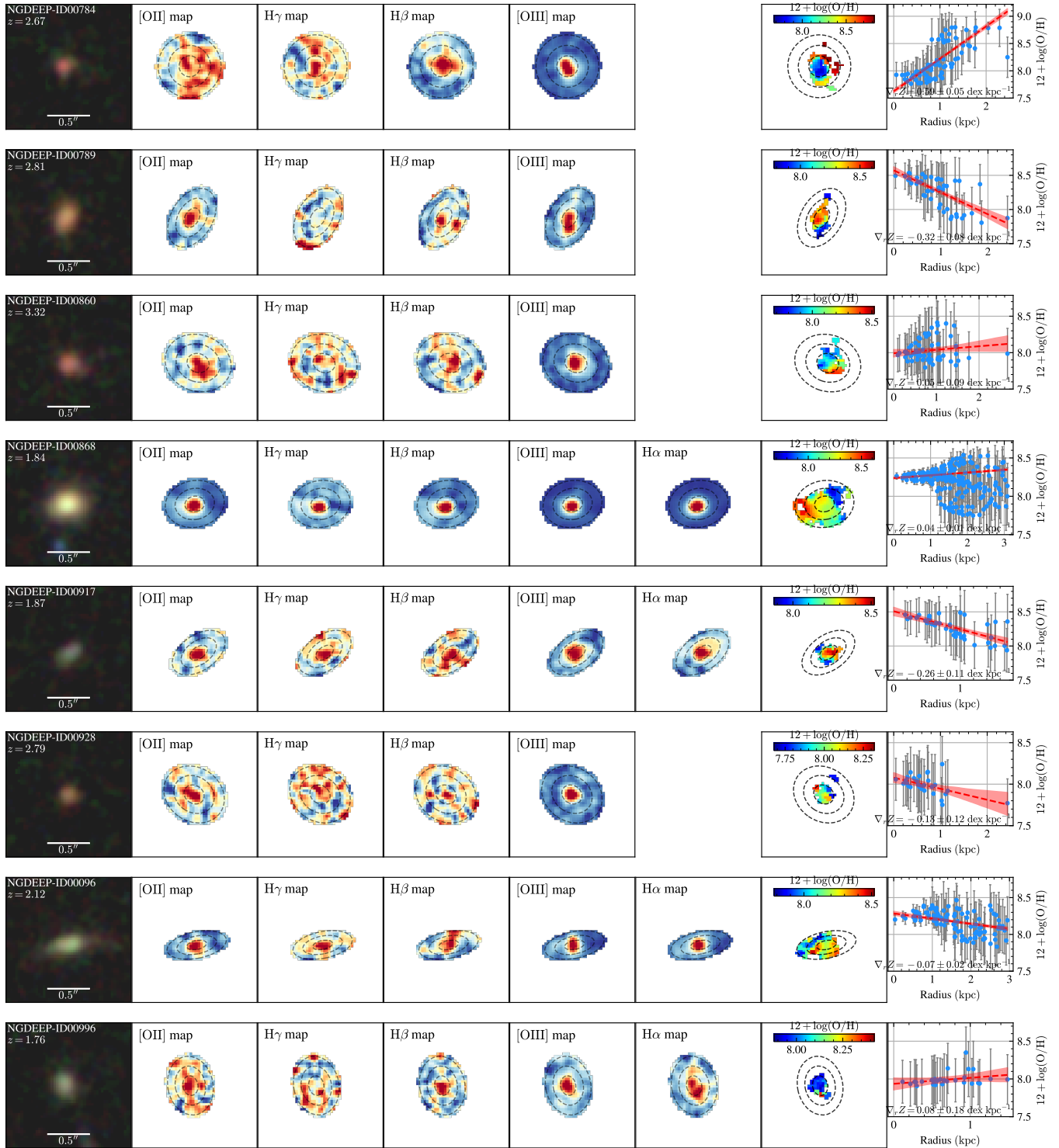


Figure 26. Continued.